Durham E-Theses

BaTiO???3 ceramics for PTC applications.

Roberts, Arwel R.

How to cite:

Roberts, Arwel R. (1994) *BaTiO???3 ceramics for PTC applications.*, Durham theses, Durham University. Available at Durham E-Theses Online: http://etheses.dur.ac.uk/1428/

Use policy

The full-text may be used and/or reproduced, and given to third parties in any format or medium, without prior permission or charge, for personal research or study, educational, or not-for-profit purposes provided that:

- a full bibliographic reference is made to the original source
- a link is made to the metadata record in Durham E-Theses
- the full-text is not changed in any way

The full-text must not be sold in any format or medium without the formal permission of the copyright holders.

Please consult the full Durham E-Theses policy for further details.

Academic Support Office, Durham University, University Office, Old Elvet, Durham DH1 3HP
e-mail: e-theses.admin@dur.ac.uk Tel: +44 0191 334 6107
http://etheses.dur.ac.uk

The copyright of this thesis rests with the author.
No quotation from it should be published without
his prior written consent and information derived
from it should be acknowledged.

$BaTiO_3$ CERAMICS FOR PTC APPLICATIONS

by

ARWEL W. ROBERTS B.Sc., A.M.I.E.E., Grad.Inst.P.

A thesis submitted for the degree of
Doctor of Philosophy in the
University of Durham

December 1994

0 8 DEC 1995

ABSTRACT

It is well known that donor doped barium titanate ceramics exhibit a Positive Temperature Coefficient of Resistance (PTCR) characteristic above the crystallographic transition temperature, T_c ~ 130 °C, at which the material transforms from the ferroelectric to the paraelectric state. The magnitude and form of the PTCR characteristic are known to be influenced by the composition and preparation conditions of the ceramic, and by the presence of impurities; especially by the donor dopant concentration and by the sintering conditions. Heywang originally proposed a model based on the presence of two dimensional grain boundary layers consisting of discrete electron traps, to explain the PTCR effect. This model was subsequently extended by Daniels to include a three dimensional layer of electron traps extending from the grain boundaries into the grain bulk.

Specimens of donor doped barium titanate ceramics were prepared with different donor concentrations and subjected to varying sintering conditions. They were then investigated by studying their microstructure, electrical and dielectric properties, both at ambient temperature and above the transition point.

Resistivity - temperature measurements were carried out to determine the influence of composition and firing conditions on the PTCR characteristics. Resistance - voltage measurements at room temperature were carried out on specimens containing different donor concentrations to investigate whether insulating intergranular layers formed at higher concentrations. Additionally, attempts were made to study grain boundaries by direct observation, using polarised light microscopy to examine the ferroelectric domain structure, and using the electron barrier voltaic effect in the scanning electron microscope to investigate variations in carrier lifetime.

The PTCR effect was found to be exclusively a grain boundary phenomenon. Dielectric measurements showed that variations in the PTCR characteristic with specimen composition and processing history were related only to changes in the grain boundary resistance and that the grain bulk resistance was unchanged. Furthermore, the PTCR properties were mainly determined by the grain boundary potential barriers. Analysis of resistivity - temperature characteristics in terms of the Ihrig-Puschert model showed that potential barrier height was the main influence, with the effects of any insulating grain boundary layers being less important. The results of this study were considered to be more consistent with the Heywang model than the Daniels model. Finally, activation energy analysis of PTCR characteristics showed that the grain boundary potential barriers also influence the resistivity of the ceramics at temperatures below the PTCR transition.

DECLARATION

I declare that the work reported in this thesis, unless otherwise stated, was carried out by the candidate, that it has not previously been submitted for any degree and that it is not currently being submitted for any other degree.

Dr. A. W. Brinkman

Supervisor

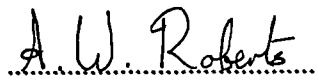

A. W. Roberts

Candidate

ACKNOWLEDGEMENTS

I would like to thank my supervisors, Dr.A.W.Brinkman and the late Professor J.Woods for their valuable advice and constant encouragement in the course of this work. I also wish to thank the late Dr. G.J.Russell for help with the electron microscopy and for many useful suggestions, and Dr.H.M.Al Allak for many valuable discussions and suggestions throughout the research. I am also grateful to Elmwood Sensors Ltd. for the provision of materials for this work and to Mr. P.Thompson and Mr. K.McLoughlin for their assistance. Thanks are also due to Mr. N.Thompson and the workshop staff for their willingness to provide their skills and advice whenever necessary.

I wish to thank Mrs. S.Fairless for typing this thesis and Mrs. J.Morgan for the preparation of the drawings and photographs.

Finally I should like to thank my parents for their constant support and encouragement throughout this work.

CONTENTS

CHAPTER 2

CHAPTER 1

INTRODUCTION AND SCIENTIFIC BACKGROUND

1.1 Introduction

Pure, stoichiometric barium titanate is a high band gap semiconductor: it has a band gap of $\simeq$ 3 eV and a resistivity of > 10^{10} Ω cm at room temperature, and therefore behaves as an insulator [1]. The material is also a ferroelectric exhibiting a type I transition at the Curie point, T_C = 130°C.

When ceramic polycrystalline barium titanate is made n-type by doping, its electrical resistivity exhibits a remarkable property at the Curie temperature; it increases rapidly with increasing temperature, rising from about 10^1 - 10^2 Ω cm by several orders of magnitude over a small temperature range at a rate of up to 100% per K. This effect is known as the Positive Temperature Coefficient, or PTC effect (fig. 1.1 (a)) [1].

The temperature at which the resistivity rise occurs may be altered by changing the Curie temperature. This is achieved by the addition of lead or strontium titanate to form a mixed titanate, using a mixture of lead and barium titantes to increase the Curie temperature or strontium and barium titanates to decrease it (fig. 1.1 (b)).

Ceramics showing PTC anomalies find practical application in the manufacture of positive temperature coefficient thermistors. These are useful as solid state temperature control devices and current limiting devices; an increase in the ceramic temperature increases its resistance thereby automatically decreasing power dissipation in a series circuit.

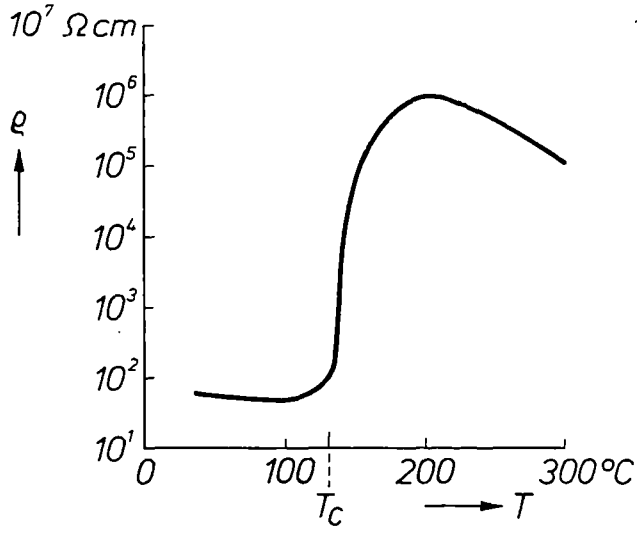

Figure 1.1 (a) Resistivity as a function of temperature of $BaTiO_3$ doped with 0.3 at. % La. T_C is the Curie point. (After Daniels et al. [26]).

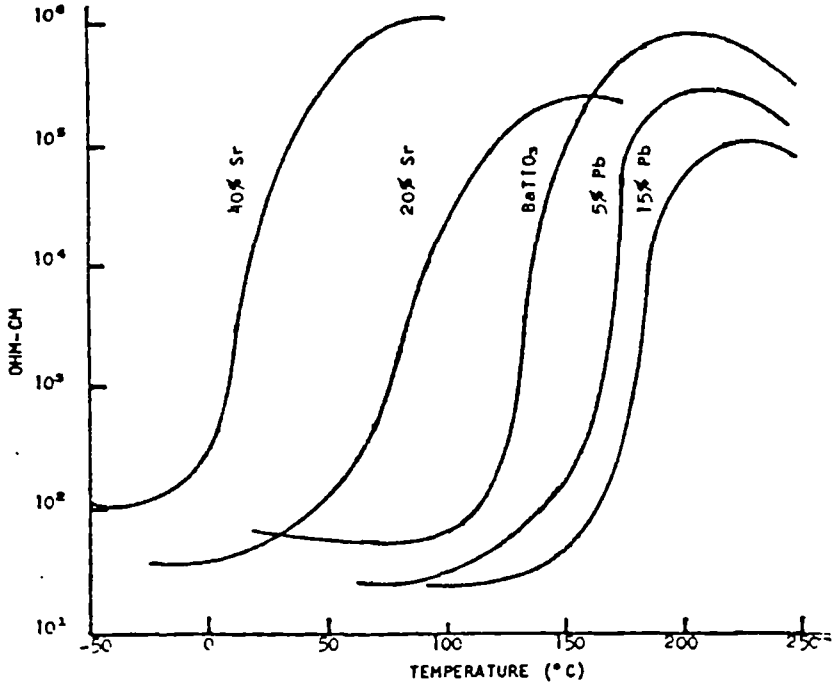

Figure 1.1 (b) Variation of resistivity-temperature characteristics of PTC ceramics with Sr or Pb substitution. (After Rutt et al. [32]).

1.2 The Ferroelectric Properties of $BaTiO_3$

In the temperature region above 130°C barium titanate has a cubic crystallographic structure, shown in fig. 1.2, named the perovskite structure after the related mineral perovskite ($CaTiO_3$): the lattice parameters of the unit cell are a = 4.009 Å [2]. Since the cubic structure is centrosymmetric no polar axis exists in the unit cell and the material is not ferroelectric. When the temperature is reduced to below 130°C a crystallographic transition occurs from the cubic to the tetragonal form; the unit cell elongates along an edge to give lattice parameters a = 4.003 Å, c = 4.022 Å and an axial ratio c/a = 1.005 Å [2]. The tetragonal structure is non-centrosymmetric and possesses a dipole moment, and therefore a polar axis, parallel to the crystallographic c-axis, in the absence of an external electric field, i.e. the crystal is ferroelectric. This results in the spontaneous occurrence of electric polarization in the material accompanied by the formation of a polarization domain structure in an analogous manner to magnetic domains in ferromagnetic materials. The transition temperature of 130°C is called the Curie point, T_C.

As the Curie point is approached and passed, the dielectric constant of the material undergoes rapid change. With increasing temperature, the relative permittivity reaches a pronounced maximum near the Curie point (fig. 1.3). As the temperature is further increased above the Curie point the value of the relative permittivity decreases according to the Curie-Weiss law

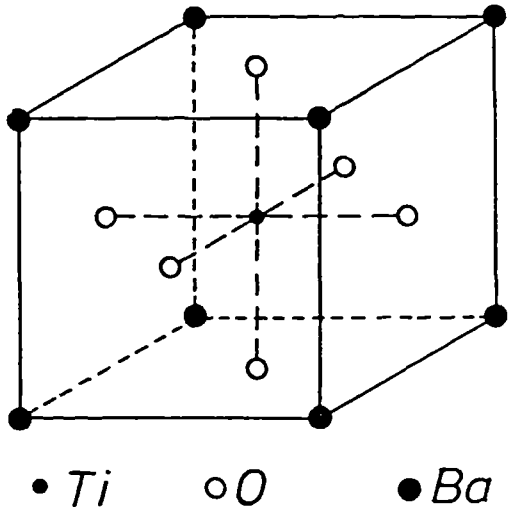

Figure 1.2 Unit cell of $BaTiO_3$ in the cubic phase (above 130°C).

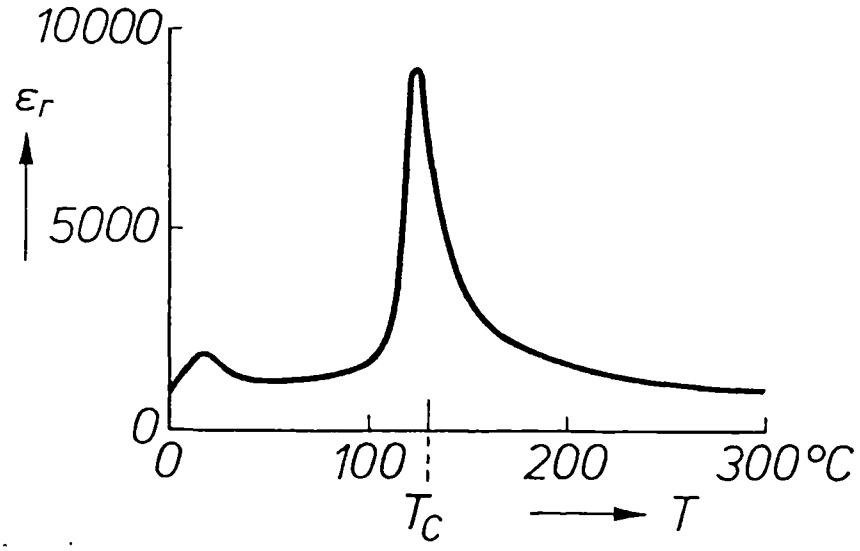

Figure 1.3 Dielectric constant ε_r of $BaTiO_3$ as a function of temperature. A peak occurs at the Curie point T_C. (After Daniels et al. [26]).

$$\varepsilon_r = \frac{C}{T - T_o} \qquad (1.1)$$

where ε_r is the relative permittivity

T is the temperature in K

C is a constant called the Curie constant

T_o is the Curie temperature.

T_o is defined as the temperature at which the extrapolated curve of $\frac{1}{\varepsilon_r}$ cuts the temperature axis; it does not coincide with the Curie point, the temperature at which the spontaneous polarization vanishes, but is generally a few degrees below the Curie point.

For $BaTiO_3$ $C = 1.8 \times 10^5$ K and $T_o = 383$ K. [3]

It may be noted that there exists two other ferroelectric polymorphs of $BaTiO_3$ [2]; one has an orthorhombic structure which transforms from the tetragonal form at 0°C and the other, rhombohedral form transforms from the orthorhombic at -90°C. These forms are, however, of no practical influence on the properties of PTC devices.

1.3 Theoretical Explanation for the PTC Effect

A valid theoretical model for the PTC effect in barium titanate must explain the following experimentally observed properties.

(i) The PTC effect is directly correlated with the ferroelectric properties of $BaTiO_3$. Changing the Curie point produces a corresponding change in the temperature at which the PTC effect occurs [1].

(ii) The PTC effect does not occur in n-doped single crystal $BaTiO_3$, although a polycrystalline specimen prepared from the same single crystal does display the PTC effect [4].

(iii) Undoped $BaTiO_3$ does not exhibit the PTC effect [1].

(iv) The PTC effect occurs only in donor doped $BaTiO_3$ ceramics. Material rendered n-type by a reducing treatment is a good conductor but does not show the PTC resistivity anomaly at the Curie point [1].

(v) It is known that the conditions under which the sintering process used to make the $BaTiO_3$ ceramics is carried out strongly influence the PTC effect. In particular the sintering temperature, sintering atmosphere and the rate of cooling from the sintering temperature affect the resistivity of the material both at room temperature and in the high temperature, high resistivity state [see section 1.7 below].

Although the PTC effect was first discovered by workers at Philips in 1955 [5], the first model giving a good interpretation of the results was that published by Heywang [6] in 1961 and further developed by Jonker [5,7].

1.4 The Heywang Model [6]

This model suggested the existence of deep acceptor states at the grain boundary interface which trap the conduction electrons generated within the grain bulk by n-type doping. This creates a depletion layer extending into the ceramic grains and causes band bending which sets up a potential barrier at the grain boundaries, i.e. a Schottky barrier, which impedes the movement of conduction electrons across grain boundaries (fig. 1.4).

From Heywang the height of the surface barrier potential may be expressed as

$$\phi = \frac{e N_D}{2 \varepsilon_r \varepsilon_o} z_0^2 \qquad (1.2)$$

where e is the electronic charge, N_D the donor concentration, d the thickness of the depletion region, ε_r the relative permittivity and ε_o the permittivity of free space, and the assumption is made that all donors are fully ionized.

For overall charge neutrality in the boundary region

$$Q_S = - Q_D \qquad (1.3)$$

where Q_S is the charge in the surface states and Q_D the charge in the depletion region. This expression becomes

$$N_{A0} = N_D z_0$$

where N_{A0} is the concentration of acceptor states per unit area at the grain boundary.

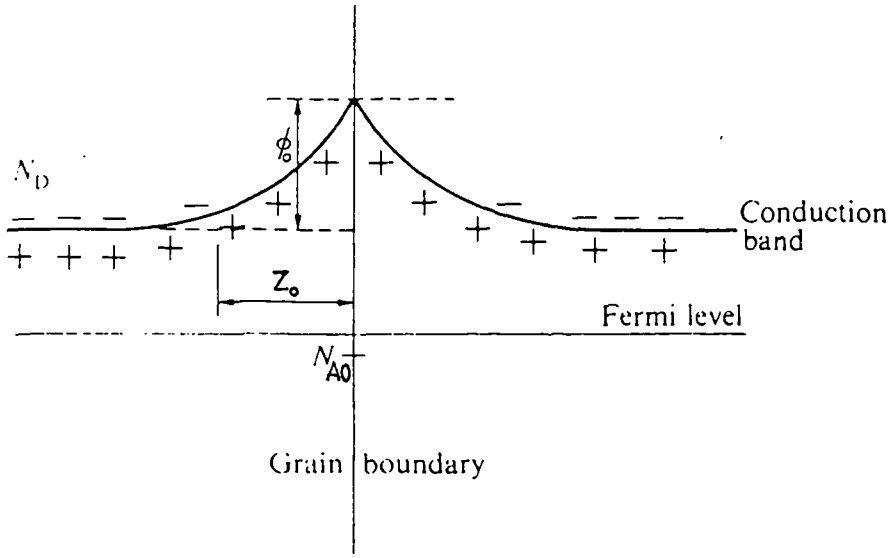

Figure 1.4 Energy-level diagram near a grain boundary. (After Heywang [6]).

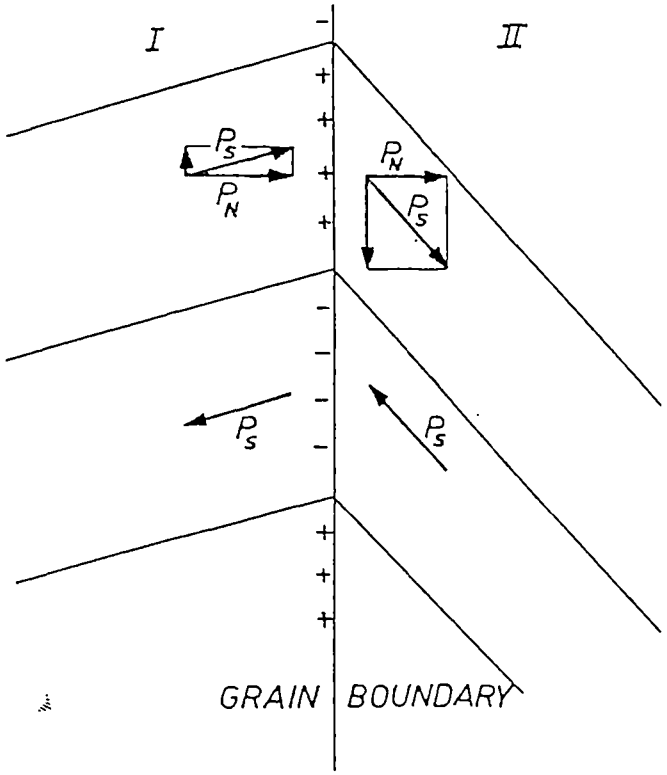

Figure 1.5 Polarisation of ferroelectric domains at a grain boundary. (After Jonker [7])

and combining (1.2) and (1.3) we have

$$\phi = \frac{e}{2\varepsilon_r\varepsilon_o}\frac{N_{A0}^2}{N_D} \tag{1.4}$$

The resistivity of the ceramic is then controlled by the height of the potential barrier at the grain boundary and may be expressed in the form

$$\rho = \rho_\infty \exp\left[\frac{e\phi}{kT}\right] \tag{1.5}$$

where ρ_∞ is a constant, the resistivity in the limit $T\rightarrow\infty$, and ϕ denotes a mean barrier potential which takes account of variations between individual grains in the ceramic.

At temperatures just above the Curie point, the relative permittivity ε_r falls rapidly in accordance with the Curie-Weiss law. Since $\phi \propto \frac{1}{\varepsilon_r}$ (equation 1.4 above) it may be seen that the height of the potential barrier increases rapidly giving rise to a corresponding increase in resistivity according to equation (1.5) above. This is, therefore, the source of the PTC effect.

The fact that the rapid fall in the relative permittivity below the Curie point does not give rise to a similar resistivity effect was explained by Jonker [5] in terms of the spontaneous ferroelectric polarisation below T_C. He suggested that the domain structure within

the grains built up in such a way as to wholly or partially compensate the excess surface charge, thus neutralising the potential barrier (fig. 1.5). This assumed the existence of 180° domains more or less randomly orientated so that on average half the domains would be oriented so as to reduce the potential barrier height, whereas the remaining half tended to increase the barrier height, producing low and high resistivity regions respectively at the grain boundaries. The high resistivity regions do not, however, dominate the behaviour of the ceramic because the low resistivity regions are electrically in parallel with them and provide a low impedance current path. Variations of this explanation have also been suggested by Kulwicki and Purdes [8] and Heywang [6].

When Haanstra and Ihrig [9] carried out a transmission electron microscopy investigation of PTC-type $BaTiO_3$ ceramics, however, they failed to find any specific orientation of the ferroelectric domains at the grain boundaries and found many more 90° domains, which were self-compensating, than 180° domains. They therefore suggested that charge compensation below T_C was brought about by local variations in the relative permittivity together with some local charge compensation by partially matching domains at the grain boundaries. This may therefore be regarded as a further modification of Jonker's theory.

These early theories assumed that the surface acceptor states were caused by adsorbed oxygen. This appeared to be supported by the fact that heat treatment in a reducing atmosphere suppressed the

PTC effect, but that it could be restored by a second treatment in an oxidising atmosphere [10,11]. However, little reliable evidence concerning the nature of the acceptor states was available until the investigations by Daniels, Härdtl, Hennings and Wernicke [12,13,14,15,16] later showed that the acceptor states were caused by barium vacancies (see Section 1.5 below).

Further evidence for the existence of grain boundary barriers above the Curie point arose from the direct observation of resistive grain boundaries and high electric fields at grain boundaries by the use of decoration techniques [17] and voltage contrast imaging [18]. Ihrig and Klerk [19] have also observed the grain boundary barriers by cathodo-luminescence at room temperature.

Heywang [1] found that grain boundary shadows, indicating the presence of resistive barriers, observed in the scanning electron microscope appeared to be most pronounced at grain boundaries which had a thick layer of intergranular phase. This observation, combined with the fact that the inclusion of acceptor impurities were shown by electron microprobe analysis to be concentrated in the glassy intergranular phase [1], gave rise to the theory that acceptors derived from impurities in an intergranular phase were influential in the development of the grain boundary barriers.

Gerthsen and Hoffmann [20] in a study of the current-voltage characteristics of a single grain boundary measured grain boundary capacitance values which were lower than expected assuming

Heywang's 2-dimensional model. They proposed the existence of a Ti rich intergranular phase, approximately 600 nm thick, in order to explain this. However, several other experiments on PTC compounds having varying amounts of second phase obtained from TiO_2 in the composition [21,22] provided no evidence of influence by the second phase on the physical nature of the grain boundary barrier. An intergranular phase of the suggested thickness, ~ 600 nm, cannot be detected micrographically; transmission electron microscope investigations by Haanstra and Ihrig [9] also failed to detect a phase of this thickness. It therefore seems unlikely that such a layer exists. Ihrig and Puschert [23], following earlier work by Kulwicki and Purdes [8], concluded that the Heywang model satisfactorily explained the experimental results when modified to include a range of acceptor state energies at the grain boundary, without recourse to an intergranular layer. These results have been subject to further argument [24,25].

The Heywang model provides a reasonably satisfactory explanation of the principal features of the PTC effect, i.e. the magnitude and rate of the resistivity charge, the dependence of the PTC transition temperature on the Curie point, and the grain boundary origin of the PTC effect. The model as it stands, however, does not explain a number of experimental observations, particularly the following four points :

1. What is the precise nature of the grain boundary acceptor states?
2. Why is the PTC effect observed only in material made n-type by donor doping, but not in material treated in a reducing atmosphere?
3. What is the explanation for the strong dependence of the PTC effect on the manner in which the ceramic is cooled after sintering?
4. Why does the room temperature resistivity of the ceramic increase dramatically, to the extent of rendering the material insulating, if the donor dopant concentration is increased beyond about 0.6 atomic %?

1.5 The Daniels Model

The theory of the PTC effect in $BaTiO_3$ ceramics has been extensively studied by workers at Philips. Following a detailed study of the defect structure and diffusion kinetics of barium titanate ceramics [12,13,14,15,16,26] Daniels, Wernicke et al. developed an extended model which they considered to explain more fully the perceived limitations of the Heywang theory described above. Their work on this model is described in a published review article [26].

Daniels et al. concluded that the potential barriers are formed not as a result of a 2-dimensional grain boundary acceptor layer as postulated by Heywang, but by a 3-dimensional zone extending from the grain boundaries into the grains due to barium vacancies which

diffuse inwards from the grain boundaries. The width of this zone thus depends on such variables as temperature, cooling rate and atmospheric composition. It was assumed in the Heywang model that the excess electronic charge arising from donor doping $BaTiO_3$ was entirely compensated by conduction electrons but this was found not to be so by Seuter [27]. In the Daniels model compensation occurs by a combination of the formation of conduction electrons and barium vacancies.

The PTC effect arises as a result of the distribution of atomic defects which arise in the course of the sintering process. This may be divided into two successive processes; firstly a sintering process at a temperature of 1380°-1400°C, followed by a process of cooling to room temperature, possibly interrupted by an annealing period at an intermediate temperature (chapter 2, fig. 2.1). In this model, it is assumed that all the defects in the system reach their equilibrium concentration during the initial sintering process. During the subsequent cooling from about 1400°C to about 1100°C, a quasi-equilibrium is initially maintained, since the mobility of the various defect species is still high at these temperatures. As the temperature falls the mobility is reduced so that eventually the equilibrium state at the lower temperature cannot be reached and a defect state corresponding to equilibrium at a higher temperature is effectively "frozen in". There is little defect mobility below 1000°C.

Daniels and Hardtl [12] carried out a detailed study of the defect chemistry of n-doped barium titanate, using La^{3+} as the dopant (they found that the choice of n-dopant had little effect on the electrical behaviour of the material). They produced an equilibrium model relating the concentrations of defects to the oxygen partial pressure of the atmosphere, considering neutral and singly or doubly ionized (positively charged) oxygen vacancies (V_o^x, $V_o^{\cdot}$, $V_o^{\cdot\cdot}$) and corresponding (negatively charged) barium vacancies (V_{Ba}^x, V_{Ba}', V_{Ba}''). The presence of titanium vacancies in the system was treated as negligible, and interstitials, defect clusters and interactions were likewise disregarded. The calculated vacancy concentrations in this equilibrium model at a temperature of 1200°C are illustrated in fig. 1.6. It is apparent that three different electroneutrality conditions apply to the doped ceramic in the oxygen partial pressure regions I, II and III :

$$2\,[V_{Ba}''] \approx [La^{\cdot}] \quad \text{in region I} \qquad (1.6\ a)$$

$$n \approx [La^{\cdot}] \quad \text{in region II} \qquad (1.6\ b)$$

$$\text{and} \quad n \approx [V_o^{\cdot}] \quad \text{in region III} \qquad (1.6\ c)$$

In region III, i.e. under strongly reducing conditions, conduction electrons compensate the oxygen vacancies, the concentration of which exceeds that of the dopant. In regions I and II, however, the compensation of the excess positive charge introduced by the La^{3+} ions dominates; this occurs via vacancy compensation in region I and

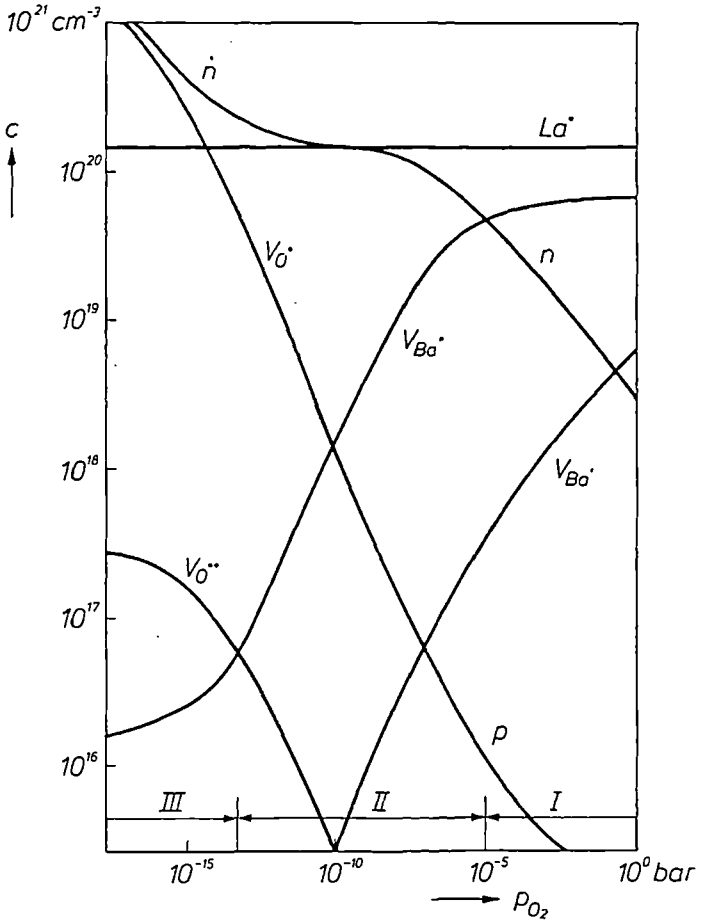

Figure 1.6 Calculated concentrations c of all defects in Daniels' equilibrium model, as a function of oxygen partial pressure Po_2 at 1200°C, for specimens of $BaTiO_3$ doped with 1 at. % La. (After Daniels et al. [26]).

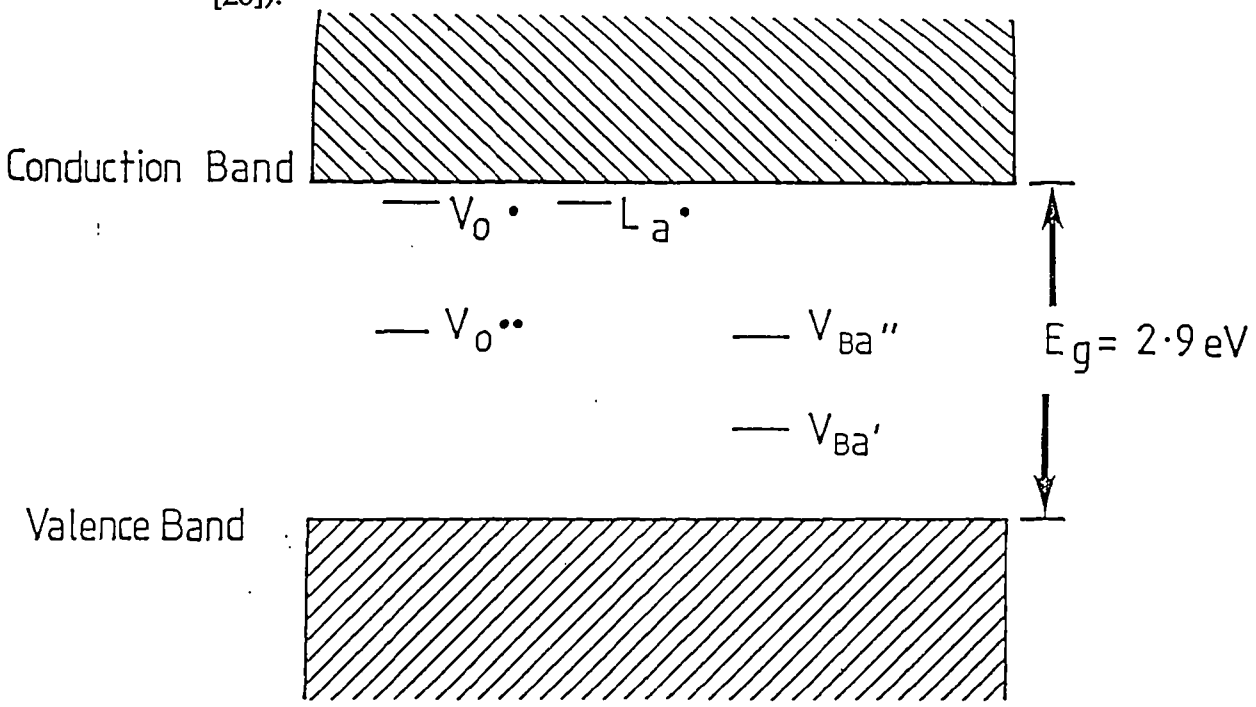

Figure 1.7 Energy level diagram for donor-doped barium titanate ceramic. (After Daniels et al. [26]).

electron compensation in region II. The barium vacancies in region I act as acceptors, lowering the electron concentration: this property of the high temperature equilibrium is of practical importance since the partial pressure of oxygen in air, the usual ambient for sintering, lies in region I, and barium vacancies are the dominant defects in this region.

By repetition of the equilibrium vacancy concentration calculations at various temperatures, Daniels and Hardtl also estimated the positions of the energy levels corresponding to the different defects in $BaTiO_3$ in the energy diagram (fig. 1.7). This reveals why n-type conduction dominates at room temperature. While the energy levels of acceptor-like defects, such as barium vacancies, lie in the middle of the band gap, the levels of donor-like defects such as La ions and singly charged oxygen vacancies, are located within less than 0.1 eV of the bottom edge of the conduction band. The donors are thus virtually all ionized at room temperature resulting in n-type conduction.

The diffusion coefficients of the various defects present were measured by Wernicke [15]: the values of the diffusion coefficients for oxygen and barium vacancies are given in figs. 1.8 and 1.9 respectively. They relate to both doped and undoped $BaTiO_3$ at the oxygen partial pressures generally used in the manufacture of PTC ceramics ($10^{-4} < Po_2 < 1$ bar, i.e. region I).

It was found that the diffusion coefficient of oxygen vacancies (in undoped material) has a fairly high value (10^{-4} cm^2 s^{-1} at 1000°C), which was explained in terms of the perovskite structure in which the oxygen

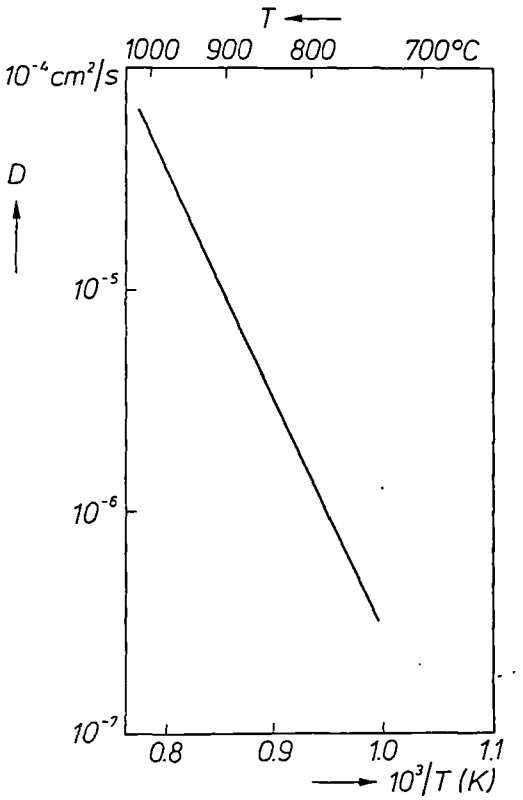

Figure 1.8 Diffusion coefficients D of the oxygen vacancies in undoped $BaTiO_3$ as a function of reciprocal temperature. (After Daniels et al. [26]).

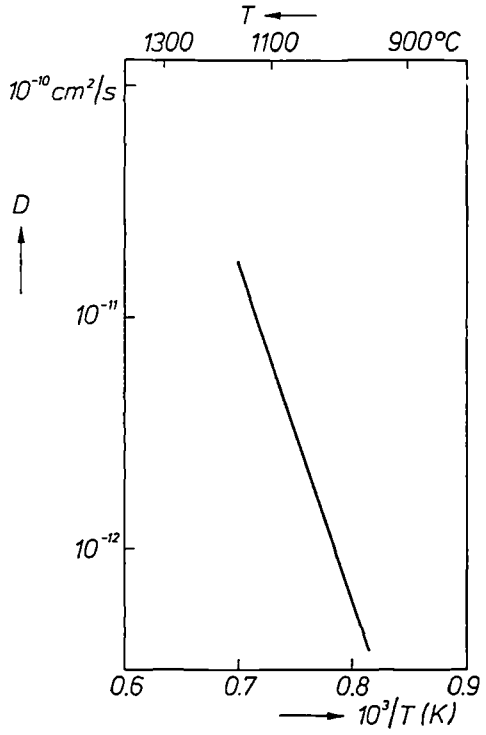

Figure 1.9 Diffusion coefficients D of barium vacancies in $BaTiO_3$ doped with 0.5 at. % La, as a function of reciprocal temperature. (After Daniels et al. [26]).

ions are located close to one another providing an easy path for diffusion. While equilibrium is being established oxygen vacancies are formed or destroyed at the surface of the ceramic specimen and diffuse inwards until the equilibrium has been achieved throughout the specimen.

It can be seen in figs. 1.8 and 1.9 that the diffusion coefficient of barium vacancies in a doped ceramic is about 7 orders of magnitude smaller than that of the oxygen vacancies. The rate of equilibrium restoration in processes determined by barium vacancies will be correspondingly slower than for oxygen vacancies. Wernicke also discovered that the barium vacancies, unlike oxygen vacancies, achieve equilibrium by diffusion from the grain boundaries rather than from the specimen surface. This results from the manner of formation of Ba vacancies.

Wernicke suggests that barium vacancies are formed by barium ions occupying sites in a second titanium rich phase (e.g. $BaTi_3O_7$) at the grain boundaries, which is formed as a consequence of the excess TiO_2 added to the precursor materials of the ceramics to promote sintering. The reaction might proceed according to the equation

$$BaTi_3O_7 + 2Ba\ (\text{lattice}) + 2O\ (\text{lattice}) \rightleftharpoons 3BaTiO_3 + 2V_{Ba} + 2V_o \qquad (1.7)$$

Barium vacancies could then form at grain boundaries and then diffuse into the grain interior until equilibrium were reached throughout the

grain. The additional formation of oxygen vacancies would not delay the achievement of equilibrium because of the speed with which they diffuse throughout the material.

The kinetic processes which occur during a typical sintering process, during which the specimen is sintered in air at 1400°C for a sufficiently long time to achieve equilibrium with the ambient atmosphere, and is then cooled slowly to room temperature, may now be considered. The behaviour of the barium vacancies, the dominant defects, is illustrated in fig. 1.10, which shows the results of Daniels' [13] calculation of the values of twice the total concentration of barium vacancies $2[V_{Ba}^{tot}]$ as a function of equilibrium temperature T^E, at different values of oxygen partial pressure $P^E o_2$. For an air atmosphere, $P^E o_2$ = 0.2 bar. The equilibrium concentration of barium vacancies increases as the temperature falls. At the inversion temperature, T_i the value of $2[V_{Ba}^{tot}]$ equals $[La^{tot}]$, the total concentration of La donors so that the conduction electrons originating from the ionized donors are exactly compensated.

As the specimen temperature falls, the equilibrium concentration of barium vacancies increases and barium vacancies diffuse inwards from the grain boundaries into the bulk of the grains to restore equilibrium. However, as the temperature is further reduced, the speed of diffusion of the vacancies falls so that restoration of equilibrium throughout the grain is no longer possible; ultimately the defects become immobile and the defect concentration corresponds to

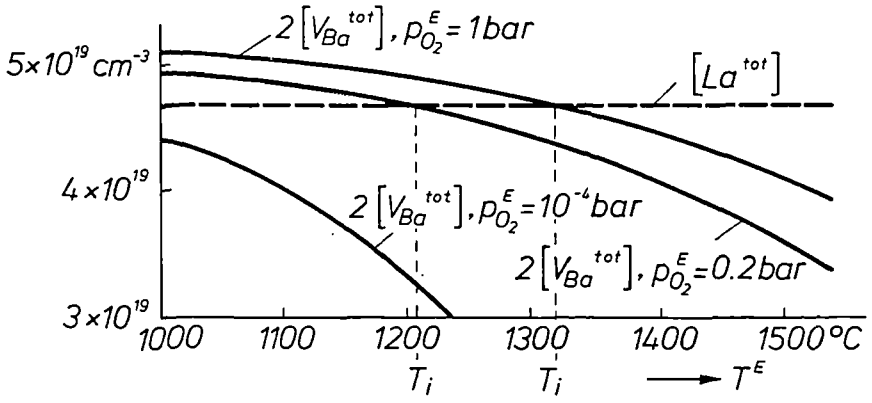

Figure 1.10 Calculated values of twice the total concentration of barium vacancies $2[V_{Ba}^{tot}]$ as a function of the equilibrium temperature T^E at different oxygen partial pressures. (After Daniels et al. [26]).

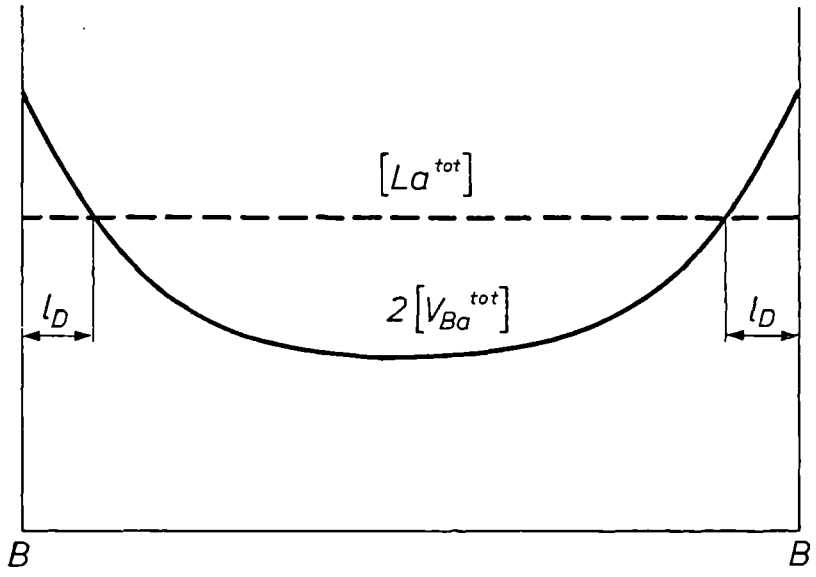

Figure 1.11 Schematic profile of defect concentrations across a grain of La-doped $BaTiO_3$ between grain boundaries B-B.

equilibrium not at the prevailing temperature but at some higher temperature at which diffusion ceased.

Thus, during cooling a diffusion front rich in Ba vacancies penetrates the grain bulk from the grain boundaries, but below a certain temperature loses its mobility. This produces a heterogeneous distribution of the vacancy concentration within each grain (fig. 1.11), so that although the grain boundary regions remain in equilibrium down to fairly low temperatures, this is no longer the case within the grain bulk below about 1300°C.

In the grain boundary region where the total concentration of the donor dopant (lanthanum) $[La^{tot}]$ is less than $2[V_{Ba}{}^{tot}]$, total vacancy compensation occurs and all the conduction electrons introduced by the dopant are captured by barium vacancies, forming a depletion layer of width ℓ_D at the grain boundary. This results in the formation of a potential barrier at the grain boundary, analagous to that proposed in the Heywang model.

The width of the depletion layer ℓ_D depends mainly on the cooling rate and on the diffusion coefficient : the slower the cooling, the further the diffusion front of vacancies penetrates the grain bulk and the greater the value of ℓ_D. At practical cooling rates, the vacancy layer has been shown to have a thickness $\ell_D \sim$ 1-3 μm (fig. 1.11). The Heywang model can thus be considered as the limiting case of the Daniels model for sufficiently fast cooling rates, when the barium vacancies are confined essentially to a 2 dimensional layer at the grain boundaries, so that the two models appear to be consistent.

1.6 Effect of n-doping

As mentioned earlier, the PTC anomaly is observed only in $BaTiO_3$ ceramics made n-type by donor doping. There are many possible elements which may be used as dopants [5,28,29,30] including Y, most of the lanthanides up to Er, Nb, Ta, W, Sb and Bi. Most commercial applications use Y or La, although Ho and Nb are also used and Sb was often used in early products. The choice of dopant depends on the precursor materials [10], other additives used and the extent of any contamination; the most effective material must often be determined experimentally.

The general dependence of low temperature resistivity on dopant concentration is similar for all donor dopants, e.g. fig. 1.12. As the dopant concentration is increased, the resistivity initially falls, reaching a minimum value followed by a sharp rise and a return to insulating properties. The position of the resistivity minimum varies according to the dopant, the ceramic composition and the manufacturing conditions but invariably occurs in a restricted range between about 0.1 at. % to 0.6 at. % of dopant [10,31].

In addition to the effect on resistivity, the donor dopants exercise a strong influence on the grain size of the ceramics: the transition to the insulating condition is accompanied by a sharp reduction in grain size. Rutt et al. [32] found, for ceramics fired under the same conditions and differing only in dopant level, a decrease in grain size from 100 μm at 0 at. % Nb to 3 μm at 0.3 at. % Nb. They also showed

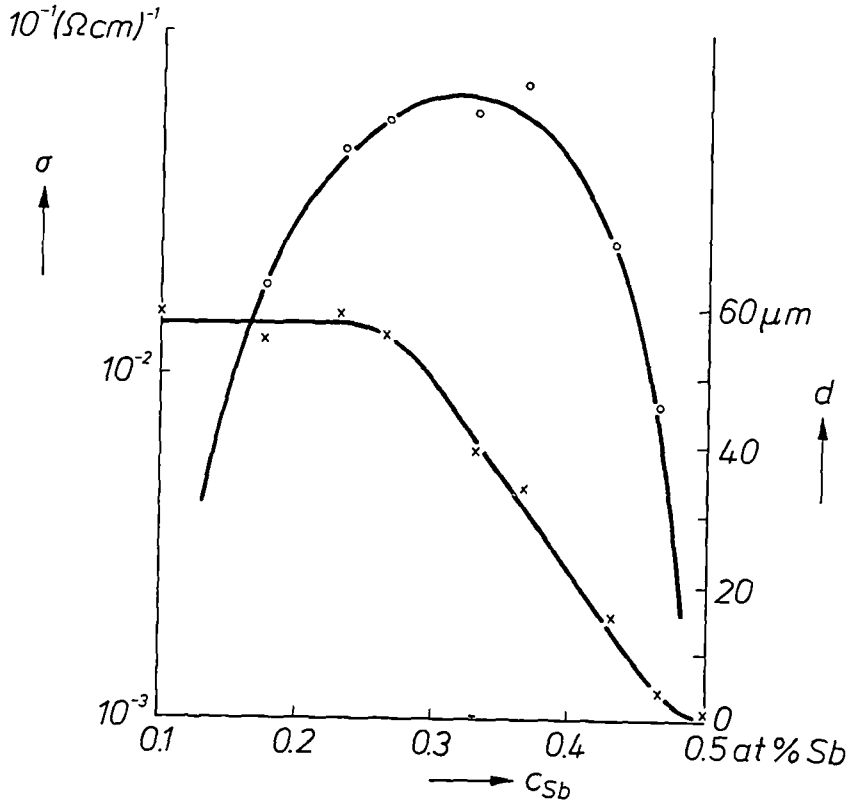

Figure 1.12 Grain size d (x) and conductivity σ (o) in Sb-doped $BaTiO_3$ ceramics as a function of C_{Sb}, the dopant concentration. (After Daniels et al. [26]).

that combinations of dopants altered the results, for example the use of 0.4 at. % La + 0.15 at. % Mg (an acceptor) produced a grain size comparable to that obtained using 0.1 at. % La only. Kahn [10] stated that using $BaTiO_3$ powders from different sources could change the point of minimum resistivity from 0.2 at. % to 0.4 at. % Nb because of different impurity contents.

Saburi [33] in an early study investigated a large number of dopants, and found that all those which produced the PTC anomaly were characterised by the ceramic having a blue colour, which indicates the presence of Ti^{3+} ions. Jonker [5] noted that specimens in the semiconducting region were dark blue, but that the insulating specimens containing more than 0.6 at. % of La were white and appeared to differ from pure barium titanate only in a small shift of the Curie temperature.

Several explanations for the dependence of room temperature resistivity on donor dopant concentration have been advanced by various authors. Some workers have suggested the formation of insulating layers at the grain boundaries at higher donor concentrations as an explanation. Sauer and Fisher [11] and Tennery and Cook [34] proposed that the segregation of the donor ions at the grain boundaries was responsible for the formation of the insulating layers, and that the minimum value of room temperature resistivity indicated the limit of solubility of the dopant in the barium titanate lattice. However, Basu and Maiti [35] did not observe donor segregation at the grain

boundaries but suggested instead that the insulating layer consisted of a Ti-rich intergranular phase. The insulating layer hypothesis is, however, considered to be unlikely for two seasons. Firstly, donor dopants were found to have high solubility limits (Macchesney and Potter [36], Jonker and Havinga [37] and Ueda and Ikegami [38]), significantly higher than the 0.4 to 0.6 at. % dopant concentration at which the transition to insulating behaviour commonly occurs. (Typical donor dopant solubility limits were 12 at. % for La, ~ 20 at. % for Nb [37] and > 1.0 at. % for Gd [38]). This excludes the possibility of significant donor segregation at grain boundaries. Secondly, Ueda and Ikegami [38] found that highly donor-doped specimens showed normal ferroelectric hysteresis behaviour. If any insulating phase, different from $BaTiO_3$ and assumed to be non-ferroelectric, were to cover the surface of the grains no ferroelectric hysteresis loop would be observed. The existence of an insulating layer at the grain boundaries of highly donor-doped specimens, whether attributable to donor segregation or the presence of a Ti-rich phase, therefore appears unlikely.

Theories have also been advanced accounting for the increase in room temperature resistivity in terms of electrical compensation of the donors. Jonker (1964) [5] postulated that the donor ions are electronically compensated at low donor concentrations, but that a transition to vacancy compensation occurs at high donor concentrations so that insulating behaviour ensues. The mechanism responsible for the transition to vacancy compensation was not explained. A partial

explanation may, however, be found in the work of Drofenik (1987) [39] who suggested that the incorporation of donor ions into the lattice (by a reaction resulting in electronic compensation and the expulsion of oxygen) is not possible, if the change in the free surface energy during grain growth (the driving force of the sintering process) is balanced by the change in the free energy associated with the evolution of oxygen. This condition is satisfied (at oxygen partial pressures corresponding to sintering in air) above a certain dopant concentration, so that dopant incorporation with electronic compensation, as well as grain growth, is suppressed and insulating behaviour ensues.

Other workers have explained the effect in terms of self-compensation of the donors, by assuming that the donors are incorporated with different valencies at equivalent lattice sites (Heywang, 1971 [1]) or with the same valency at different lattice sites (Murukami et al., 1973 [40]). However, the suggested self-compensation mechanisms cannot form the basis of a model which is required to be generally applicable to all donors. In particular, a commonly used donor dopant is lanthanum, which has an ionic radius similar to that of Ba ions and has only one valency state (3+); it is most probably incorporated only as La^{3+} at the Ba sites [10,41] so that self-compensation is unlikely to occur. A self-compensation model is therefore inapplicable in the case of one of the most common donors.

On the other hand it was suggested by Daniels et al. (1978/79) [26] that the increase in the resistivity is due to the combined effects of

the reduction in grain size with increasing donor concentration and the formation of a Ba vacancy-rich insulating grain boundary layer. They assume that at a high donor concentration the grain size is reduced to about 2 μm, a value which is comparable to the width of the Ba vacancy-rich insulating layer, thus rendering the material a complete insulator.

1.7 The Influence of Sintering Atmosphere, Temperature and Cooling Rate on the PTCR Effect

It has been demonstrated experimentally by a number of workers that the resistivity of the ceramic and the magnitude of the PTCR effect are strongly influenced by the sintering temperature, by the oxygen partial pressure in the sintering atmosphere during cooling from the sintering temperature and by the rate at which the cooling takes place. The grain size of the ceramic is also a significant factor. The effects of sintering atmosphere, temperature and cooling rate are due to their influence on the defect structure of the ceramic and its interaction with the donor dopants.

Rutt et al. [32] showed that for pure undoped barium titanate, n-type conductivity was introduced at low oxygen partial pressures and high temperatures, whereas at high oxygen partial pressures and low temperatures the ceramics exhibited p-type conductivity. The n-type conductivity arose as a result of the dominant defects being oxygen vacancies which act as donors, whereas the p-type behaviour was due to the dominance of barium vacancies acting as acceptors. In the case

of air fired ceramics ($Po_2 \simeq 0.2$ atmosphere) n-type conductivity is expected for undoped materials at temperatures of above 1200-1300°C.

For n-doped PTC ceramics the defect structure introduced by the firing conditions is superimposed on the n-type conductivity produced by doping.

Firing in a reducing atmosphere, in which the oxygen partial pressure is low (e.g. a N_2 rich atmosphere), promotes a defect structure rich in oxygen vacancies. This increases the bulk conductivity of the ceramic, but also introduces a negative temperature coefficient (NTC) component to the resistivity which dilutes the PTC effect, with the net effect of a decrease in both the room temperature resistivity and the peak resistivity together with a decrease in the slope of the PTC characteristic [11]. The effect is also evident when specimens with good initial PTC properties are heat treated in a reducing atmosphere and show a subsequent deterioration in PTC properties.

Kahn [10] carried out a detailed investigation of the effects of firing conditions and heat treatment and showed that ceramics sintered in reducing atmospheres and subsequently reoxidised exhibited an increase in resistance which was greater for higher reoxidation temperatures and smaller grain sizes. He also found that the PTCR of specimens fired in an oxidising atmosphere which had been quenched (i.e. cooled extremely rapidly) from the sintering temperature could be improved by reheating and cooling slowly, but that the enhanced PTCR manifested as a higher peak resistivity, was accompanied by some increase in the room temperature resistivity.

Kahn also found that a minimum sintering temperature was necessary to incorporate the dopant into the grains of the ceramic and produce a semiconducting material. He found this minimum temperature to be 1360°C for his material, doped with 0.18-0.28 at. % Nb; below the minimum temperature the specimens contained areas of small brown grains of diameter ~1 μm where grain growth and therefore sintering had not occurred. In the absence of grain growth due to sintering, dopant incorporation had not occurred and these grains were insulating. Rutt et al [32] showed experimentally that the room temperature resistivity of ceramics sintered at high temperature can be raised by equilibriation at low temperature and lowered by equilibriation at higher temperatures; this effect was accompanied by a colour change from blue to brown on reducing the equilibrium temperature.

Additional effects of temperature were described by Ueda and Ikegami [38] who found that Gd-doped specimens quenched after sintering in air at 1375°C exhibited no PTCR, but that specimens cooled slowly in air after sintering, or annealed at high temperature after quenching, did exhibit a PTC effect.

Explanations for all the experimental results were developed by Daniels, Hardtl and Wernicke in a study of the defect kinetics of $BaTiO_3$ ceramics [15,26,40]. As previously stated, when the partial pressure of oxygen in the atmosphere is reduced there is a change from barium vacancies to oxygen vacancies as the dominant defect species, and

therefore a transition from complete vacancy compensation of the donor to partial vacancy compensation. Since the donors have a lower ionization energy (~ 0.1 eV) [25,41] than the vacancies (V_{Ba}' ~ 0.8 eV, V_{Ba}'' ~ 1.6 eV) [25], this transition is accompanied by an increase in conductivity.

For a given atmospheric composition, the concentration of barium vacancies increases as the temperature decreases, and since for the ceramic to be a semiconductor the concentration of barium vacancies must not exceed that of the conduction electrons derived from the dopant atoms, there exists a specific temperature above which a ceramic in equilibrium will be a semiconductor and below which it will be an insulator. In air this temperature was 1200°C for the case considered by Daniels and so specimens quenched in air were only semiconducting if they were initially in equilibrium above 1200°C.

In the case of slowly cooled materials, the defect equilibrium initially follows the decreasing temperature. As the temperature falls further, equilibrium restoration can no longer be maintained for kinetic reasons and the defects become frozen-in so that the final defect distribution and hence the room temperature conductivity is determined largely by the cooling rate and the initial temperature from which cooling began. Diffusion experiments have also demonstrated [15] that equilibrium restoration is controlled by the very slow diffusion of barium vacancies from the grain boundaries into the interior of the grains, giving rise to a grain boundary layer rich in barium vacancies.

At an appropriate cooling rate in air, it is possible to maintain equilibrium near the grain boundaries to temperatures below 1200°C, when total vacancy compensation takes over and an insulating grain boundary layer is formed.

This explains the observations of Kahn that the increase in maximum resistivity induced by reoxidation is greater in the case of smaller grains where the equilibrium restoration extends further into the grains and at higher reoxidation temperatures where the barium vacancy diffusion rate is higher. The explanations due to Daniels et al. are also consistent with the results of subsequent investigations by Al-Allak, Russell and Woods [42]. Al-Allak et al. annealed specimens of Ho-doped barium titanate ceramics in air at 1220°C for periods of up to 27 hours while cooling to room temperature after sintering at 1320°C. They found that the annealing process resulted in an increase in the value of the maximum resistivity and an increase in the steepness of the resistivity-temperature curve in the region of the PTCR transition. This was attributed to the formation of a resistive grain boundary region in series with the space charge layer; dielectric measurements at A.F. and R.F. revealed that the resistive layer was confined to the grain boundary region and did not diffuse throughout the entire grain bulk, even for the longest annealing time. These changes were explained in terms of an increase in the acceptor state density, consistent with Daniels et al.'s explanation.

1.8 Summary

Daniels' modification of the Heywang model explains satisfactorily most aspects of the experimentally observed PTCR effect in donor doped $BaTiO_3$ ceramics. Certain aspects of the PTCR effect are, however, not fully resolved by Daniels' model.

The first aspect is the transition from conductive to insulating room temperature behaviour at high donor dopant concentration. The transition coincides with a marked reduction in grain diameter which Daniels postulates leads to the grain boundary depletion layers filling the entire grain thus producing insulating behaviour. This seems plausible, but Daniels furnishes no direct proof of the postulate and other possible explanations must also be considered, such as changes in the nature or density of the grain boundary acceptor states.

The second aspect the effect of annealing, and reduction and reoxidation, on the PTCR effect. In view of the low mobility of Ba vacancies, both the disappearance of the PTCR on reduction and its appearance on reoxidation occur too rapidly for Ba vacancy diffusion alone to be responsible, according to the Daniels model. However, Al-Allak et al. have proposed a modification to the model which includes a resistive layer in series with the grain boundaries and the effects of rapidly diffusing oxygen vacancies at the grain boundaries, in order to overcome these shortcomings.

References

1. Heywang, W., J. Mat. Sci., 6 (1971) 1214.
2. Kay, H. F. and Vonsden, P., Phil. Mag., 40 (1949) 1019.
3. Lines, M. E. and Glass, A. M., Principles and Applications of Ferroelectrics and Related Materials, Oxford University Press (1979) 136.
4. Goodman, G., J. Am. Ceram. Soc., 46 (1963) 48.
5. Jonker, G. H., Solid St. Electron., 7 (1964) 895.
6. Heywang, W., Solid St. Electron., 3 (1961) 51-8.
7. Jonker, G. H., Advances in Ceramics, Vol. 1, Am. Ceram. Soc., (1981).
8. Kulwicki, B. M., Purdes, A. J., Ferroelectrics, 1 (1970) 253.
9. Haanstra, H. B., Ihrig, H., J. Am. Ceram. Soc., 63 (1980) 288.
10. Kahn, M., Ceram. Bull., 50 (1971) 676.
11. Sauer, H. A., Fisher, J. R., J. Am. Ceram. Soc., 43 (1960) 297.
12. Daniels, J., Härdtl, K. M., Philips Res. Repts., 31 [6] (1976) 489-504.
13. Daniels, J., Philips Res. Repts., 31 [6] (1976) 505-515.
14. Hennings, D., Philips Res. Repts., 31 [6] (1976) 516-525.
15. Wernicke, R., Philips Res. Repts., 31 [6] (1976) 526-543.
16. Daniels, J., Wernicke, R., Philips Res. Repts., 31 [6] (1976) 544-559.
17. Gerthsen, P., Härdtl, K. H., Z. Naturf., 18a (1963) 423.
18. Rehme, H., Phys. Stat. Sol., 18 (1966) K101.
19. Ihrig, H., Klerk, M., App. Phys. Lett., 35 (1979) 307.
20. Gerthsen, P., Hoffmann, B., Solid. St. Electron, 16 (1973) 617.
21. Haanstra, H. B., Ihrig, H., Phys. Stat. Sol. (a), 39 (1977) K7.
22. Ihrig, H., Phys. Stat. Sol. (a), 47 (1977) 437.

23. Ihrig, H. Puschert, W., J. App. Phys., 48 (1977) 3081.

24. Hoffmann, B., J. App. Phys., 50 (1979) 1156.

25. Ihrig, H., J. App. Phys., 50 (1979) 1158.

26. Daniels, J., Härdtl, K. H., Wernicke, R., Philips Tech. Rev., 38 [3] (1978/79) 73.

27. Seuter, A., Philips Res. Repts. Suppl., 3 (1974).

28. Schmelz, H., Phys. Stat. Sol., 35 (1969) 219.

29 Kahn, M., J. Am. Ceram. Soc., 54 (1991) 452.

30. Murukami, T., Miyoshita, T., Nakakara, M., Sekini, E., J. Am. Ceram. Soc., 56 (1973) 294-7.

31. Fukami, T., Tsuchiya, H., Jpn. J. Appl. Phys., 18 (1979) 735.

32. Rutt, J. C., Fulson, F. C., Laughlan, G. B., Proc. 25th Electron. Components Conf., IEEE (1975).

33. Saburi, O., J. Phys. Soc. Jpn., 14 (1959) 1159.

34. Tennery, U. J., Cooke, R. L., J. Am. Ceram. Soc., 44 (1961) 187.

35. Basu, R. N., Maiti, H. B., Proc. IEEE Int. Symp. Appl. of Ferroelectrics, (Lehigh Univ., U.S.A.), ed. Van Wood, (New York : IEEE), (1986) 685.

36. Macchesney, J. B., Potter, J. J., J. Am. Ceram. Soc., 48 (1965) 81.

37. Jonker, G. H., Havinga, E. E., Mat. Res. Bull., (1982) 345.

38. Ueda, I., Ikegami, S., J. Phys. Soc. Jpn., 20 (1965) 546.

39. Drofenik, M., J. Am. Ceram. Soc., 70 (1987) 311-4.

40. Wernicke, R., Phys. Stat. Sol. (a), 47 (1978) 139.

41. Ihrig, H. and Hennings, D., Phys. Rev. B, 17 (1978) 4593.

42. Al-Allak, H. M., Russell, G. J., Woods, J., J. Phys. D, 20 (1987) 1645.

CHAPTER 2

EXPERIMENTAL METHOD

2.1 Introduction

Semiconducting barium titanate ceramics were prepared from barium titanate powder into which small quantities of donor ions were incorporated as an impurity. A conventional ceramic processing route was followed, using heat treatment of specimens at high temperatures to incorporate the donor ions into the barium titanate lattice and to induce sintering leading to densification and grain growth. The resulting ceramics were studied using a scanning electron microscope in secondary electron emission and energy dispersive X-ray analysis modes to determine their microstructure and composition. Electrical properties of the ceramic grain boundaries both below and above the Curie temperature were investigated using the scanning electron microscope in electron beam induced current and electron barrier voltaic effect modes. Optical polarized light microscopy was used to investigate the ferroelectric domain properties of the ceramics below and above the Curie temperature, and to study the effects of external electric fields on the optical properties. Electric and dielectric measurements were used to determine the electrical properties of the ceramics. Measurements of resistance were carried out as the temperature was raised through the Curie temperature, whence resistivity-temperature characteristics for the materials were derived. Resistivity measurements as a function of applied electric field at room temperature were used to investigate non-ohmic behaviour of the ceramic. A.C. impedance measurements were carried out at room

temperature in order to separate the component of resistance arising from the grain bulk from that attributable to the grain boundaries of the ceramic.

The electrical properties were then analysed in terms of the Heywang model to determine the height of the grain boundary potential barriers and the characteristics of the grain boundary acceptor traps.

The remainder of this chapter describes the experimental methods used for the preparation of the ceramic specimen and their microstructural, optical and electrical characterization. The methods used for analysis of the results are described in subsequent chapters.

2.1.1 Specimen Preparation - Powder Processing

The barium titanate ceramics used in these studies of the PTCR effect were prepared according to a conventional route [1,2], incorporating various concentrations of holmium, the donor dopant, between 0.05 and 0.8 at. % according to the formulation $Ba_{1-x}Ho_xTiO_3$. Holmium oxide was selected as the donor dopant because of the similarity in size between the Ho^{3+} and Ba^{2+} ions, so that holmium will readily substitute for barium in the crystal lattice. A commercial grade of $BaTiO_3$ (Mandoval grade 6, mean particle diameter 0.8 μm) was used as the precursor material with holmium added in the form of Ho_2O_3 to give the required donor dopant concentration in each case. Sufficient TiO_2 was added to produce a 0.5 mol. % excess of Ti over the stoichiometric quantity to produce a titania-rich phase ($Ba_6Ti_{17}O_{40}$). This

forms a eutectic with $BaTiO_3$, which melts at 1320°C and so promotes liquid phase sintering at comparatively low temperatures [2]. Furthermore, Daniels [3] considered the presence of excess Ti in the second phase assisted the formation of Ba vacancies. In addition a small amount (0.9 mol. %) of SiO_2 was added to the mixture to act as a sintering aid. (It is generally accepted that the TiO_2 and SiO_2 combine during sintering to form a glassy intergranular phase [4,5,6] which assists the sintering process without fundamental influence on the electrical properties of the ceramic). The constituents of each precursor mixture were weighed out then ball milled together in deionized water (in the proportion water:precursor = 1.4:1 by weight) for 12 hours in a polyethylene jar, using spherical agate milling media. The mixture was recovered by filtration, and a quantity of organic binder solution (0.3 x weight of solids of an aqueous solution of 3.5 % w/w glucose and 3.5% w/w polyethylene glycol) added. After drying the material was granulated, sieved to give particle sizes between 90-500 μm, and pressed into small pellets of diameter 5 mm and thickness ~1 mm using a hydraulic press to apply a load of 6000 N to a SiC lined die.

The properties of ceramics are known to be sensitive to composition and processing history, especially when their parameters are determined by small variations in impurity concentration such as the donor dopant in $BaTiO_3$ PTCR ceramics. In particular, contamination with small amounts of certain 3d transition elements [7], e.g. Mn, Fe, which substitute for Ti^{4+} at lower valency thus acting as

acceptors, can considerably modify the PTCR behaviour. Close control of composition was therefore exercised throughout the specimen preparation process by maintenance of a consistent experimental method and careful equipment design. The milling process was identified as a potential source of contamination : accordingly a polyethylene milling jar, and media made of agate (a very hard form of silica) were selected. Since polyethylene is completely combustible, any contamination from the container walls would be removed during firing, and since a constant milling time was used, contamination from the agate media would result only in the addition of a small quantity of SiO_2 to the second phase composition of each mixture. All equipment was washed with deionized water before use and the powdered ceramic precursors kept in closed containers before and after mixing to prevent contamination.

2.1.2 Specimen Preparation - Sintering

The pressed 'green' pellets were then fired in a tube furnace to sinter them into the ceramic form. The pellets were placed on a setter plate which was covered with a thin platinum foil in order to prevent contamination of the ceramic by reaction with the setter material. Firing was carried out according to the profile in fig. 2.1; the specimens were initially maintained at 600°C for 60 minutes in order to ensure complete combustion of the organic binder. The temperature was then increased at a rate of 900°C h^{-1} to the sintering temperature of 1380° or 1420°C and held for 60 minutes while sintering occurred [8]; after this

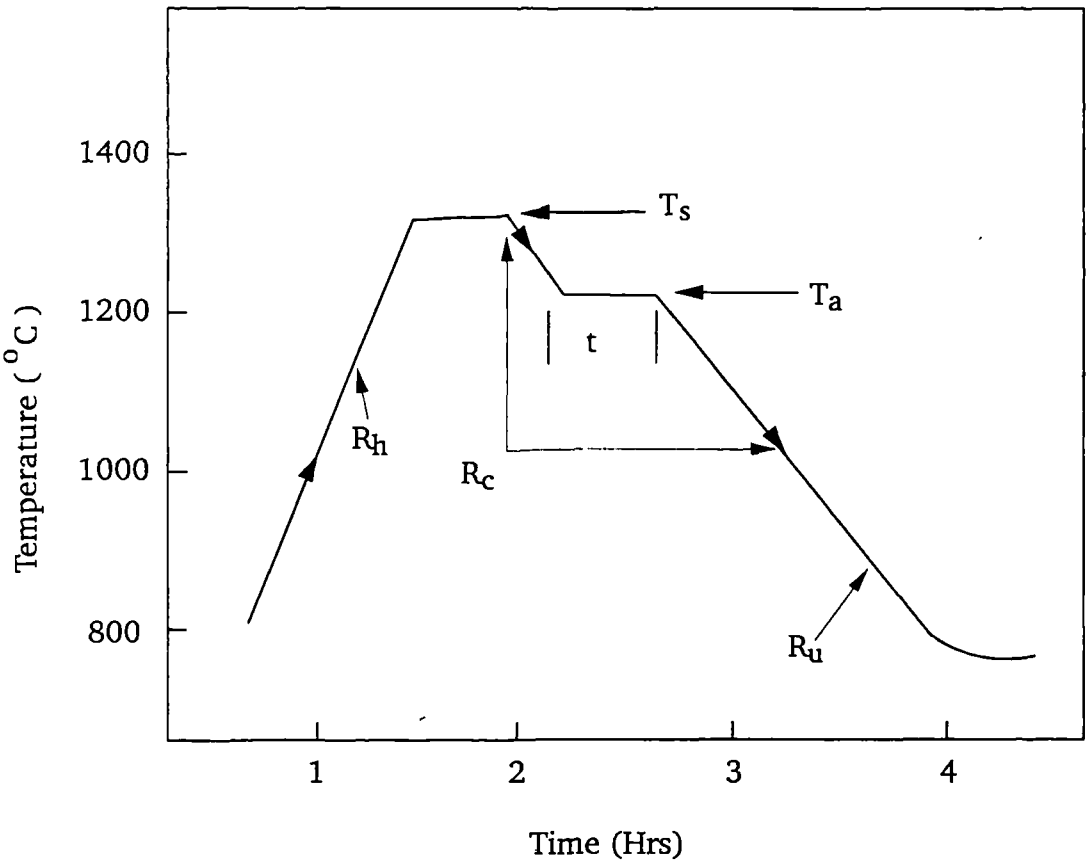

Figure 2.1 Temperature profile used in the preparation of PTCR samples (T_s = sintering temperature, T_a = annealing temperature, t = annealing time, R_h = heating rate, R_c = controlled cooling rate and R_u = uncontrolled cooling rate)

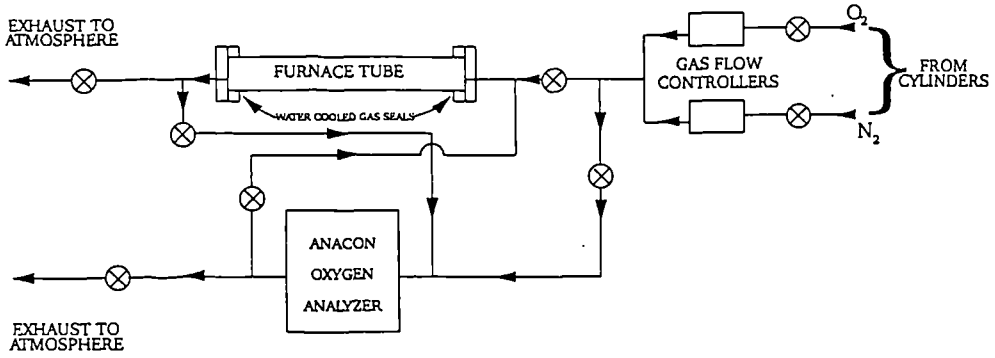

Figure 2.2 Schematic diagram of gas mixing system used in controlled ambient firing experiments.

the furnace was cooled at 300°C h^{-1} down to 800°C, then at its natural cooling rate to ambient temperature. In the case of the annealing study described in chapter 4, cooling was interrupted while annealing took place at 1220°C for a variable period. The firing profile of the furnace was regulated by a Eurotherm programmable temperature controller.

A controlled atmospheric composition was maintained within the furnace tube during firing by passing through a mixture of oxygen and nitrogen at a flow rate of 1 ℓ min^{-1}, in a proportion of O_2:N_2 = 21:79 which was identical to the composition of air. The composition of the gas mixture was measured using an Anacon oxygen analyser; this was arranged so as to be capable of measuring the composition of gas entering or leaving the furnace tube, by means of suitable valve connections (fig. 2.2). The exhaust gas measurement facility was used to check that combustion of the organic binders was complete after 60 minutes at 600°C by comparison of the inlet and exhaust gas composition.

The furnace was also used in conjunction with the atmosphere control facility for the reduction and reoxidation treatment of specimens (chapter 4). Reduction was carried out by heating the specimens to 1220°C in a flow of N_2 (i.e. oxygen-free), while reoxidation entailed heating in the standard N_2 /O_2 'air' mixture.

2.2 Polarized Light Microscopy

A polarizing optical microscope was used to study the behaviour of the ferroelectric domains within the ceramic grains and their

interaction with the grain boundaries, by exploiting the optical anisotropy and birefringence caused by the non-centrosymmetric crystal structure of the tetragonal phase of $BaTiO_3$.

2.2.1 Specimen Preparation

Specimens for optical microscopy were prepared from PTCR ceramic pellets, using standard metallographic polishing and lapping techniques on Logitech lapping machines. Successively finer grades of aluminium grit abrasive were used, down to a final particle size of 0.25μm, to produce a final specimen thickness of 30 μm, the standard thickness used in polarized light microscopy. This thickness corresponded to 1-2 grain diameters for the ceramics studied, and was found to give good light transmission.

2.2.2 Microscopy Technique

The optical specimens were studied using a standard polarizing light microscope, in unpolarized light and then in polarized light between crossed polarizers (i.e. with the upper and lower polarizers' planes of polarization mutually perpendicular) in order to observe the ferroelectric domain structure. Specimens were rotated with respect to the plane of polarization of the incident light by means of the microscope stage and the effect on the domains observed. Photo-micrographs of specimens were taken using a 35 mm camera attached to the eyepiece, finding the correct exposure by bracketing.

Selected specimens were mounted on a heated stage and observed between crossed polars as the specimen temperature was

increased from room temperature up to and beyond the transition temperature, in order to study domain behaviour at the PTCR transition. Specimen temperature was measured by a thermocouple fitted to the stage. Again the specimens were photographically recorded.

2.2.3 Optical Effects of External Electric Fields

In order to investigate the effects of external electric fields on the domain structure, pairs of silver electrodes were thermally evaporated onto some of the specimens. The electrodes were circular in shape, of diameter 1 mm and with centres 2 mm apart giving an electrode separation of 1 mm at the closest point: metal thickness was ~ 2000 Å. After mounting the specimens on a glass slide, thin copper wires were attached to the electrodes using silver paint to permit connection to a high voltage power supply. The optical properties of the specimen were then studied, using crossed polars, as voltages of up to ~ 300 V were applied from the voltage supply.

2.3 Scanning Electron Microscopy

2.3.1 Microstructural Characterization

A Cambridge Instruments Stereoscan S600 scanning electron microscope (SEM) operating in secondary electron emission (SE) and energy dispersive X-ray analysis (EDX) modes was used for the microstructural characterization of ceramic specimens.

2.3.1.1 Secondary Electron Emission (SE) Mode

In SE mode [9], the SEM scans an electron beam ~ 100 Å in diameter across the area of the specimen under investigation. A small proportion of the beam (primary) electrons is elastically scattered from the specimen surface as high-energy backscattered electrons. The remainder undergo inelastic collisions, generating secondary electrons which can escape from the region 50-500 Å below the specimen surface. The number of secondary electrons emitted is influenced primarily by the surface topography and also by the secondary emission efficiency of the surface. An Everhart-Thornley detector collects the secondary electrons; this consists of a scintillator, screened by a Faraday cage, and connected to a photomultiplier tube. The low energy secondary electrons are accelerated by a potential of +14 kV applied to the scintillator in order to give them sufficient energy to excite scintillations. The Faraday cage serves to screen the primary electron beam from the influence of this potential, and is biased at +250 V to collect the secondary and backscattered electrons. Scintillations produced when the collected electrons are accelerated onto the scintillator are guided by a light pipe onto the cathode of the photomultiplier tube, initiating a cascade of electrons and producing high gain while introducing very little noise. The output signal of the photomultiplier tube is then applied to the z-modulation (brightness) of a CRT which is scanned synchronously with the electron beam to produce a video image of the surface topography of the specimen. With a well-focused electron beam

it is possible to obtain very high levels of magnification combined with good resolution (< 100 Å) and a very large depth of field (due to the small wavelength of the electrons).

Electron microscopy was performed using the SEM in SE mode mostly on the as-fired surfaces of the ceramic specimens in order to observe the microstructure and to determine the average grain size, shape and distribution, together with the observation of any additional phase on the specimen surface.

2.3.1.2 Energy Dispersive X-ray Analysis (EDX)

Energy dispersive X-ray analysis [10] was carried out on specimens to determine their chemical composition by means of a Link Systems 860 EDX analyser fitted to the Cambridge Instruments S600 SEM. This X-ray microanalysis technique relies upon the emission of characteristic X-ray wavelengths from the specimen on bombardment by the SEM electron beam. The primary electrons eject core (and other) electrons as secondary electrons, and the empty core energy levels are subsequently filled by relaxation of electrons from higher energy levels, accompanied by the emission of X-rays of characteristic frequency. For instance, electrons from the L, M or N etc. shells may relax into an empty K shell emitting characteristic X-ray spectral lines denoted respectively K_α, K_β, K_γ etc. The frequency, ν, of each X-ray spectral line is given by Moseley's law,

$$\sqrt{\nu} = a\,(Z - b) \tag{2.1}$$

where Z is the atomic number and a and b are constants. Measurement of the energy, and thus the frequency, of the emitted X-ray photons therefore permits analysis of the elemental composition. The electron beam of the SEM may be positioned onto specific features of the specimen observed by imaging in SE mode; since the beam width is only ~ 100 Å, this enables the analysis of sub-micron features.

The analyser consists of a lithium-drifted silicon reverse-biased p-n junction detector, cooled by liquid nitrogen. The incident X-rays pass through a Be window and impinge on the depletion region of the junction, forming electron-hole pairs. Since the energy of each pair is 3.8 eV, much less than the energy of the incident X-ray photon, a large number of electron-hole pairs are generated. This results in a current pulse proportional to the energy of the incident X-ray photon. The distribution of numbers and magnitudes of current pulses is determined using a multi-channel analyser and stored in its memory. This stored distribution is then transmitted to a computer for elemental identification by comparison of the energy peaks in the stored distribution with the known spectral positions of the characteristic X-ray lines of all elements. It may be seen that the frequency of the characteristic X-rays is inversely proportional to the square of the atomic number; since most media absorb longer wavelength X-rays more strongly, it follows that EDX is less sensitive to lighter elements.

This analyser could not detect elements having an atomic number less than 11(Na) since the characteristic X-rays could not then penetrate the Be detector window. The detection limit for any single element was ~1%, the limit being determined by the signal/noise ratio of the detection system.

EDX analysis was used to analyse the composition of grains and intergranular phases of as-fired and polished and etched specimens. It was not, however, possible to investigate variations in dopant concentrations within specimens using this technique because of the high detection limit.

2.3.2 Grain Boundary Electrical Characterization

The Cambridge Instruments S600 SEM was also used to study electrically active structural features, particularly grain boundaries, by the extraction of electron-hole pairs generated by interaction of the electron beam with the specimen. This was attempted with the SEM operating in electron beam induced current (EBIC) and electron barrier voltaic effect (EBVE) modes, both at room temperature and at temperatures above the PTCR transition.

2.3.2.1 Electron Beam Induced Current (EBIC) Mode

The EBIC technique uses a potential barrier (in the form of a reverse-biased Schottky or p-n junction) to separate the electrons and holes which are produced by the incident electron beam [11].

Provided that the barrier lies within about a diffusion length of the point at which the electron-hole pairs are generated, the barrier

separates the charge carriers which are collected and the resulting current amplified and applied to the z-modulation of the synchronously scanned CRT display. As the electron beam is scanned across the specimen and traverses areas of different charge carrier recombination lifetime, a change in the specimen current occurs which appears as a change in contrast on the video display image.

The specimen configuration selected for the EBIC investigations was similar to that first used by Ralph et al.[12]. Specimens were polished down to a thickness of ~30μm by standard metallographic techniques, using successively finer grades of alumina grit, and finally 1μm diamond paste, as the polishing media. A Schottky barrier electrode consisting of a 200Å thick layer of gold was applied to one surface by thermal evaporation, and an ohmic electrode formed from a 2000Å thick layer of titanium protected from oxidation by a 2000Å thick layer of gold was evaporated onto the opposite surface; electrode diameters of ~2mm were used. The specimens were mounted within the SEM on an electrically heated stage with the Schottky contact uppermost and contact with the electrodes was established, as shown in fig. 2.3. With the Schottky junction reverse-biased, the incident electron beam penetrated the thin gold electrode layer before interacting with the specimen to generate charge carrier pairs. The carriers were separated by the barrier and formed the EBIC current which was amplified by a Matelec-5 amplifier connected to the SEM; the resulting signal was then applied to the z-modulation input of the CRT to

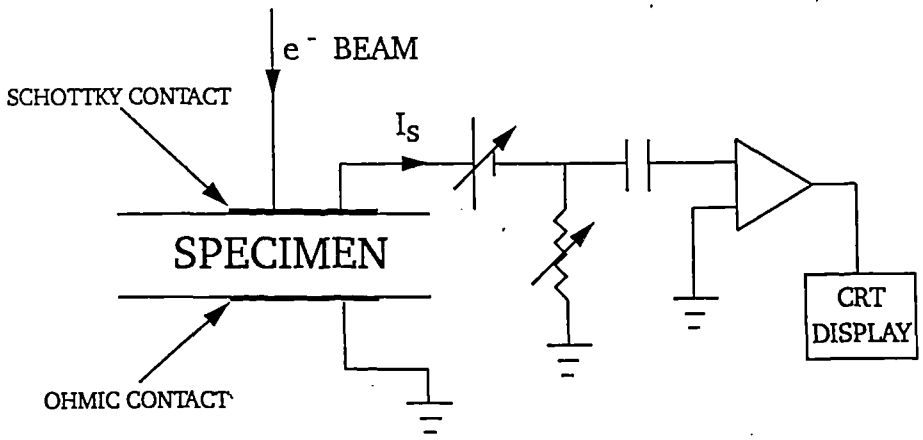

Figure 2.3 Schematic diagram of circuit used in EBIC measurements.

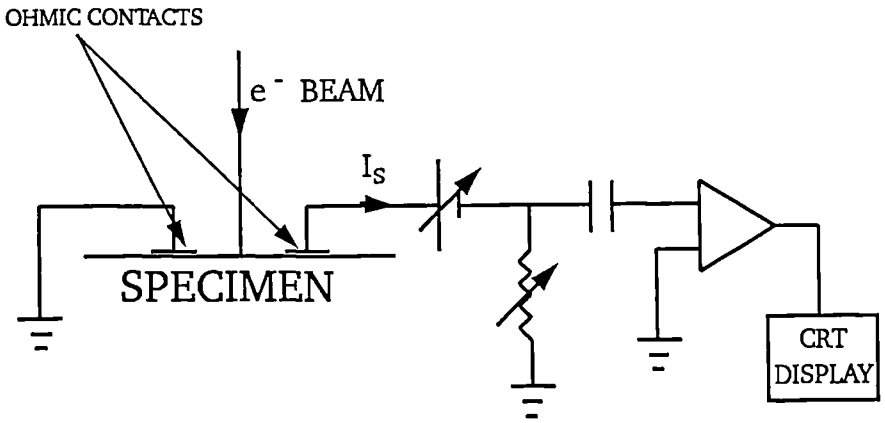

Figure 2.4 Schematic diagram of circuit used in EBVE measurements.

produce a video image. Thin specimens (equivalent to 1-2 grain diameters thick) were used to reduce the number of resistive grain boundaries traversed by the EBIC current in the electrical circuit in order to minimise electrical noise. The heated stage was used to vary the specimen temperature in order to carry out EBIC investigations above and below the PTC transition temperature.

2.3.2.2 Electron Barrier Voltaic Effect (EBVE) Mode

The EBVE technique is implemented using two closely-spaced ohmic electrodes on the specimen surface (fig. 2.4). A potential V is applied between the electrodes and causes a current I_V to flow through the surface region. The electron beam scans the specimen surface in the region between the electrodes and generates electron-hole pairs which are separated by the applied electric field to give an additional contribution to the current, I_B. Thus the total specimen current, I_S, is given by

$$I_S = I_V + I_B \qquad (2.2)$$

The current is amplified by the Matelec-5 amplifier and applied to the z-modulation input of the CRT display in an analogous manner to the EBIC mode. Variations in charge carrier recombination lifetime as the electron beam is scanned across the surface result in changes in I_B and therefore in total specimen current I_S giving rise to contrast variation on the video image. Since image formation depends on the detection of small variations in I_B in the presence of a large background current I_V,

this technique is more susceptible to extraneous electrical noise than EBIC. However, the EBVE technique has the advantage of being usable where the good Schottky contacts required for EBIC cannot be obtained.

Ceramic specimens were prepared for EBVE investigation by polishing one face only using the same metallographic techniques as for EBIC; the thickness of the polished EBVE specimens was approximately 2 mm. The polished surfaces were then etched using a solution of 5% HF : 10% HCl for ~ 60 seconds, followed by repeated rinsing in deionized water; this was done to remove polishing damage and to reveal the grain structure. Ohmic electrodes of diameter 1 mm with centres 2 mm apart were then applied to the polished surface by thermal evaporation of a layer of titanium 2000 Å thick, followed by superimposed layer of gold, also 2000 Å thick, to protect the Ti ohmic layer from oxidation.

The specimens were mounted on *the electrically heated stage* within the SEM and electrical contact made between the specimen electrodes and the EBVE circuit by means of thin gold wires held in place by mechanical pressure. This experimental arrangement was then used to study the specimens in EBVE mode both above and below the PTCR transition temperature.

2.4 Electrical Measurements

2.4.1 Resistivity - Temperature Measurements

Resistance was measured using a two-probe technique under the control of a BBC microcomputer; a diagram of the experimental arrangement is given in fig. 2.5. A two-probe technique was selected since the contact resistances were assumed to be negligible. Up to 10 specimens at a time were placed in the air oven, where they were surrounded by a copper block to minimise temperature fluctuations, the temperature being controlled by the BBC microcomputer via a Eurotherm temperature controller. At each set temperature a bias of 2V was applied to each specimen in turn and the current passing through the samples was measured by a specially adapted Thurlby 1905a multimeter. Resistance and resistivity values were calculated as the mean of 1000 readings and stored by the microcomputer for plotting at the end of the measurement run. The measurement chamber temperature was increased to each set point at a rate of 3°C/min and held for 4 minutes after reaching the set point before commencing measurement to ensure an even specimen temperature.

Specimens were prepared for measurement by gentle polishing with emery paper to ensure flat surfaces and produce specimens of approximately the same thickness (usually ~ 1 mm). Ohmic electrodes were applied by rubbing an alloy of indium and gallium in the ratio of 2:1 by weight onto the polished surfaces. This material was selected because both components have low work functions, ensuring the absence

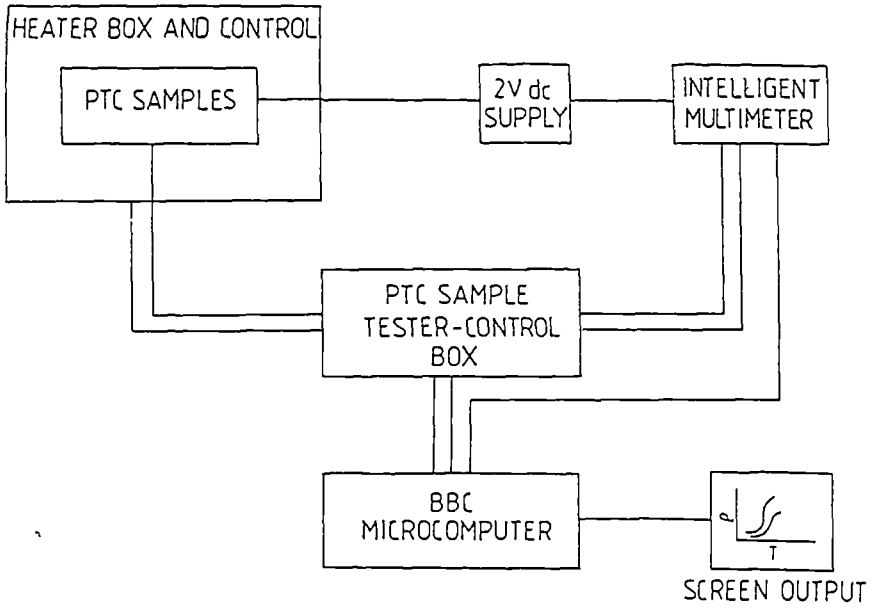

Figure 2.5 Block diagram of the experimental arrangement used in Resistivity-Temperature measurements.

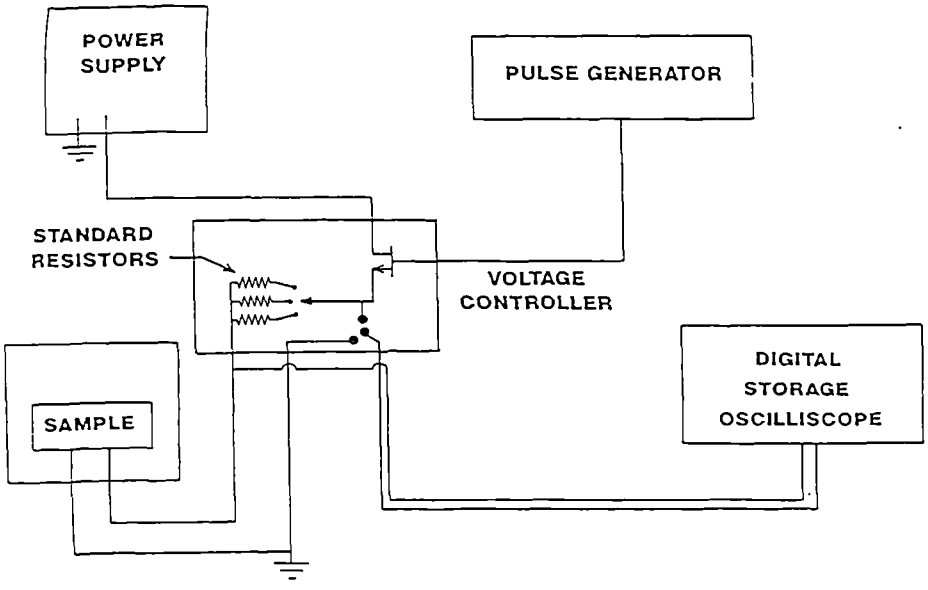

Figure 2.6 Block diagram of the experimental arrangement used in the pulsed Resistivity-Voltage measurements.

of electron barriers at the contact and therefore producing ohmic behaviour. Furthermore the gallium is an efficient oxygen getter which removes adsorbed surface oxygen which would otherwise create a resistive depletion layer at the contact interface. For the resistivity measurements, four or five specimens from each batch were measured at a time in order to ensure reproducible results and to determine the amount of random experimental error.

2.4.2 Resistivity-Voltage Measurements

These measurements were carried out to investigate non-ohmic resistance effects arising at high applied electric fields. The experimental apparatus is schematically illustrated in fig. 2.6. Ohmic electrodes were applied, as described above, to the specimen, which was connected in series with a resistance of known value, and single short (~ 1.5 ms) pulses (> system time constant) of the selected voltage then applied across the specimen. The voltages across the resistor and the specimen were measured using a Gould digital storage oscilloscope and used to calculate the current through the circuit and thus the resistivity of the specimen, together with the applied electric field. Repetition of the measurement at different applied voltages permitted determination of the dependence of the resistivity of the specimen on the applied electric field. Because of the need for high fields, thin specimens which had been polished with emery paper to ~ 0.7 mm thickness were used, to allow the application of the required field with the available voltage supply.

2.5 Dielectric Measurements

According to a simple model developed from AC theory by Basu and Maiti [13], plotting the real versus the imaginary part of the AC impedance of donor doped barium titanate ceramics permits the separation of the grain bulk and grain boundary resistance of the material. In order to study the distribution of resistance between the grain bulk and grain boundaries, AC impedance measurements were carried out at room temperature at frequencies up to 50 MHz using a Marconi Instruments TF1313A AC impedance bridge and a Hewlett Packard HP4342A Q meter. The AC bridge was employed at frequencies between ~ 100 Hz and 40 kHz, and the Q meter was used at higher frequencies.

2.5.1 A.C. Bridge Measurements

Ohmic electrodes were applied to thin specimens as described previously by rubbing In/Ga alloy onto the flat surfaces. The specimens were placed in an electrically screened capsule and connected to the bridge with short, air insulated leads of negligible impedance. An A.C. signal at a given frequency was applied to the bridge from an external signal generator and the bridge balanced by adjustment of the internal variable capacitance and resistance to give no signal on the oscilloscope used as a detector.

Figure 2.7 illustrates the equivalent circuit of the A.C. bridge. The bridge consisted of four impedances, where Z_1 and Z_2 were pure resistances and Z_3 and Z_{SP} were equivalent to parallel combinations of resistance, R_3 and R_{SP}, and capacitance, C_3 and C_{SP}, which respectively

represented the bridge characteristic and specimen parameters. At balance, where the impedances were such that no signal appeared at the detector, elementary circuit theory gives

$$\frac{Z_1}{Z_1 + Z_{SP}} = \frac{Z_2}{Z_2 + Z_3} \tag{2.3}$$

Since $Z_1 = R_1$, $Z_2 = R_2$, $Z_3 = R_3/(1 + j\omega C_3 R_3)$ and $Z_{SP} = R_{SP}/(1 + j\omega C_{SP} R_{SP})$ equation (2.3) may be written

$$\frac{R_1 (1 + j\omega C_{SP} R_{SP})}{R_1 + R_{SP} + j\omega C_{SP} R_{SP} R_1} = \frac{R_2 (1 + j\omega C_3 R_3)}{R_2 + R_3 + j\omega C_3 R_3 R_2} \tag{2.4}$$

Simplification and separation of the real and imaginary parts gives an expression for the capacitance of the equivalent parallel circuit of the specimen

$$C_P = R_2 \times C_3 / R_1. \tag{2.5}$$

The parameter C_3 / R_1 was a constant which was incorporated in the calibration of the dial controlling the variable balancing resistor, R_2, so that the value of C_P could be read directly from the dial graduations.

The second balancing adjustment controlled the internal variable resistance R_3, with the dial calibrated to give the value of Q ($1/\tan \delta$, the dielectric loss factor) of the specimen at balance.

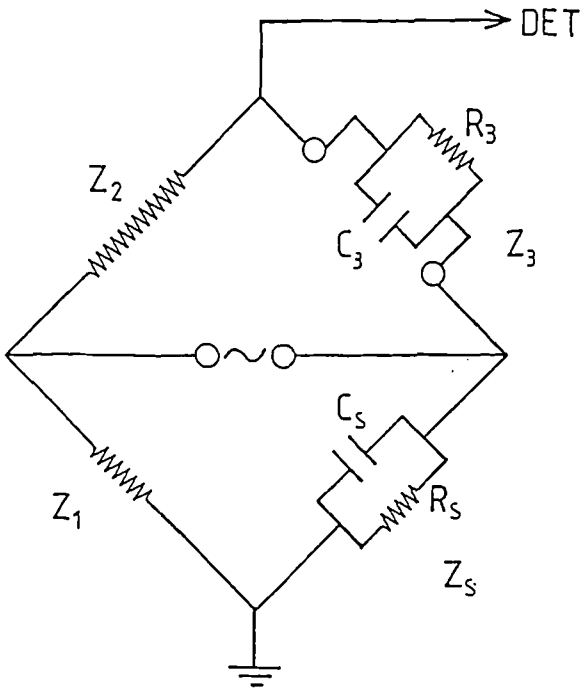

Figure 2.7 Equivalent circuit for the A.C. bridge measurements.

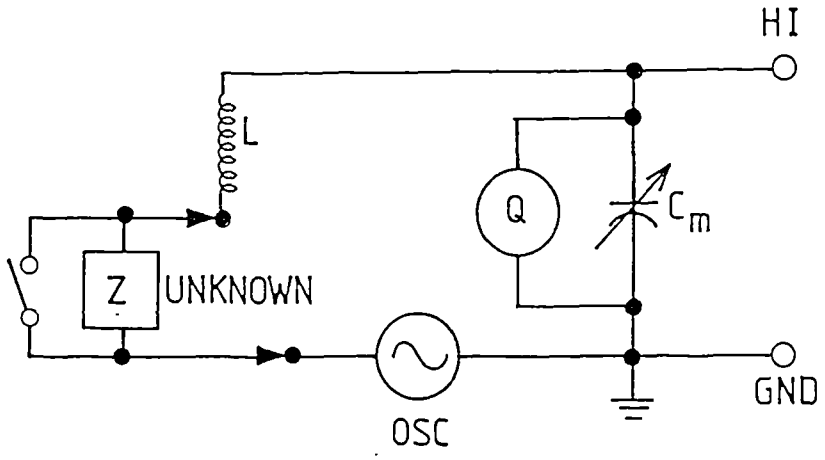

Figure 2.8 Schematic circuit for Q meter measurements.

The analysis of the A.C. impedance measurements requires the data to be expressed in terms of a series capacitance-resistance equivalent circuit for the specimens, whereas the A.C. bridge measured data only in terms of the parallel equivalent circuit. A conversion was therefore carried out as follows : consider the impedance of the parallel and series equivalent circuits, Z_P and Z_S respectively, defined in terms of R_P, C_P, R_S and C_S, the respective resistance and capacitance of each circuit. Z_P is identical to Z_S, since each circuit represents the same specimen. Hence

$$Z_P = \frac{R_P}{1 + j\omega C_P} = \frac{R_P\,(1 - j\omega C_P R_P)}{1 + \omega^2 C_P^2 R_P^2} \tag{2.6}$$

and

$$Z_S = R_S + \frac{1}{j\omega C_S} \tag{2.7}$$

where $\omega = 2\pi f$ and f is the frequency of the applied signal. Since Q, for a parallel equivalent circuit is defined as $Q = \omega R_P C_P$, equation (2.6) can be rewritten

$$Z_P = \frac{R_P}{1 + Q^2} - j\,\frac{Q^2}{\omega C_P\,(1 + Q^2)} \tag{2.8}$$

Since $Z_P = Z_S$ it follows that

$$R_S = R_P \left(\frac{1}{1 + Q^2} \right) \tag{2.9}$$

and

$$C_S = C_P \frac{(1 + Q^2)}{Q^2} \tag{2.10}$$

For the series circuit, Q is defined as $Q = X_S / R_S$ where X_S is the series reactance, thus

$$X_S = Q \times R_S \tag{2.11}$$

Since a balance is obtained at each frequency with unique values of C_P and Q, then R_S and X_S may be calculated.

Errors in the measured capacitance values due to fringing of the electric field at the sample edges were avoided by the use of thin specimens. For disc electrodes without a guard ring, i.e. where the electrodes extend to the edge of the specimen, and the electrode is much thinner than the specimen thickness, t, the fringing capacitance is given by [14]

$$C_e = (0.0087 - 0.00252 \ln (t)) \times P \quad pF \tag{2.12}$$

where P is a constant given by $P = \pi \times (2r + t)$ and 2r is the specimen diameter (2r, t in mm). The fringing capacitance appears in parallel with the apparent specimen capacitance, introducing errors into the

measured values. For the present experiments the specimens were 5mm in diameter and ~ 0.7 mm thick, giving C_e ~ 0.1 pF. This was several orders of magnitude smaller than typical specimen capacitances (~ a few μF) and was therefore regarded as negligible. Errors arising from self-heating of the specimens were also negligible since the amplitude of the applied signal did not exceed 750 mV.

2.5.2 Q-meter Measurements

Measurements at the higher frequencies were carried out using the Q-meter, assuming the series resistance-capacitance equivalent model. Thin specimens were coated with In/Ga alloy ohmic electrodes and connected to the Q-meter by short air-insulated leads of negligible impedance as described earlier. Figure 2.8 gives a schematic circuit diagram of the Q-meter, which operates on the principle of resonance of the inductor, Q-meter and specimen in series.

The measurements were carried out as follows. Firstly the Q and C values of the meter alone, in series with the inductor, were obtained by shorting across the specimen and tuning the variable capacitor C_m to give maximum deflection on the meter. The specimen was then introduced into the circuit and C_m again adjusted to give resonance. If C_1 and Q_1 are the values of capacitance and Q of the meter alone and C_2 and Q_2 are the corresponding values with the specimen in place, the equivalent series resistance, R_s, and Q are obtained from the equations

$$Q = \frac{Q_1 Q_2 (C_1 - C_2)}{C_1 Q_1 - C_2 Q_2} \tag{2.13}$$

$$R_s = \frac{(C_1/C_2)\, Q_1 - Q_2}{\omega C_1 Q_1 Q_2} \tag{2.14}$$

The equivalent series reactance X_s is then obtained from equation 2.11.

As large as possible a value of C_1 - C_2 is necessary to produce optimum operation of the Q-meter in order to obtain an accurate value of Q. As a result, measurements of Q became inaccurate at low frequencies because the values of (C_1 - C_2) were generally small, especially with the conducting specimens (R < 100) often encountered.

2.5.3 Grain Boundary Equivalent Circuit.

Basu and Maiti [13] modelled the grain bulk and boundary as each being a parallel combination of resistance and capacitance, forming a two-layer equivalent circuit, as shown in fig. 2.9, with parameters C_{bulk}, R_{bulk}, C_{gb} and R_{gb} respectively. Since the grain bulk is conductive it may be assumed to have negligible capacitance, and C_{bulk} may be ignored. The equivalent circuit impedance Z is then given by

$$Z = R_{bulk} + \frac{R_{gb}}{1 + j\omega C_{gb} R_{gb}} \tag{2.15}$$

Multiplication of the second term in (2.15) by the complex conjugate gives :

$$Z = R_{bulk} + \frac{R_{gb}}{1 + \omega^2 C_{gb}^2 R_{gb}^2} - j \frac{\omega C_{gb} R_{gb}}{1 + \omega^2 C_{gb}^2 R_{gb}^2} \tag{2.16}$$

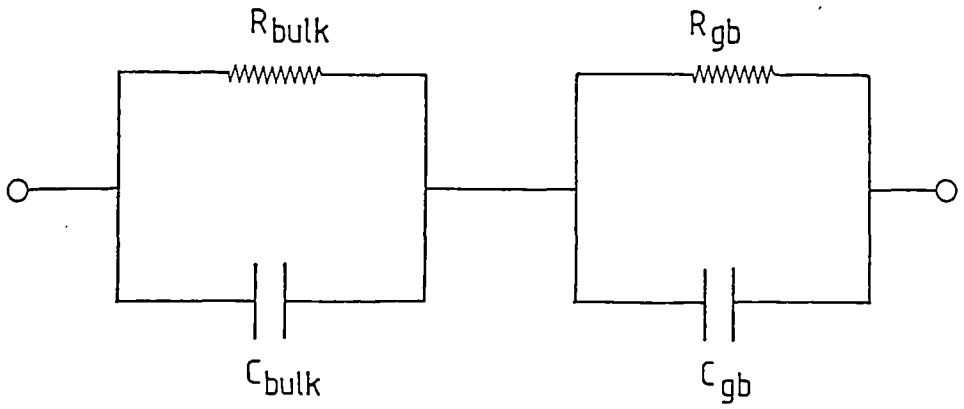

Figure 2.9 Equivalent circuit for the grain bulk and grain boundary.

It is apparent from the impedance measurement theory that the real and imaginary parts of Z are respectively equivalent to R_s and X_s. Therefore,

$$R_s = R_{bulk} + \frac{R_{gb}}{1 + \omega^2 C_{gb}^2 R_{gb}^2} \tag{2.17}$$

and

$$|X_s| = \frac{\omega C_{gb} R_{gb}}{1 + \omega^2 C_{gb}^2 R_{gb}^2} \tag{2.18}$$

The values of R_s and X_s are affected as frequency changes. At low frequency, $\omega \rightarrow 0$ so $R_s \rightarrow R_{bulk} + R_{gb}$ and $X_s \rightarrow 0$. On the other hand, at very high frequency, $\omega \rightarrow \infty$ so $R_s \rightarrow R_{bulk}$ and again $X_s \rightarrow 0$. If X_s is plotted against R_s, the values of R_{bulk} and R_{gb} can be determined from the intercepts on the real axis, at high and low frequency respectively.

2.6 Summary

This chapter has presented a description of the experimental techniques used for the preparation, and the electrical and structural characterisation of n-doped $BaTiO_3$ PTC ceramics which form the subject of this investigation.

Ceramic specimens were prepared from powder precursor materials by liquid phase sintering under closely regulated conditions of temperature and ambient atmosphere in order to control the electrical properties of the resulting ceramics. The ceramic specimens were investigated by scanning electron microscopy in secondary emission and energy dispersive X-ray analysis modes to study their microstructure and composition, and in electron barrier voltaic effect mode for carrier lifetime investigations at the grain boundaries. Optical polarized light microscopy was used to study the properties of the ferroelectric domains and their interaction with grain boundaries below and above the Curie temperature. Measurements of resistivity as a function of temperature were carried out to characterise the PTCR effect, and resistivity was also measured as a function of applied electric field at room temperature to investigate non-ohmic characteristics of the

material. The dielectric properties of the ceramics were studied by means of A.C. impedance measurements at room temperature, enabling grain boundary and grain bulk components of the resistivity to be distinguished.

These experimental techniques were utilised to investigate systematically the dependence of the PTC effect on ceramic composition, microstructure and processing history in order to study aspects of the Heywang and Daniels theory of the PTC effect.

References

1. Ichinose, N., 'Introduction to Fine Ceramics', (John Wiley and Sons, New York, 1987), p16.
2. Moulson, A. J. and Herbert, J. M., 'Electroceramics', (Chapman and Hall, London, 1990), p88.
3. Daniels, J., Härdtl, K. H. and Wernicke, R., Philips Tech. Rev., 38 [3], 73 (1978/9).
4. Al-Allak, H. M., Russell, G. J. and Woods, J., J. Phys. D : Appl. Phys., 20, 1645 (1987).
5. Al-Allak, H. M., Brinkman, A. W., Russell, G. J., Roberts, A. W. and Woods, J., J. Phys. D : Appl. Phys., 21, 1226 (1988).
6. Cheng, H. F., J. Appl. Phys., 66, 1382 (1989).
7. Al-Allak, H. M., Brinkman, A. W., Russell, G. J. and Woods, J., J. Appl. Phys., 63, 4350 (1988).

8. Kingery, W. D., 'Introduction to Ceramics' (John Wiley and Sons, New York, 1963), p369-380, 386-389.

9. Quantitative Scanning Electron Microscopy, Eds. Holt, D. B., Muir, M. D., Grant, P. R., Boswarva, I. M. (Academic Press, London, 1974), p94.

10. Ibid, p403.

11. Ibid, p213.

12. Ralph, J. E., Gowers, J. P., and Burgess, M. R., Appl. Phys. Lett. 41, 343 (1982).

13. Basu, R. N. and Maiti, H. S., Mater. Lett., 5, 99 (1987).

14. American Standards for Testing Materials DISO (1987), 'Imaging capacitance for electrodes without a guard ring'.

CHAPTER 3

THE EFFECTS OF DONOR DOPANT CONCENTRATION

3.1 Introduction

As discussed in Chapter 1 the PTCR effect was originally attributed to potential barriers at the grain boundaries arising from two-dimensional layers of occupied surface acceptor states [1], e.g. segregated acceptor ions [2,3] or adsorbed oxygen ions [4]. Daniels et al. [5] modified this model, postulating that the acceptor states consist of Ba vacancies in a thin (1-3 μm thick) [6] three-dimensional layer that has diffused inwards from the grain boundary during cooling after the sintering process. Complete electrical compensation of the donors is assumed to occur within this layer, giving rise, in effect, to a n-i-n structure at the grain boundaries.

It is well known that the room temperature resistivity decreases initially with increasing donor dopant concentration and then increases again rapidly as the donor dopant concentration is increased above about 0.4 at. %, resulting in an insulating ceramic (Wernicke, 1978 [7]; Murukami et al., 1973 [8]; Kahn, 1971 [9]; Jonker, 1964 [10]; Eror and Smyth, 1970 [11]; Heywang, 1964 [12], 1971 [3]; Sauer and Fisher, 1960 [13]; Tennery and Cook, 1961 [14]; Basu and Maiti, 1986(a) [15]), although the cause of this behaviour has not yet been completely explained.

This increase in room temperature resistivity was observed to coincide with a sharp reduction in mean grain diameter (from several micrometres to one micrometre or less) and with a colour change from dark blue in the case of semiconducting ceramics to pale blue in the

case of insulating ceramics. The increase in room temperature resistivity has been observed irrespective of the donor dopant used.

The formation of insulating layers at the grain boundaries has been suggested by some authors as an explanation for this effect. Bauer and Fisher [13] and Tennery and Cook [14] proposed that such an insulating layer might be caused by the segregation of the donor ions at the grain boundaries. However, Basu and Maiti [15] failed to observe donor segregation and suggested instead that the insulating layer consisted of a Ti-rich intergranular phase although this hypothesis is now considered to be unlikely for the following reasons. Firstly, the donor dopant atoms are known to have solubility limits which are much higher than the critical value of 0.4 at. % [16,17] in the $BaTiO_3$ crystal lattice, so that segregation at the grain boundaries is unlikely to occur at such low dopant concentrations. Secondly, heavily donor-doped specimens were observed to show normal ferroelectric hysteresis [17], which would be inconsistent with the presence of completely insulating layers at the grain boundaries.

Alternative theories explaining the increase in resistivity in terms of electrical compensation of the donors have also been advanced. Jonker [10] postulated that the donor ions are compensated at low donor concentrations, by conduction band electrons, but that a transition to vacancy compensation occurs at higher donor concentrations so that the ceramic exhibits a more insulating behaviour; no attempt was made to explain the mechanism responsible for this

transition. A partial explanation for the transition from electronic to vacancy compensation may, however, be obtained from the work of Drofenik [18] who postulated that the incorporation of donor ions into the lattice during sintering (by a reaction resulting in electronic compensation and the evolution of gaseous oxygen) is impossible if the reduction in the surface free energy during grain growth (the driving force of the sintering process) is balanced by the increase in free energy associated with the expulsion of oxygen. This condition is influenced by the ambient oxygen partial pressure during sintering. When sintering in air, this condition is satisfied above a certain dopant concentration, resulting in the suppression of donor incorporation with electronic compensation, together with the halting of grain growth.

Other workers have advanced explanations of the effect in terms of self-compensation of the donors; this entailed the assumption that the donors are incorporated with different oxidation states at equivalent-lattice sites [3] or with the same oxidation state at different lattice sites [8]. Such self-compensation mechanisms are not, however, universally applicable to all donors, e.g. lanthanum which has a single oxidation state (3+), and an ionic radius similar to that of the Ba^{2+} ion and which is too large to permit incorporation at Ti sites. Lanthanum is thus most probably incorporated only as La^{3+} at Ba sites, but the transition to an insulating ceramic is nevertheless observed as the dopant concentration exceeds 0.4 at. % La.

However, Daniels et al [5] proposed that the increase in resistivity is caused by the combined effects of the decrease in grain size with increasing donor concentration and the formation of an insulating grain boundary layer rich in Ba vacancies. This theory postulates that at high donor concentration the grain size is reduced to about 2 μm. This value is assumed to be comparable to the width of the Ba-vacancy rich insulating layer, so that the entire thickness of each grain, and therefore the entire material, is rendered a complete insulator.

This chapter presents the results of a study of the effects of donor doping on the resistivity of $BaTiO_3$ ceramics. Holmium was used as the donor dopant, at concentrations in the range of 0.05 to 0.8 at. %. The transition from conductive to insulating behaviour at room temperature for high dopant concentrations (> 0.4 at %) has been investigated. Resistivity and dielectric measurements have been made and have revealed that the transition is exclusively a grain boundary phenomenon for which existing models fail to offer a satisfactory explanation. The results of these measurements are analysed in terms of a numerical model of the grain boundary potential barriers, and a new explanation for the conductive to insulating transition is proposed.

3.2 Experimental Method

3.2.1 Specimen Preparation

Barium titanate ceramic PTCR specimens containing different Ho (donor) concentrations varying between 0.05 and 0.8 at. % were prepared with the formulation $Ba_{1-x}Ho_xTiO_3$. The precursor material used was commercial $BaTiO_3$ (Mandoval grade 6) with holmium, in the form of Ho_2O_3, used as the donor dopant. Sufficient TiO_2 was added to give a 0.5 at. % excess of Ti over the stoichiometric quantity, in order to ensure liquid phase sintering and controlled grain growth; a small amount (0.9 mol. %) of SiO_2 was added to serve as a sintering aid. Specimens were prepared using the technique described earlier in section 2.1.1. The specimens were then sintered in a tube furnace according to the firing profile in fig. 3.1 which entailed sintering for 1 hour at 1420°C followed by annealing for 30 minutes at 1220°C. Air was passed through the tube at a flow rate of $1\ell\ min^{-1}$ throughout the firing in order to maintain a constant ambient atmosphere.

3.2.2 Electrical Measurements

The flat surfaces of specimens were smoothed, cleaned in acetone, and coated with InGa alloy contacts. The resistivity-temperature characteristics of the ceramics were then determined by the two-probe DC measurement technique described earlier (Section 2.4.1).

The dielectric properties of selected specimens which had been reduced to a thickness of ~0.7 mm were measured at room temperature in the radio-frequency (RF) and audio-frequency (AF) ranges using a

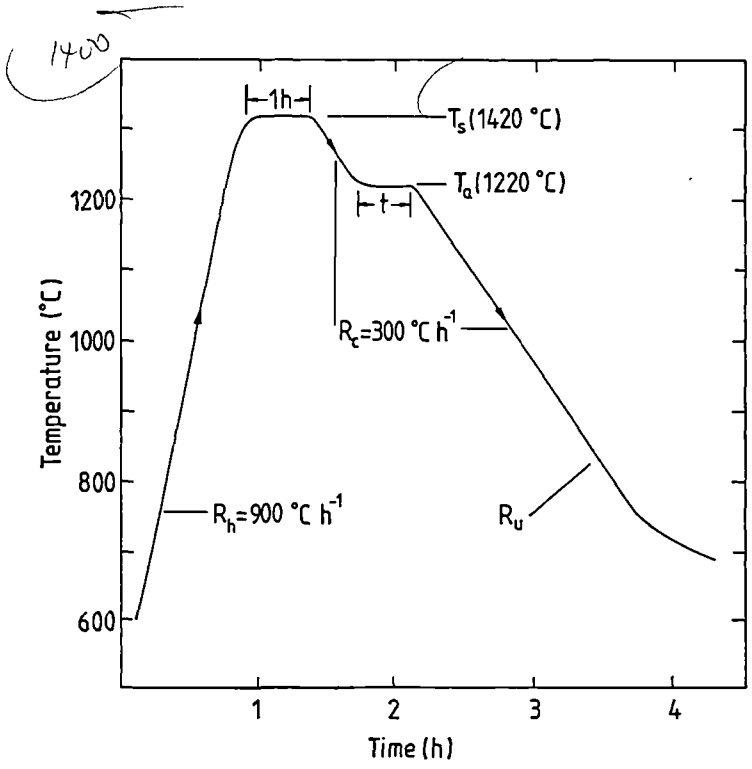

Figure 3.1 Sintering profile used for specimen preparation.

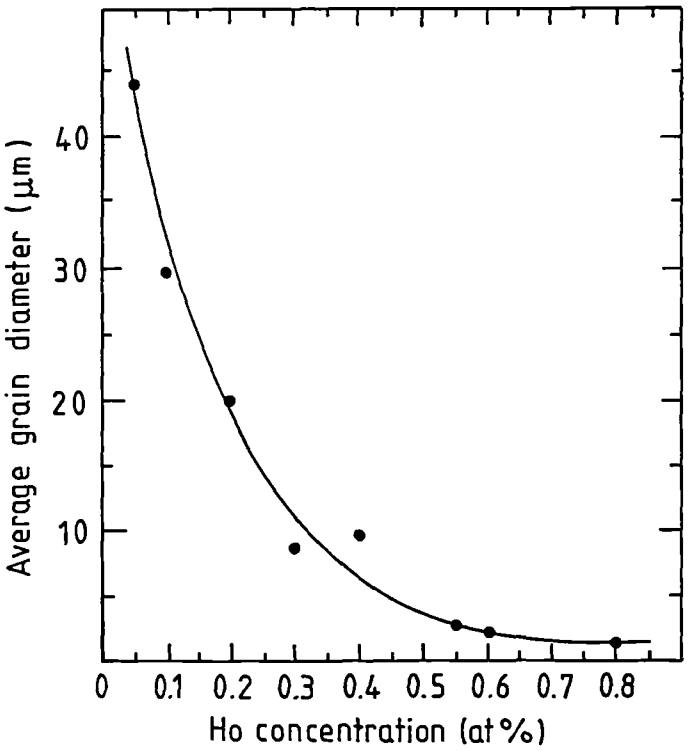

Figure 3.2 Mean grain diameter as a function of dopant concentration.

Hewlett Packard 4342A Q-meter and a Marconi Instruments TF1313A AC bridge respectively as described earlier (Section 2.5). Electric field fringing effects at the specimen edges were negligible as sources of error because the samples used were thin discs of area 0.152 cm^2 and thickness ~0.07 cm. Self-heating due to internal dissipation effects was likewise not a significant source of error because of the small amplitude (750 mV) of the AC test signal.

The voltage dependence of resistivity at room temperature was investigated using the pulsed voltage technique described earlier in Section 2.4.2.

3.3 Results

3.3.1 Sintering Behaviour

Ceramic specimens incorporating up to 0.4 at. % Ho were observed to be dark blue-green after sintering, whereas those containing higher levels of donor dopant concentration were a pale green-grey colour. The influence of donor dopant concentration on the microstructure of the ceramics was investigated by means of a scanning electron microscope (SEM). The mean grain diameter was determined from SEM micrographs of as-fired surfaces and is presented as a function of donor dopant concentration in fig. 3.2. It is apparent that an increase in donor dopant concentration from 0.05 to 0.6 at. % Ho results in a reduction in mean grain diameter from 44 μm to 2 μm, i.e. by more than one order of magnitude. Further increases in dopant

concentration, however, had little influence on the mean grain diameter. The effect of progressive increase in donor dopant concentration on ceramic microstructure is illustrated in figs. 3.3 and 3.4, corresponding to 0.05 and 0.6 at. % Ho respectively. Ceramic specimens incorporating low concentrations of donor dopant had flat grains with considerable quantities of second phase (generally visible as fibrous or irregular features near grain boundaries) and also displayed pronounced growth terracing (fig. 3.3). As the donor dopant concentration was increased both the amount of second phase and the degree of growth terracing became progressively less apparent, until they were virtually absent in the most heavily doped ceramics (fig. 3.4). In more heavily doped ceramics, represented in fig. 3.4 for 0.6 at. % Ho, the grains were observed to be more rounded and to have a narrow distribution of sizes (mean grain diameter ~ 2 μm with a few larger grains present which did not exceed ~ 4 μm in size). Analysis of the second phase in lightly doped specimens by means of the EDX (energy dispersive analysis of X-rays) analyser attached to the SEM revealed that this phase was rich in Si and to a lesser extent Ti relative to the bulk of the grain (see fig. 3.5). This was believed to arise from the addition of SiO_2, which acted as a sintering aid, and of a small (0.5 mol. %) excess of TiO_2 in order to control the titanate stoichiometry, to the original ceramic composition. Since both SiO_2 and TiO_2 were insoluble in the $BaTiO_3$ lattice, they were eliminated into a distinct second phase as grain growth occurred during sintering.

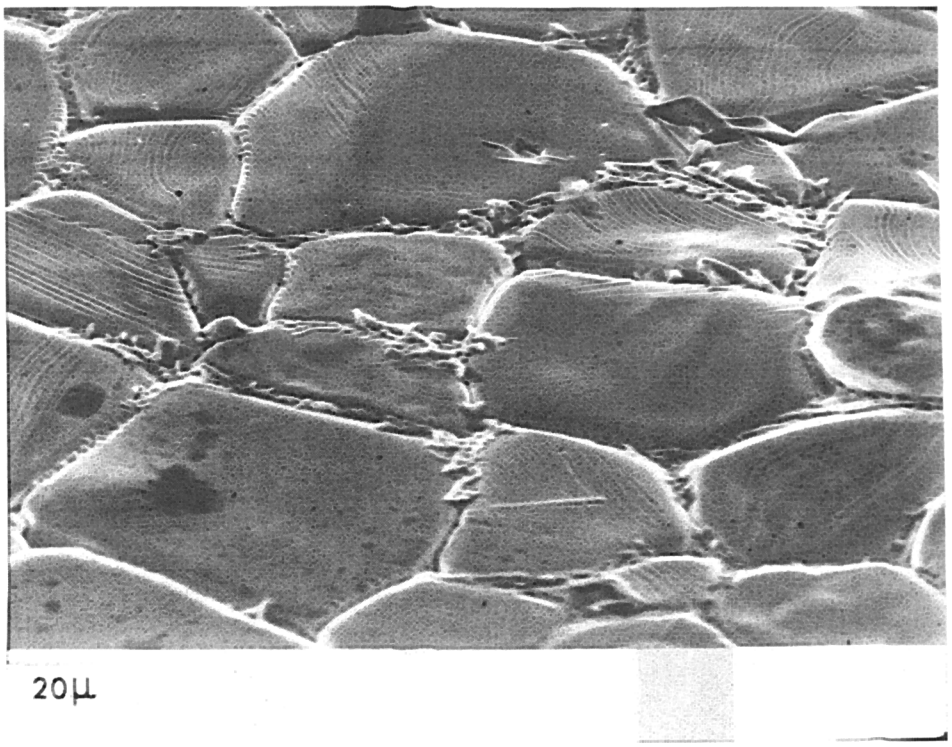

Figure 3.3 SEM micrograph of as-fired surface of specimen doped with 0.05 at. % Ho.

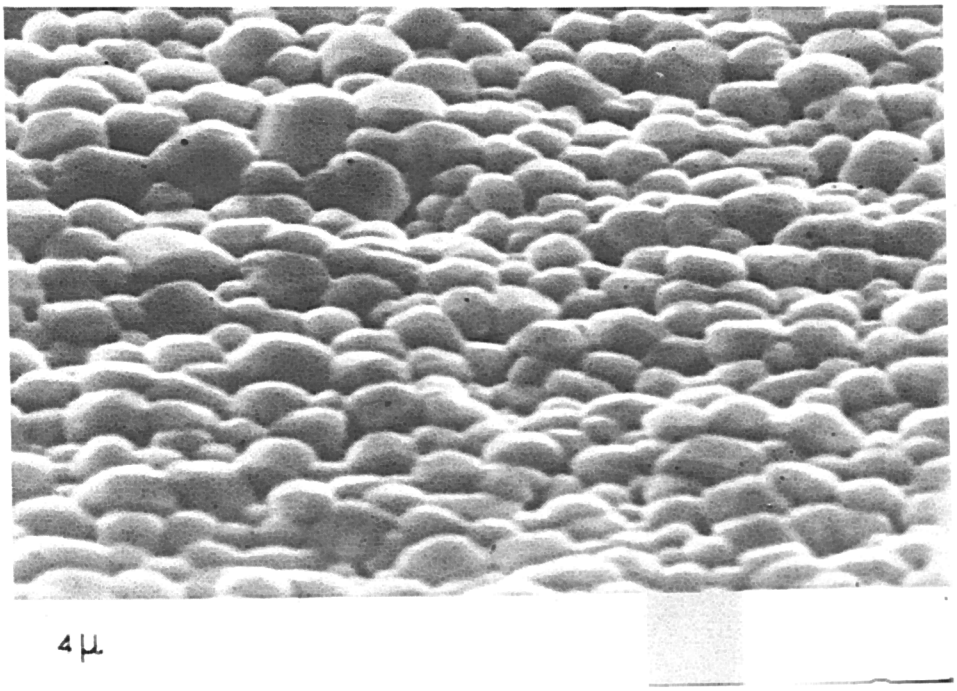

Figure 3.4 SEM micrograph of as-fired surface of specimen doped with 0.6 at. % Ho.

3.3.2 The Temperature Dependence of Resistivity

The values of resistivity (ρ (Ω cm)) of the ceramic samples were measured as a function of temperature (T); additionally these values were normalised with respect to their value per grain boundary (See Apendix A1 - normalised values are denoted by the use of a prime, i.e. ρ') in order to eliminate the effect of the reduction in grain size with increasing donor dopant concentration and thus permit comparison between specimens of differing composition. A series of measured resistivity versus temperature plots (ρ - T) for the specimens incorporating different donor dopant concentrations is shown in fig. 3.6. Each experimental point represents the mean value of measurements from 5 nominally identical samples (the mean variation between specimens of the same composition was ~ 6%). The corresponding series of plots of normalised resistance versus temperature (ρ' - T) plots is reproduced in fig. 3.7. Fig. 3.8 reveals that the donor dopant concentration strongly influences the maximum value of both the resistivity ρ_{max} and the normalised resistance, ρ'_{max}, and the temperature, T_{max}, at which ρ_{max} and ρ'_{max} occur. Initially ρ'_{max} was observed to fall rapidly with increasing donor dopant concentration up to ~ 0.3 at. % Ho, followed thereafter by a much slower decrease (fig. 3.8). However, the value of T_{max} was observed to show an initial increase followed by a sharp reduction as the donor concentration exceeded ~ 0.4 at. % (fig. 3.9).

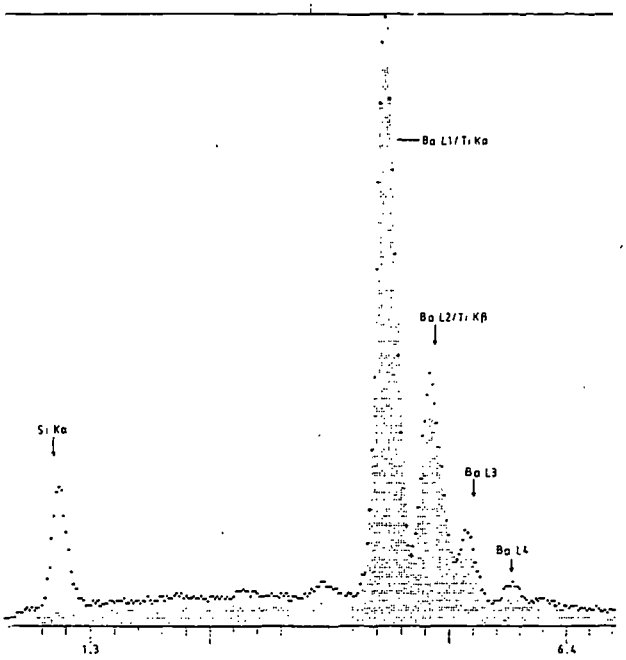

Figure 3.5 EDX spectrum for a specimen containing 0.05 at. % Ho recorded from the mid grain (shaded area) and the second phase (dotted curve).

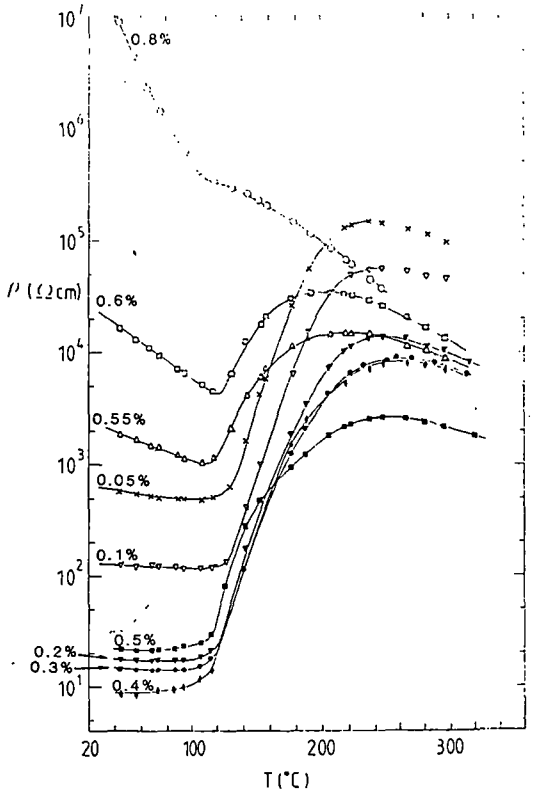

Figure 3.6 Resistivity ρ as a function of temperature T for different dopant concentrations.

The influence of the donor concentration on the normalised low-temperature resistance, ρ'_{45} (measured at 45°C), derived from the data presented in fig. 3.8, is illustrated in fig. 3.10. The behaviour of the measured low-temperature resistivity (i.e. not normalised to the value per grain boundary), ρ_{45}, is also given in fig. 3.10 for purposes of comparison. It is evident that both ρ'_{45} and ρ_{45} decrease by about two orders of magnitude when the donor concentration is increased from ~0.05 at. % to ~0.3 at. % Ho, but then rise sharply as the donor concentration is further increased. It is interesting to note that the functional dependence of both ρ'_{45} and ρ_{45} on the donor concentration is very similar. The various parameters derived from the ρ-T plots for different donor concentrations are summarized for reference purposes in Table 3.1.

3.3.3 Dielectric Measurements

Dielectric investigations were carried out on specimens doped with 0.05, 0.1, 0.55 and 0.6 at. % Ho, the resistivities of which lay either side of the minimum of the low-temperature resistivity versus donor dopant concentration curve (fig. 3.11 and 3.12). [Specimens of composition 0.2, 0.3 and 0.4 at. % Ho, whose resistivities lay near the minimum of the curve, were not investigated since their resistances were found to be too low to permit the balancing of the capacitance bridge and Q-meter]. The real (R_s) and imaginary (X_s) parts of the impedance were determined at each frequency and plotted in the form of complex impedance diagrams, to permit the resistance of the grain

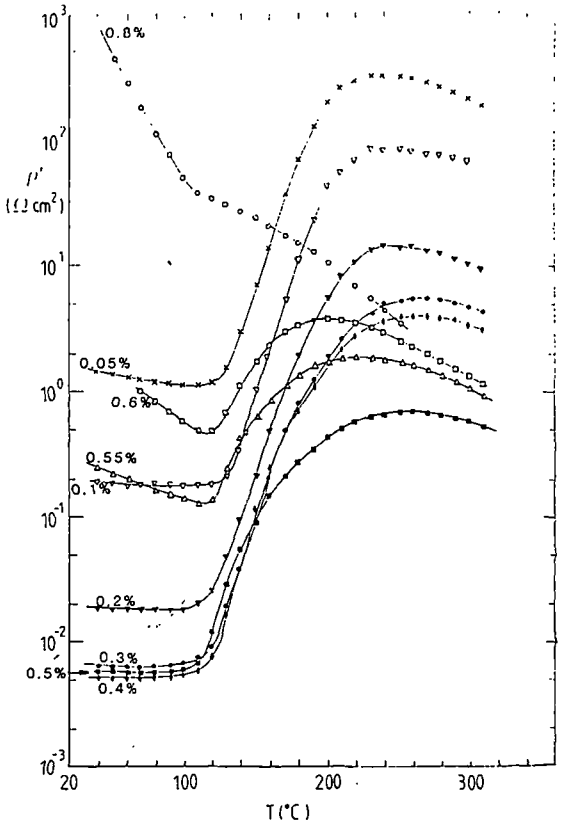

Figure 3.7 Normalised resistance, ρ' as a function of temperature T for different dopant concentrations.

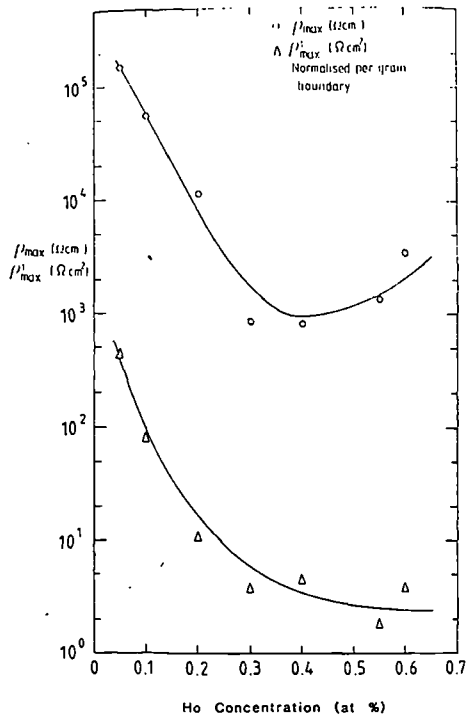

Figure 3.8 ρ_{max} and ρ'_{max} as a function of dopant concentration.

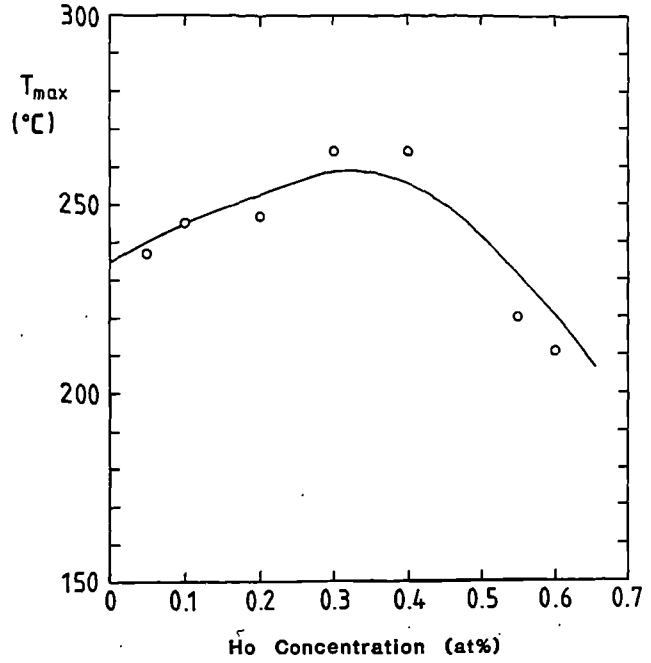

Figure 3.9 T_{max} as a function of dopant concentration.

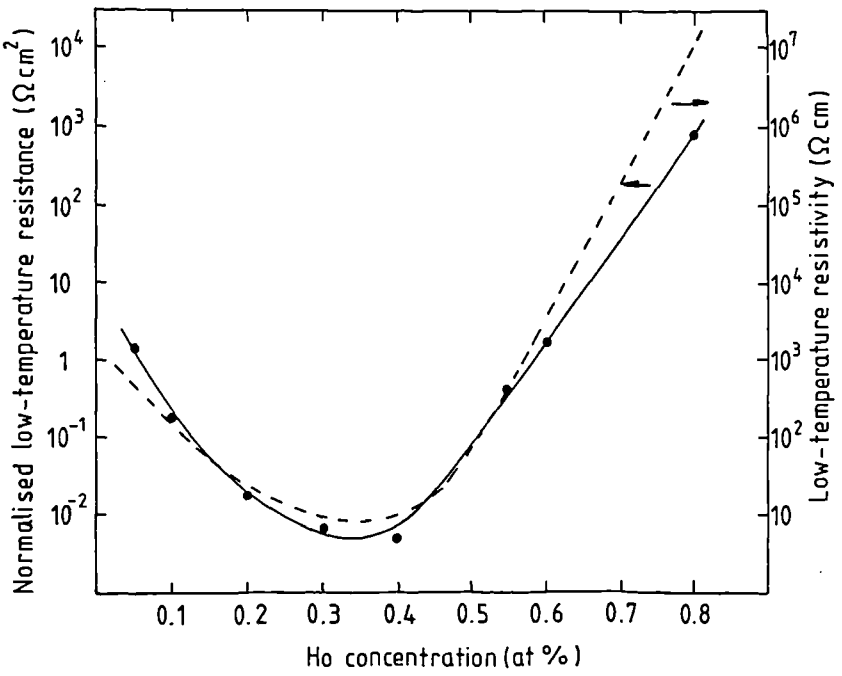

Figure 3.10 Dependence of the resistivity ρ_{45} and normalised resistance ρ'_{45}, measured at 45°C, on the dopant concentration.

Table 3.1

at. % Ho	0.05	0.1	0.2	0.3	0.4	0.5	0.55	0.6	0.8
Mean grain diam. (μm)	44 ± 4	30 ± 3	20 ± 2	9 ± 1	10 ± 1	5.25 ± 0.5	2.55 ± 0.2	2 ± 0.2	1.7 ± 0.2
T_{max} (°C) (K)	237 510	245 518	247 520	264 537	264 537		220 493	211 484	
ρ_{max}	1.5×10^{5}	5.5×10^{4}	1.14×10^{4}	8.6×10^{3}	8.1×10^{3}		1.35×10^{4}	3.4×10^{4}	
ρ'_{max} (per grain boundary)	4.35×10^{2}	8.1×10^{1}	1.09×10^{1}	3.8×10^{0}	4.5×10^{0}		1.8×10^{0}	3.8×10^{0}	
ρ_{45} (45°C)	5.35×10^{2}	1.25×10^{2}	1.8×10^{1}	1.5×10^{1}	9×10^{0}		2.15×10^{3}	1.7×10^{4}	8×10^{6}
ρ'_{45} (per grain boundary)	1.46×10^{0}	1.9×10^{-1}	1.9×10^{-2}	6.5×10^{-3}	5.2×10^{-3}	2.85×10^{-2}	2.8×10^{-1}	1.6×10^{0}	8.5×10^{2}
ρ_{min}	4.7×10^{2}	1.13×10^{2}	1.7×10^{1}	1.4×10^{1}	9×10^{0}		1.02×10^{3}	4.3×10^{3}	
ρ_{max}/ρ_{min}	319	487	671	614	900		13.23	7.907	

bulk, R_{bulk}, to be distinguished from that of the grain boundary layer, R_{gb}. The analysis (see Section 2.5) is based on a combination of lumped parallel R-C equivalent circuits, representing conduction processes in the grain bulk, grain boundaries and contacts etc. [19]. The usual approximation, which was adopted here, assumes the contact impedance to be negligible and the grain bulk to have no capacitance. The equivalent circuit then reduces to a parallel combination of R_{gb} and C_{gb} (representing the impedance of grain boundaries) in series with a purely resistive term R_{bulk} (representing the grain bulk impedance). The real and imaginary part of the combined impedance are given by

$$R_s = R_{bulk} + \frac{R_{gb}}{1 + (\omega C_{gb} R_{gb})^2} \tag{3.1}$$

$$X_s = j \frac{\omega C_{gb} R_{gb}^2}{1 + (\omega C_{gb} R_{gb})^2} \tag{3.2}$$

where ω is the angular frequency. It is immediately apparent that the imaginary part disappears at DC and high frequency so that the corresponding intercepts on the real axis equal $(R_{gb} + R_{bulk})$ and R_{bulk} respectively.

The impedance diagrams for the low donor dopant concentration samples (0.05 and 0.1 at. % Ho) are shown in fig. 3.11; they indicate that the low temperature resistance of the ceramic arises mainly at the grain

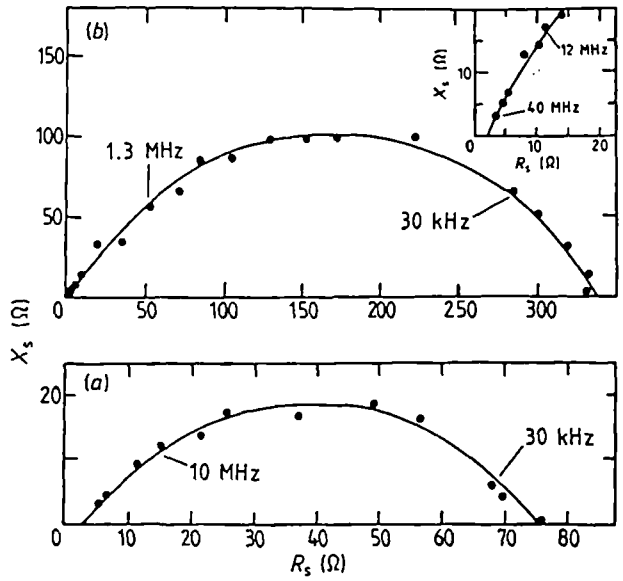

Figure 3.11 Complex-plane impedance diagrams for lightly doped specimens (a) 0.05 at. % Ho and (b) 0.1 at. % Ho.

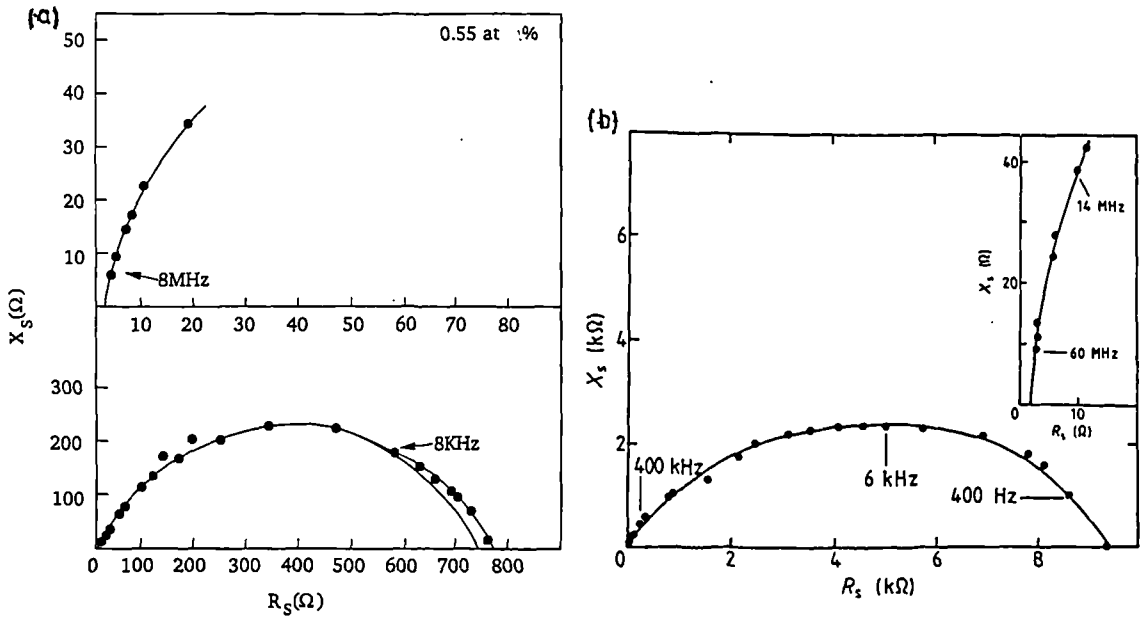

Figure 3.12 Complex-plane impedance diagrams for heavily doped specimens (a) 0.55 at. % Ho and (b) 0.6 at. % Ho.

boundary region, since the grain bulk resistance was found to be similar, ~ 2Ω, in each case. In these investigations the measurement errors tend to be greater at low frequency, where the instrument is more difficult to balance. In this case, the resultant uncertainty was ~ 5% at low frequencies and somewhat less than this at higher frequencies. The single semi-circle obtained in the complex impedance diagram confirms that the contact impedance was negligible; had this not been the case, a second semi-circle arising out of the contact impedance would have been visible on the diagram. The impedance diagrams for specimens incorporating 0.55 and 0.6 at. % Ho are given in fig. 3.12. It can again be seen that the increase in low temperature resistivity at these high dopant levels results from an increase in the grain boundary resistance, since the bulk resistance has remained virtually unchanged at ~2 Ω in both cases. The shape of the complex impedance plots indicates that contact impedances were insignificant, as in the case of the lightly doped specimens. No investigations were carried out on specimens containing dopant concentrations higher than 0.6 at. % because it proved difficult to balance the A.C. bridge at these concentrations.

3.3.4 Resistivity-Voltage Dependence

The variation of room-temperature resistivity with the applied voltage was investigated for both lightly-doped (0.05 and 0.1 at. % Ho) and heavily-doped (0.6 % Ho) ceramic specimens (i.e. on either side of the minimum of the low-temperature resistivity versus donor dopant

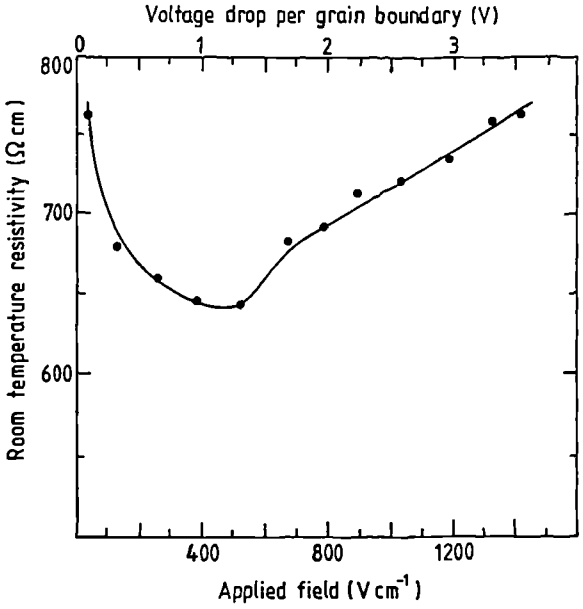

Figure 3.13 Dependence of room temperature resistivity on the applied field for 0.05 at. % Ho concentration.

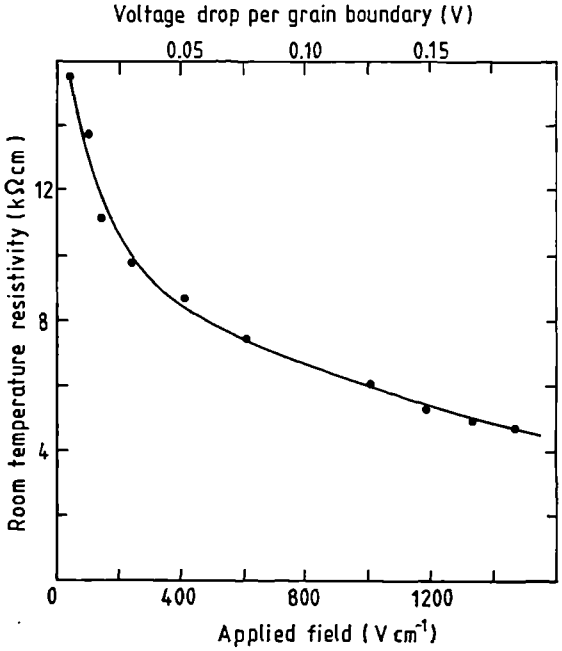

Figure 3.14 Dependence of room temperature resistivity on the applied field for 0.6 at. % Ho concentration.

concentration characteristic). The results for the lightly and heavily-doped specimens are reproduced in figs. 3.13 and 3.14. It is seen that the room temperature resistivity of the lightly doped specimen (fig. 3.13) fell initially with increasing applied field but then started to increase again as the field exceeded about 500 V cm^{-1}. In contrast, however, a monotonic decrease in resistivity with increasing applied field was observed for the heavily-doped ceramics (fig. 3.14).

3.3.5 Activation Energy Analysis

Arrhenius plots of the natural logarithm of resistivity ρ as a function of T^{-1} at temperatures below the transition temperature for lightly donor doped (0.05 and 0.55 at. % Ho) and heavily donor doped (0.6 and 0.8 at. % Ho) ceramic specimens are reproduced in figs. 3.15 to 3.18. The Heywang theory (see Section 1.4) postulates that the resistivity is given by

$$\rho = \rho_{\infty} \exp\left(\frac{e\phi}{kT}\right) \tag{3.3}$$

$$\phi = \frac{e}{2\varepsilon_r\varepsilon_o}\frac{N_{A0}^2}{N_D} \tag{3.4}$$

where e is the electronic charge, N_D the donor dopant concentration, N_{A0} is the density of acceptor states at the grain boundary, ε_r is the relative permittivity and ε_o the permittivity of free space.

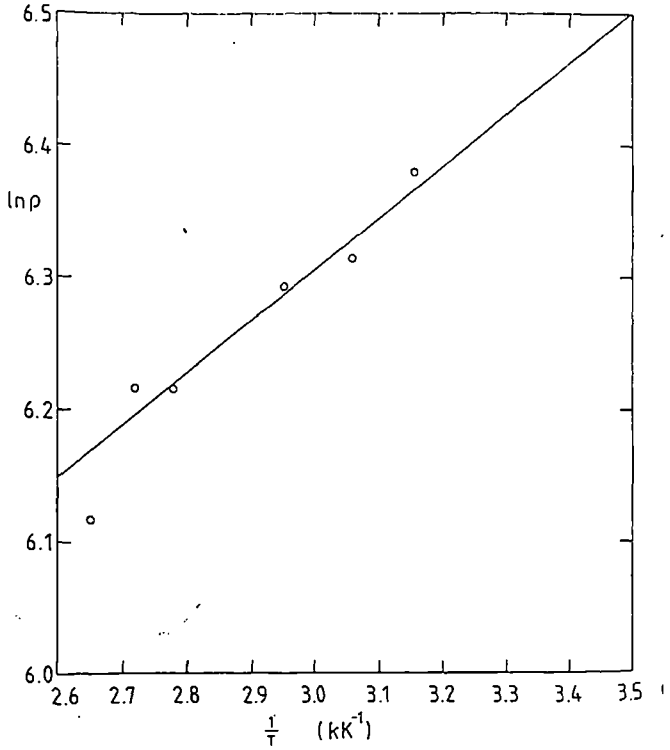

Figure 3.15 Arrhenius plot (temperature < T_o) for 0.05 at. % Ho concentration.

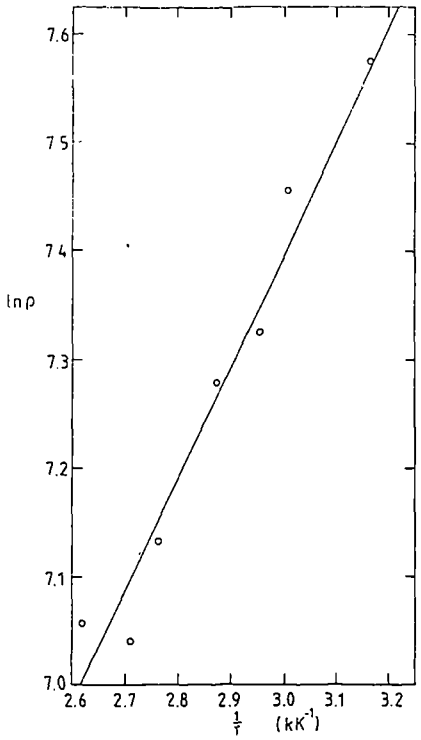

Figure 3.16 Arrhenius plot (temperature < T_o) for 0.55 at. % Ho concentration.

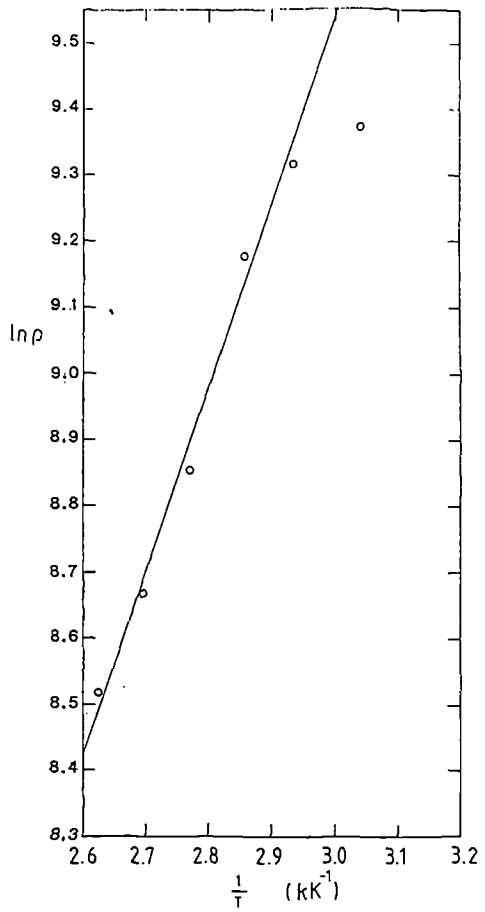

Figure 3.17 Arrhenius plot (temperature < T_o) for 0.6 at. % Ho concentration.

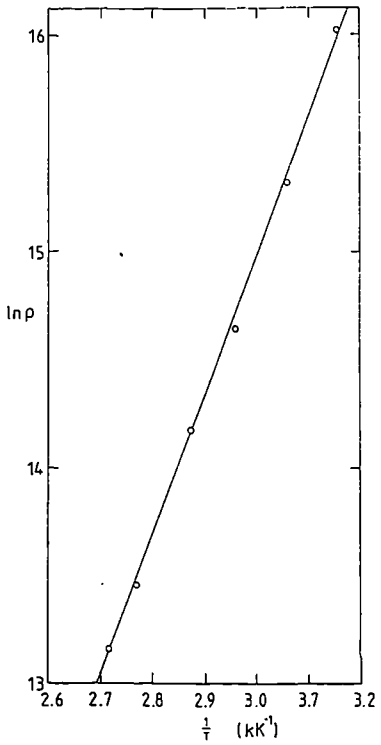

Figure 3.18 Arrhenius plot (temperature < T_o) for 0.8 at. % Ho concentration.

Taking logarithms of both sides of (3.4) we have

$$\ell n\,(\rho) = \frac{e\phi}{k} \cdot \frac{1}{T} + \text{constant} \qquad (3.5)$$

so that an Arrhenius plot of $\ell n\,(\rho)$ versus T^{-1} should yield a straight line of gradient $\frac{e\phi}{k}$ at constant N_{A0} if the Heywang model is followed.

Hence the height $e\phi$ of the potential barriers at the grain boundaries postulated by Heywang may be determined.

The straight lines obtained in the Arrhenius plots of figs. 3.15 to 3.18 indicate the existence of potential barriers within the ceramic specimens; the height of these potential barriers are given in table 3.2. It is evident that the transition from low to high values of low temperature resistivity as the donor dopant concentration was increased corresponded to a very substantial increase in potential barrier height. It is particularly noteworthy that the transition from a residual PTCR behaviour in the case of 0.6 at. % Ho doped ceramics to a totally resistive behaviour in 0.8 at. % Ho ceramics (figs. 3.17, 3.18) was accompanied by a doubling of potential barrier height from 0.27 eV to 0.56 eV. It was not possible to derive useful Arrhenius plots for the 0.1 to 0.4 at. % Ho doped ceramics, since the room temperature resistance of the specimens of these compositions was too low for the measuring apparatus, so that apparatus-induced errors became significant, and

introduced a considerable degree of scatter in the data points. This could not be compensated by increasing the range of temperatures used for measurement since the apparatus was incapable of cooling specimens below ambient. Values at specimen temperatures near the transition temperature were unusable since ε_r was rapidly varying according to the Curie-Weiss law in this temperature regime. [The Arrhenius derivation - see equation 3.4, 3.5 - assumes constant ε_r and would be invalid near T_C]. The derivation of Arrhenius plots at temperatures above T_{max} was not feasible because of limitations on the maximum temperature achievable by the equipment; this prevented the making of measurements at temperatures high enough to avoid the dominance of the variation of ε_r with temperature in the vicinity of the PTCR transition.

Table 3.2

at. % Ho	0.05	0.55	0.6	0.8
Activation Energy (eV)	0.0335	0.0892	0.267	0.555

3.3.6 ρ_{max}-T_{max} Analysis : The Ihrig-Puschert Model

The effect of donor dopant concentration on the PTCR characteristic was further investigated by the construction of ρ_{max} vs. T_{max} diagrams, first described by Jonker [4]. Values of ρ_{max} and T_{max} were calculated using the Heywang equations for a range of values of acceptor energy E_A and effective acceptor density N_{A0}, at constant

values of other relevant parameters such as the charge carrier density n and the average grain size d, by the method of Ihrig and Puschert [19] described in Appendix A2. Curves of constant E_A and N_{A0} were plotted on a graph of ρ_{max} vs. T_{max} enabling the construction of a map of (ρ_{max},T_{max}) over the range of interest of the parameters. Experimentally measured values of ρ_{max} and T_{max} for ceramic specimens of varying composition were then superimposed on the (ρ_{max},T_{max}) map, enabling estimates to be made of the values of E_A and N_{A0} and the influence of donor dopant concentration on these parameters to be investigated.

The application of this technique for the comparison of the properties of ceramic specimens of different composition was complicated by the possibility of variation of the charge carrier concentration n and grain size d with donor dopant concentration, since n and d were parameters in the calculation of the ρ_{max} vs. T_{max} plots. Dielectric measurements at room temperature of specimens incorporating 0.05, 0.1, 0.55 and 0.6 at. % Ho as a donor dopant, however, revealed a value ρ_{bulk} = 4.7 Ω cm in each case, irrespective of donor dopant content. Insertion of this value, together with electron mobility μ = 0.5 $cm^2\ V^{-1}\ s^{-1}$ into the identity $n = (\mu e \rho_{bulk})^{-1}$ yielded the value $n \approx 2.7 \times 10^{18}\ cm^{-3}$ for each composition. The same value of n was assumed to be valid in the case of 0.2, 0.3 and 0.4 at. % Ho specimens which were not subjected to dielectric investigations : this assumption seemed reasonable since ρ_{bulk} and therefore n was found to have the

same value at higher and lower donor dopant concentrations. It may be noted that this value of n was at least an order of magnitude below the value expected from the donor dopant concentration (table 3.2).

The effects of varying grain size on ρ_{max} were compensated by normalisation with respect to a specific grain diameter, as described in Appendix A2. Normalised values are denoted by ρ^*_{max}.

Plots of ρ^*_{max} vs. T_{max} were calculated for a ceramic composition containing 0.1% Ho, with d = 30 μm and n = 2.7 x 10^{18} cm^{-3} and are given in fig. 3.19. Measured values of ρ^*_{max} and T_{max} for specimens of varying composition, with ρ^*_{max} normalized with respect to d = 30 μm, were also plotted on fig. 3.20. The specimen parameters are given in table 3.3. It is seen that the 0.05 and 0.1 at. % Ho specimens lie on a curve corresponding to E_A = 1.2 eV whereas more heavily doped specimens containing 0.2, 0.3 and 0.4 at. % Ho correspond to E_A = 1.1 eV. Further increases in doping level, to 0.55 and 0.6 at. % Ho, correspond with a still lower value of E_A = 0.95 eV. Dopant level does not appear to exert a monotonic influence on the value of N_{A0} - as the dopant concentration increases from 0.05 to 0.4 at. % Ho, N_{A0} exhibits a slow decrease, but increases again as the donor dopant concentration is further increased to 0.55 and 0.6 at. % Ho.

The values of E_A obtained for moderate donor dopant concentrations of 0.2, 0.3 and 0.4 at. % Ho, E_A ~ 1.1 eV, are consistent with the value of E_A = 1.12 eV derived by other workers under similar conditions [28].

Curves of ρ_{max} vs. T_{max} at constant E_A were calculated for 0.3 and 0.55 at. % Ho specimen compositions, using the values determined above for E_A but in this case using the actual rather than the normalised grain size. This corresponded to E_A = 1.1 eV, d = 10 μm for 0.4 at. % Ho and E_A = 0.95 eV, d = 2.55 μm for 0.55 at. % Ho. The curves were then superimposed on a non-normalised plot of ρ_{max} vs. T_{max} (fig. 3.20); it is immediately apparent that the values of ρ_{max} and T_{max} for these specimens lie on the calculated curves, providing confirmation of the validity of the grain size normalisation approach adopted earlier.

3.4 Discussion

3.4.1 Sintering Properties

The reduction in grain size and change in colour of the ceramic when the donor dopant content exceeded ~ 0.4 at. % Ho is in agreement with the observations of previous workers (Sections 1.4 and 1.5). The presence of a second-phase component in readily detectable amounts (using EDX) in the lightly doped ceramics, and its apparent absence in the more heavily doped specimens, may be explained in terms of the specimen microstructure. The lightly doped samples consisted of large, flat grains which fitted closely together, and contained relatively few intergranular interstices into which the second phase might be concentrated during the sintering process. The excess second phase which could not be accommodated within these interstices was therefore ejected to the surface of the sample. The more heavily doped specimens, however, consisted of small rounded grains and contained

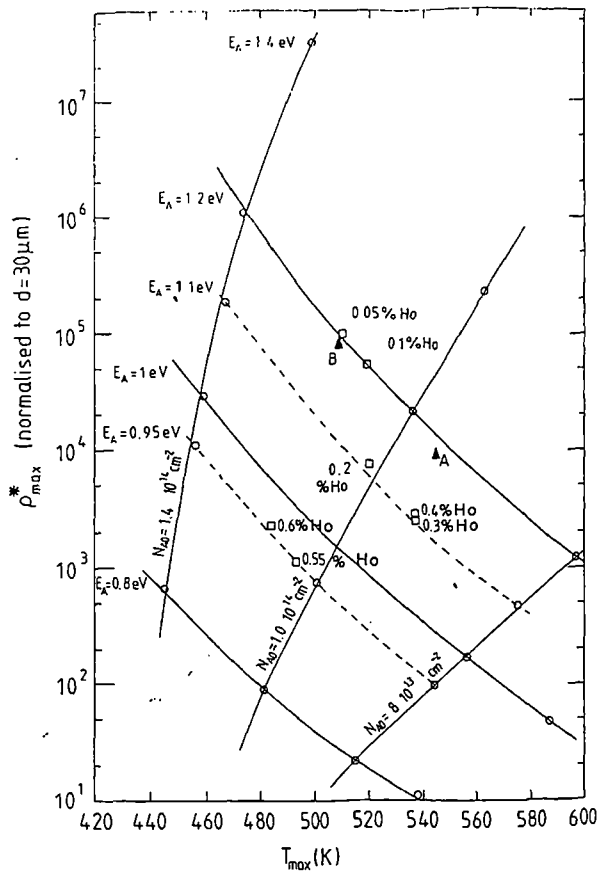

Figure 3.19 Ihrig-Puschert plot of ρ_{max} against T_{max}.

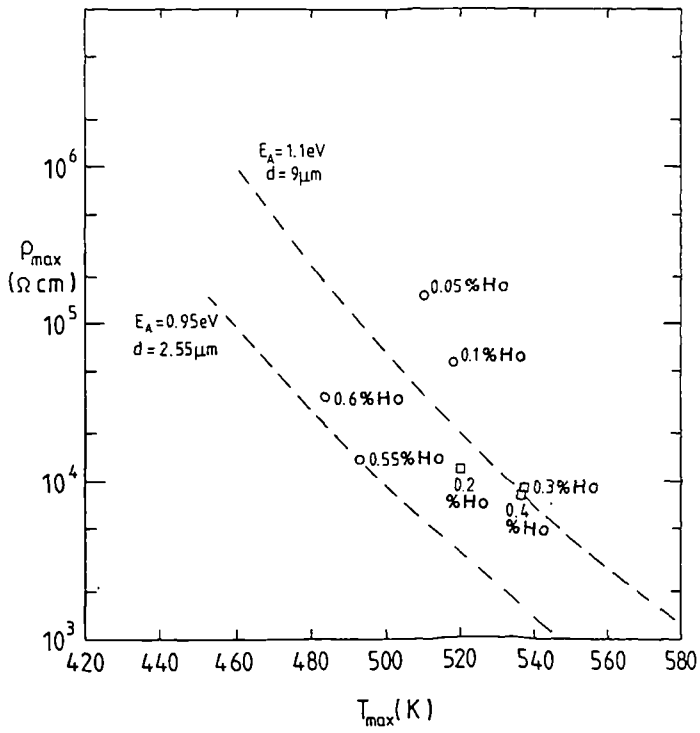

Figure 3.20 Non-normalised plot of ρ_{max} against T_{max}.

Table 3.3

at. % Ho	0.05	0.1	0.2	0.3	0.4	0.55	0.6
Grain bulk R (Ω)	2	2	2§	2§	2§	2	2
ρ_{gb} (Ω cm)	4.68	4.68	4.68§	4.68§	4.68§	4.68	4.68
n (cm^{-3})	2.67×10^{18}	2.67×10^{18}	2.67×10^{18}§	2.67×10^{18}§	2.67×10^{18}§	2.67×10^{18}	2.67×10^{15}
Mean grain diam. (μm)	44	30	20	9	10	2.55	2
Expected n′ (cm^{-3})	7.8×10^{18}	1.56×10^{19}				8.58×10^{19}	9.36×10^{19}
ρ_{max} (Ω cm)	1.5×10^{5}	5.5×10^{4}	1.14×10^{4}	8.6×10^{3}	8.1×10^{3}	1.35×10^{4}	3.4×10^{4}
ρ^{*}_{max} (Normalize dto 30 μm)	1.02×10^{5}	5.5×10^{4}	1.71×10^{3}	2.9×10^{2}	2.4×10^{3}	1.6×10^{3}	5.1×10^{3}
T_{max} (K)	510	518	520	537	537	493	484

§ Assumed Values

a much larger number of interstices into which the second phase material was readily dispersed. Thus the heavily-doped, small-grained ceramic could accommodate all the second phase material within the interstices without having to eject it onto the sample surface.

The composition of the second phase, which was found by EDX analysis to be rich in Ti and Si relative to the grain bulk, indicates its probable origin in the SiO_2 and excess TiO_2 added to the composition to promote liquid phase sintering and ensure uniform grain growth and dopant incorporation throughout the ceramic body during the sintering process. It appears that TiO_2 in excess of the stoichiometric quantity was eliminated into the second phase during grain growth; it is likely that all the SiO_2 remained in the second phase throughout the process and that no significant amounts were incorporated into the grain bulk, since Si was undetectable by EDX in the grain bulk (fig. 3.6).

3.4.2 Effect of Donor Dopant Concentration on Low Temperature Resistivity

3.4.2.1 Grain Boundary Origin of the Conducting-Insulating Transition

It is evident from the AF and RF dielectric measurements shown in figs. 3.12 and 3.13 that the greater part of the resistance at the low concentrations of 0.05 and 0.1 at. % Ho is caused by the behaviour of the grain boundaries and not, as previously assumed, by a reduction in

the charge carrier concentration resulting from the low donor dopant concentration. The similar values of grain bulk resistivity derived from dielectric measurements carried out on both lightly and heavily-doped ceramics (figs. 3.12 and 3.13) imply that the charge carrier concentration is similar in the two doping regimes and that variations in this parameter are unlikely to be responsible for changes in room temperature resistivity. The room temperature resistivity of lightly-doped samples (fig. 3.12) shows a significant dependence on applied voltage; it is therefore unrelated to the formation of passive intergranular resistive layers by the second phase. It is assumed instead that the increased low-temperature resistivity in lightly doped samples (fig. 3.12) is caused by the enhancement of the residual potential barrier which is partially compensated by the spontaneous polarization at low temperature, in accordance with Jonker's model [10].

The initial fall in the resistivity of the lightly-doped ceramics with increasing applied voltage is attributed to the diminution of the influence of the residual potential barriers at the grain boundaries in the presence of an applied field. Fowler-Nordheim tunnelling might be regarded as a possible mechanism for the diminution of grain boundary potential barriers in the presence of applied fields. According to Sze [25] the equation for current transport in insulators by Fowler-Nordheim tunnelling takes the form

$$J = C_1 E^2 \exp(-E_o / E) \qquad (3.10)$$

where J = current density ($A\ cm^{-2}$)

E = electric field ($V\ m^{-1}$)

C_1 is a constant in terms of carrier effective mass

E_o is a constant in terms of barrier height

and $\rho = E/J$ is the resistivity.

Rearranging,

$$\ell n\ (\rho E) = \frac{E_o}{E} - \ell n\ (C_1) \qquad (3.11)$$

This equation implies that a graph of $\ell n\ (\rho E)$ as a function of $1/E$ should yield a straight line if Fowler-Nordheim tunnelling is the conduction process.

This analysis is given in fig. 3.21 for data from heavily-doped specimens containing 0.6 at. % Ho, derived from the resistivity-voltage dependence data in fig. 3.14. It is clear that a curved rather than a straight line is obtained, with greater curvature at lower values of $1/E$, corresponding to higher applied fields. The field dependence of resistivity is therefore unlikely to be a straightforward Fowler-Nordheim tunnelling effect. This certainly appears to be the case for

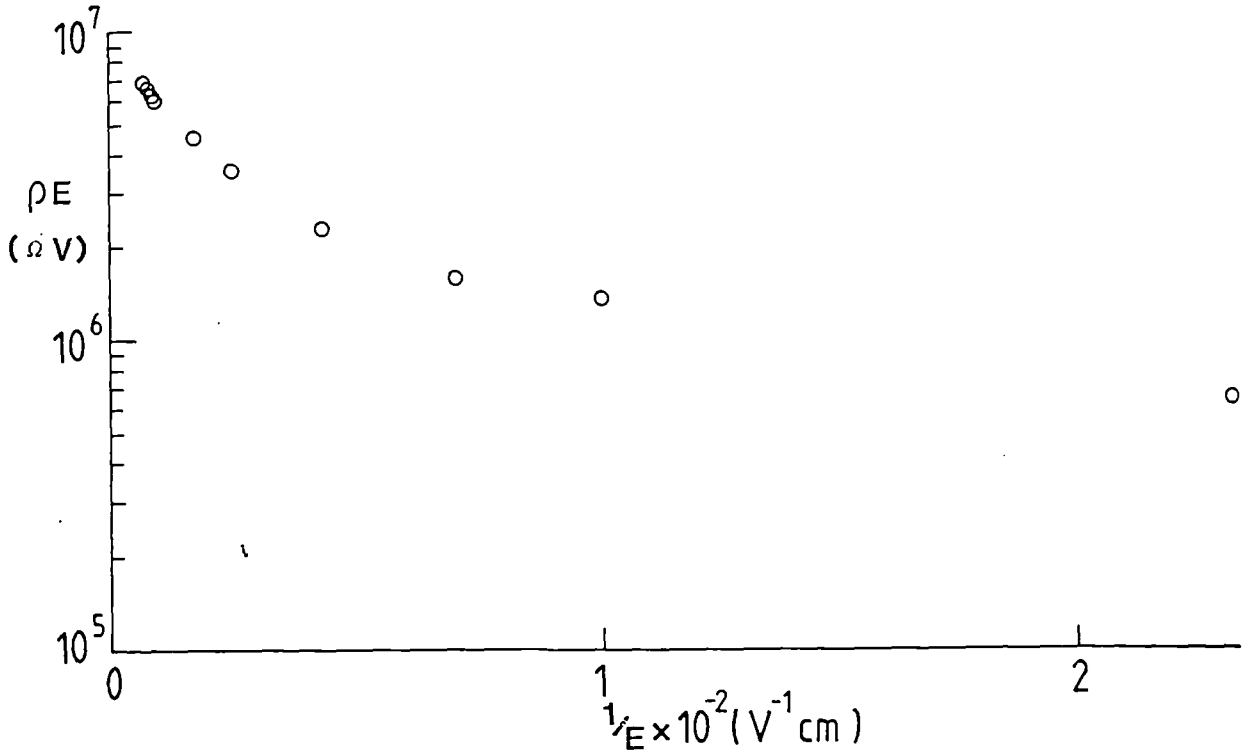

Figure 3.21 Fowler-Nordheim plot for a specimen containing 0.6 at. % Ho.

the more heavily-doped specimens : however, the analysis described above was inapplicable to lightly doped specimens whose behaviour was strongly influenced by self-heating effects.

The increase in resistivity found at higher applied voltages is believed to result from localised heating at the grain boundaries caused by the dissipation of electrical power occurring preferentially at the grain boundaries which are resistive. This conclusion was supported by the fact that pulses of longer duration caused larger increases in resistivity at high applied fields, and is consistent with the observations of Mader et al. [21], who used an infrared technique to detect large temperature rises at grain boundaries when short duration, high voltage pulses were applied to $BaTiO_3$ PTCR ceramics. An approximate calculation was carried out of the power dissipated at the grain boundaries at an applied electric field of 800 Vm^{-1} for the sample in fig. 3.13; this gave a value of ~350 mW cm^{-2}, which is enough to raise the grain boundary temperature significantly.

The same calculation of grain boundary power dissipation was carried out for the heavily-doped ceramics in fig. 3.14; this gave about 7 $\mu W\ cm^{-2}$, which would produce a negligible rise in temperature and explains the observation that the room temperature resistivity of the heavily doped specimens did not increase at higher applied fields. The power dissipation at grain boundaries was reduced because the current passing through the specimens was substantially reduced due to their

higher resistivity; the voltage dropped across each grain boundary was also reduced since the much smaller grain size resulted in a large increase in the number of grain boundaries per unit length.

3.4.2.2 Insulating Intergranular Layer Models

If the formation of an insulating intergranular layer were responsible for the observed increase in the low-temperature resistivity with dopant concentration, the resistivity should be independent of the applied voltage, as stated earlier. In fact a strong dependence of the resistivity on the applied field was observed (fig. 3.12), which was inconsistent with this model. Thus the insulating layer model was not considered to represent a satisfactory mechanism for the observed increase in the low-temperature resistivity seen in fig. 3.9 at higher donor dopant concentrations.

3.4.2.3 Electrical Compensation Models

The results are also thought to show that the models based on a change in the mechanism of electrical compensation of the donor ions cannot give a satisfactory explanation for the observed dependence of low-temperature resistivity on the donor dopant concentration. According to these theories the change from electron to vacancy compensation (see Section 1.6) is presumed to occur throughout the

bulk of the grains; so that an increase in the resistivity of the bulk material would be expected to occur at higher donor dopant concentrations. The dielectric measurements carried out at AF and RF on heavily doped specimens (fig. 3.12) clearly demonstrated instead that the bulk resistivity remained unchanged at ~ 4.7 Ω cm, and that the increase in low-temperature resistivity was therefore purely a grain boundary phenomenon. The possibility of the formation of cation vacancies at high donor dopant concentrations is not excluded entirely by the dielectric results; these investigations, however, indicate that the vacancies must be confined to the grain boundary regions if they do occur. Such an assumption is consistent with theoretical predictions made by Lewis et al. [22].

3.4.2.4 The Daniels Barium Vacancy Model

According to the Ba-vacancy model proposed by Daniels et al [5], the insulating layer in Ba vacancies should have had a thickness of the order ~ 3 μm in view of the cooling rate of 300°C h^{-1} following sintering in the firing profile used (fig. 3.1). The specimens containing 0.6 at. % Ho had a grain size of ~ 2 μm and should accordingly have been totally insulating. In such a circumstance; the usual equivalent circuit no longer applies. In particular, the series bulk resistance component (R_{bulk}) must be replaced by a series capacitive component, C_{bulk}, resulting in complex impedance plots that would pass through the

origin at the high-frequency limit. It can, however, be seen that the dielectric measurement results in fig. 3.12 demonstrate very clearly that the grain bulk remains conducting, (i.e. finite resistance) in contrast with the predictions of the Ba-vacancy model. Although this result does not disprove the existence of an insulating layer, it proves that any such layer had not completely penetrated the grain bulk.

3.4.2.5 Grain Boundary Potential Barrier Enhancement

However, the observation that ρ_{max} and T_{max} were substantially modified as the donor dopant concentration was increased indicates some changes in the characteristics of the grain boundary potential barriers leading to their enhancement and hence to the sharp increase in low-temperature resistivity at high donor dopant concentrations. The existence of this enhancement of the potential barriers is supported by the marked increase in activation energy at low temperatures, as derived from the Arrhenius plots of ρ vs. T^{-1}, at high donor dopant concentrations. Additional support is lent to the postulate that changes in the characteristics of the grain boundary potential barriers occur at high donor dopant concentrations by the variation in acceptor energy E_A with donor dopant concentration revealed in the analysis according to the Ihrig and Puschert model.

There are a number of possible reasons for this enhancement, such as the formation near the grain surfaces of cation vacancies acting

as additional acceptors, as described above, or the creation of a second phase having an increased donor dopant concentration [22,23], perhaps at the grain boundary layer [22], causing under-compensation of the surface charges at the barrier layers by spontaneous ferroelectric polarization. The variation of E_A in the Ihrig-Puschert model appears to be consistent with the formation of new cation vacancies acting as additional acceptors at the grain boundaries. The precise cause of the changes remains a matter for speculation and additional work is required to isolate the precise nature of the effects occurring at the grain boundaries. It might well be useful to conduct an investigation by means of transmission electron microscopy in order to determine whether a second phase is in fact found at high donor dopant concentrations.

3.5 Conclusions

It has been demonstrated that the increase in room temperature resistivity of the ceramics at high donor dopant concentrations, which results in a transition from conductive to insulating behaviour, is exclusively a grain boundary phenomenon. Dielectric measurements showed the transition to be associated with increased grain boundary resistance, whilst the grain bulk resistivity remained unaltered. Daniels et al's postulate that the transition was caused by the extension of the grain boundary depletion layer throughout the grain bulk as the grain

size fell at high dopant concentrations, would therefore appear to be inapplicable. An alternative explanation of the transition which proposed the formation of an insulating intergranular second phase at high donor dopant concentrations, was disproved by measurements of room temperature resistivity as a function of the applied electric field.

Analysis of the resistivity-temperature characteristics of the ceramics using Ihrig and Puschert's model revealed behaviour consistent with higher grain boundary acceptor state density, accompanied by an increase in acceptor state activation energy, at high donor dopant concentrations. The mechanism causing these changes is not yet clear. It is concluded that the increased acceptor state density and activation energy increases the height of the grain boundary potential barrier and modifies the PTCR characteristics to produce the transition from conductive to insulating behaviour in heavily-doped specimens.

References

1. Heywang, W., Solid State Electron., 3, 51 (1961).
2. Brauer, M., Z. Angew. Phys., 23, 373 (1967).
3. Heywang, W., J. Am. Ceram. Soc., 6, 1214 (1971).
4. Jonker, G. H., Mat. Res. Bull., 2, 401 (1967).
5. Daniels, J., Hardtl, K. H. and Wernicke, R., Philips Tech. Rev., 38, 73 (1978/9).
6. Daniels, J. and Wernicke, R., Philips Res. Rep., 31, 544 (1976).

7. Wernicke, R., Phys. Stat. Sol. (a), 47, 139 (1978).

8. Murukami, T., Miyashita, T., Nakahara, M. and Sekine, E., J. Am. Ceram. Soc., 56, 294 (1973).

9. Kahn, M., J. Am. Ceram. Soc., 54, 452 (1971).

10. Jonker, G. M., Solid State Electron., 7, 895 (1964).

11. Eror, N. G. and Smyth, D. M., The Chemistry of Extended Defects in Non-Metallic Solids, Ed. LeRoy Eyring and H. O'Keeffe (Amsterdam : North Holland), p62 (1970).

12. Heywang, W., J. Am. Ceram. Soc., 47, 484 (1964).

13. Sauer, H. A. and Fisher, J. R., J. Am. Ceram. Soc., 43, 297 (1960).

14. Tennery, V. J. and Cook, R. C., J. Am. Ceram. Soc., 44, 187 (1961).

15. Basu, R. N. and Maiti, H. B., Proc. IEEE Int. Symp. Applications of Ferroelectrics (Gehigh Univ., USA) ed. Ian Wood (New York : IEEE), p685 (1986).

16. Jonker, G. H. and Havinga, E. E., Mat. Res. Bull., 17, 345 (1982).

17. Ueda, I. and Ikegami, S., J. Phys. Soc. Jpn, 20, 546 (1965).

18. Drofenik, M., J. Am. Ceram. Soc., 70, 311 (1987).

19. Basu, R. N. and Maiti, H. B., Trans. Indian Ceram. Soc., 45, 140 (1986).

20. Ihrig, H. and Puschert, W., J. Appl. Phys., 48, 3081 (1977).

21. Mader, M., Meixner, H. and Kleinschmidt, P., J. Appl. Phys., 56, 282 (1984).

22. Lewis, G. V., Catlow, C. R. A. and Casselton, R. E. W., J. Am. Ceram. Soc., 68, 555 (1985).

23. Muruguraj, P. and Kutty, T. R. N., Mat. Res. Bull., 20, 1473 (1985).

24. Molokhia, N. M., Issa, M. A. A. and Nasser, S. A., J. Am. Ceram. Soc., 67, 289 (1984).

25. Sze, S. M., Physics of Semiconductor Devices, 2nd Edition, p497, Wiley (1981).

26. Johnson, C. J., Appl. Phys. Lett., 7, 221 (1965).

27. Al-Allak, H. M., Brinkman, A. W., Russell, G. J. and Woods J., J. Appl. Phys., 63, 4530 (1988).

CHAPTER 4

THE EFFECTS OF ANNEALING

4.1 Introduction

Although the Heywang model [1] as extended by Jonker [2,3] (Chapter 1) gives the most commonly accepted explanation for the PTCR effect in n-doped $BaTiO_3$ ceramics sintered in air, certain aspects of the model are not yet fully understood. In particular, the nature of the postulated acceptor states in the region of the grain surfaces, which are believed to be responsible for the creation of the space charge layer and potential barrier at the grain boundaries, still remains unresolved.

As discussed previously, Heywang assumed the existence of a two-dimensional surface layer of electronic states with acceptor characteristics, which might be produced by adsorbed oxygen atoms at the grain surfaces. Daniels et al.[4,5], however, in a subsequent study proposed that the acceptors at the grain boundary layer consist of Ba vacancies which form a three-dimensional layer extending from the grain surfaces into the bulk of the grains. Heywang's original model may therefore be regarded as a limiting case of the Daniels model for fast cooling rates when the Ba vacancies are confined to the grain boundaries. In addition, later work by Al-Allak et al. [6] postulated the existence of an additional resistive layer, introduced during the cooling process, in series with the space charge layer.

According to the Daniels model, the distribution of Ba vacancies near the grain boundaries should be significantly affected by high temperature treatment such as annealing of the ceramic after sintering, with consequent alteration of the electrical properties. In particular

increasing the sintering temperature or the annealing time should result in increased peak resistivity as well as a steeper PTCR characteristic. This chapter presents the results of a study of the effect of annealing in an oxygen-containing environment on the properties of $BaTiO_3$ PTCR devices.

4.2 Experimental Method

4.2.1 Specimen Preparation

Barium titanate PTCR ceramic specimens containing 0.1, 0.2, 0.3 and 0.4 atomic % Ho (acting as a donor dopant) were prepared (as described in Sections 2.1.1 and 2.1.2) according to the formulation $Ba_{1-x}Ho_xTiO_3$. After combustion of the organic binder at 600°C, the temperature was increased at a rate of 900°C h^{-1} to 1380°C and maintained at that value for 30 minutes while sintering occurred (Fig. 4.1). After sintering, the furnace was cooled at 300°C h^{-1} to 1220°C and the specimens were annealed at that temperature for varying periods, between 30 minutes and 27 hours. The furnace was then cooled at 300°C h^{-1} down to 800°C, and thereafter at its natural cooling rate to room temperature. A flow of air at 1 ℓ min^{-1} was maintained through the tube throughout the entire firing cycle in order to maintain a constant ambient atmosphere during firing.

4.2.2 Electrical Measurements

Using InGa alloy contacts, resistivity vs. temperature characteristics of the ceramics were obtained, over a temperature range

of approximately 40° to 320°C using the DC two probe measurement technique described earlier in Section 2.4.1.

Selected specimens of various dopant concentrations and annealing histories were reduced in thickness to ~ 0.7 mm and attempts were made to measure the dielectric properties at room temperature as described in Section 2.4.2. It was, however, found that the measurements could not be carried out because of the low resistance of the specimens which prevented balancing the bridge and the Q meter.

4.3 Experimental Results

4.3.1 The Influence of Annealing Time on the Grain Structure

The grain structures of the free surfaces of specimens containing 0.1, 0.2, 0.3 and 0.4 at. % Ho annealed for 1, 12 and 27 hours were studied using scanning electron microscopy : the resulting micrographs are reproduced in figs. 4.2-4.5 and values of mean grain size and standard deviation are given in table 4.1. It is apparent that increasing the Ho concentration from 0.1 at. % to 0.4 at. % corresponded to a decrease in mean grain diameter from 21 μm to 4.9 μm and in standard deviation from 0.9 μm to 0.2 μm, but that altering the sintering time had no significant effect on the size of grains and their distribution, or on grain shapes. The reduction in grain size at higher Ho concentrations is analogous to that observed in the study described in Chapter 3, although the values of grain sizes observed in this investigation were generally smaller. It may be noted that the same

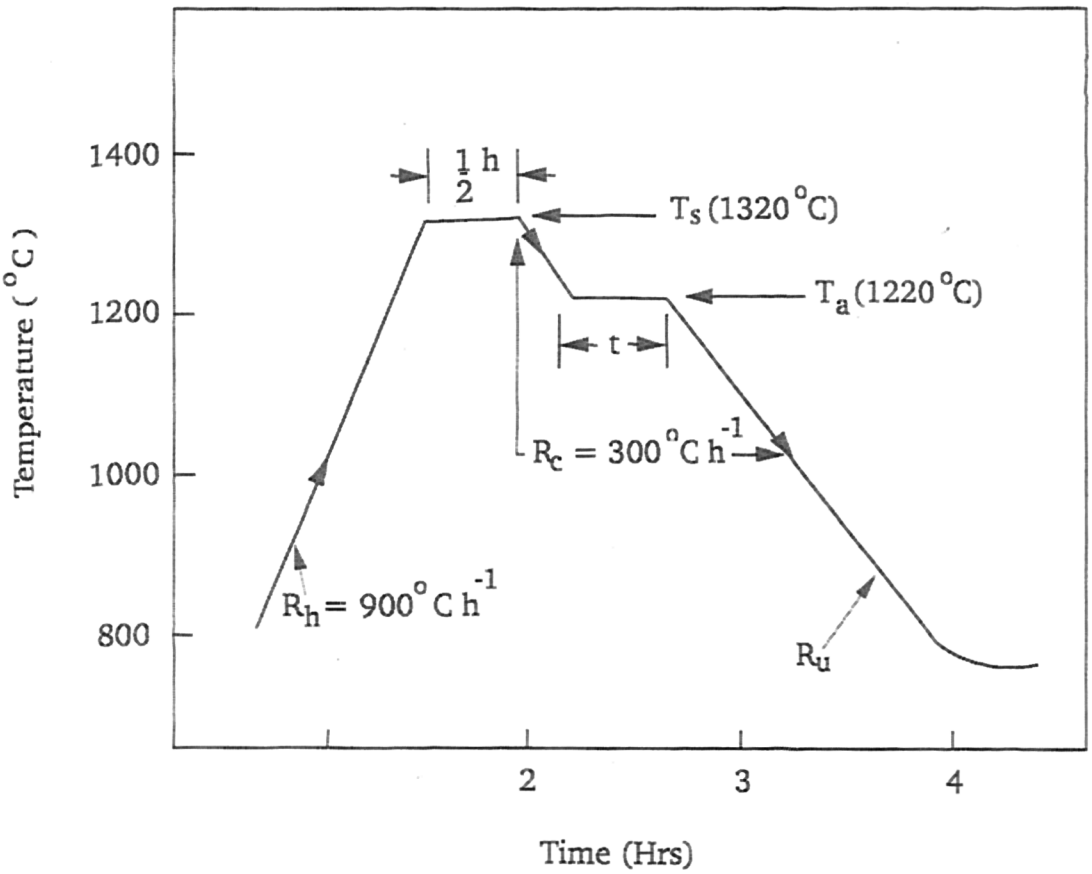

Figure 4.1 Sintering profile used for specimen preparation.

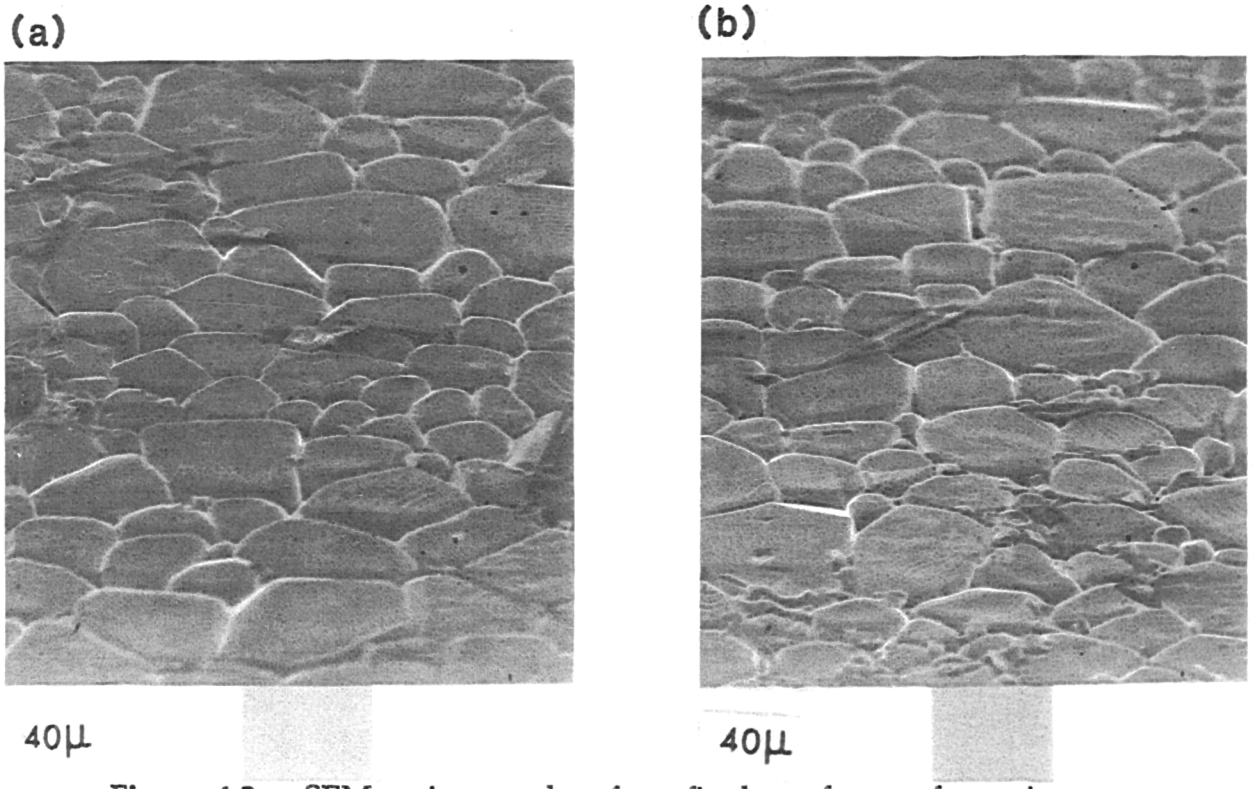

Figure 4.2 SEM micrograph of as-fired surfaces of specimens containing 0.1 at.% Ho annealed for (a) 1hr and (b) 12 hrs.

batches of precursor mixture were used for the fabrication of specimens of a given composition (i.e. donor dopant concentration) used in this study and in the investigation described in Chapter 3. The firing profiles used in the two investigations, however, differed significantly (figs. 4.1 and 3.1); a sintering temperature of 1420°C was used in the previous study compared with 1380°C in the present case.

Quantities of a second phase, generally observed in the form of needle-like structures on the free surface of the specimens, were observed in the lightly-doped (0.1 and 0.2 at. % Ho) ceramics (figs. 4.6 and 4.7). The second phase was not observed in the more heavily-doped ceramics. Analysis of the second phase by the EDX technique (figs. 4.8 and 4.9) revealed that it was rich in Si and TiO_2 relative to the bulk of the adjacent grains. These observations are similar to those reported in Chapter 3.

4.3.2 Resistivity vs. Temperature Plots

A number of plots of resistivity vs. temperature for different ceramic compositions and annealing times are reproduced in figs. 4.10 to 4.19. Each experimental point represents a mean value of measurements carried out on five samples from the same batch; the estimated error in resistivity for each point is $\pm$ 10%. It may be seen that increasing the annealing time at 1220°C in air corresponds with (i) an increase in the steepness of the plots in the region of transition between low and high resistivity, (ii) an increase in the value of both maximum resistivity ρ_{max} and minimum resistivity ρ_{min} and (iii) a reduction in T_{max}, the temperature at which ρ_{max} occurs. Numerical

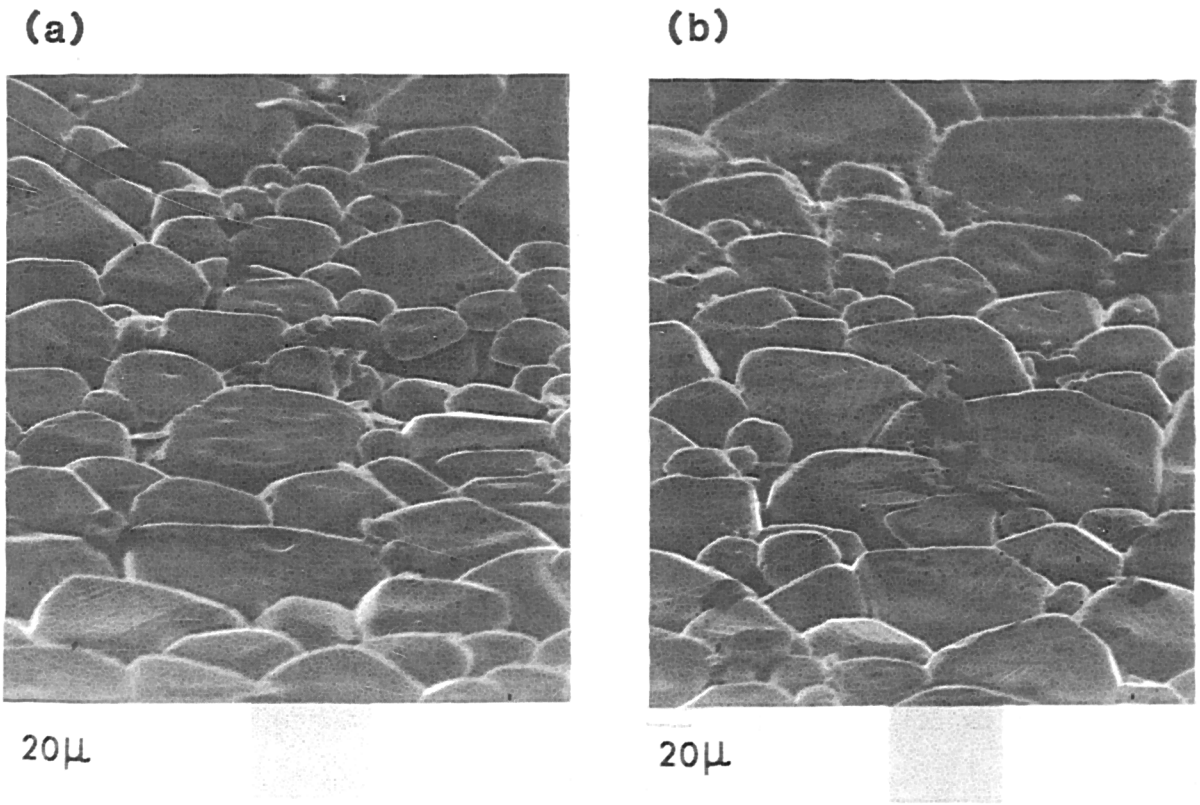

Figure 4.3 SEM micrograph of as-fired surfaces of specimens containing 0.2 at.% Ho annealed for (a) 1hr and (b) 12 hrs.

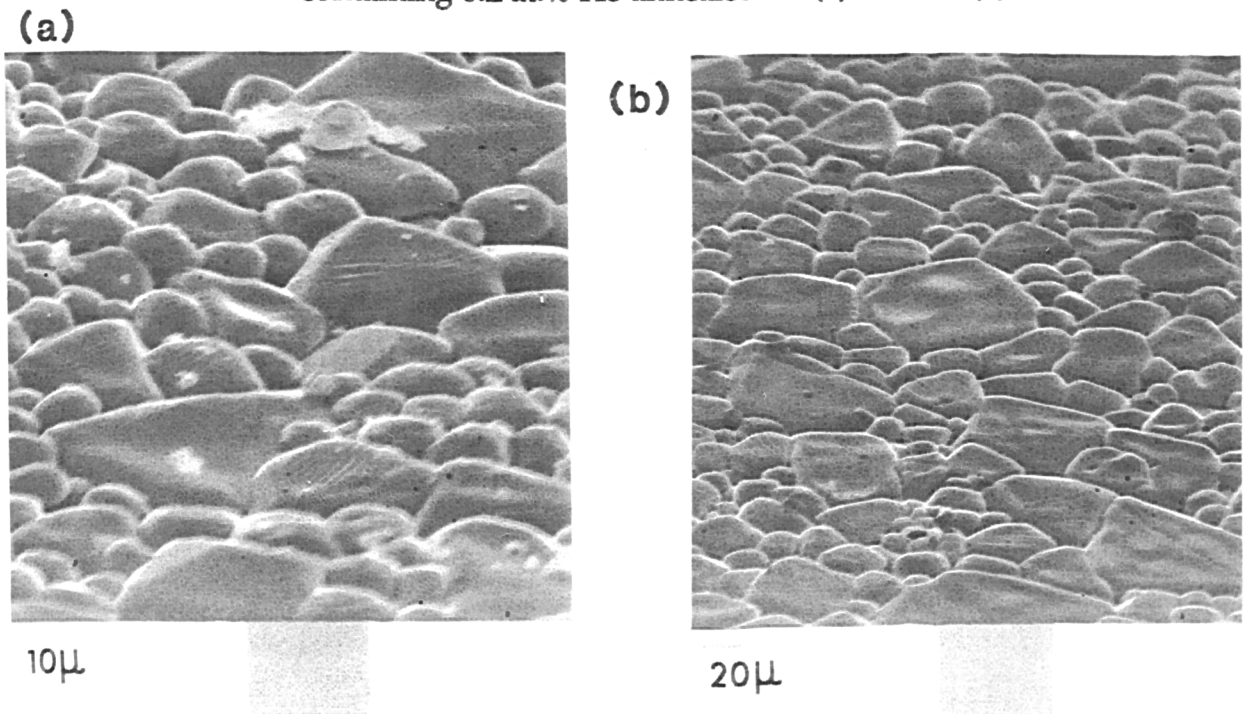

Figure 4.4 SEM micrograph of as-fired surfaces of specimens containing 0.3 at.% Ho annealed for (a) 1hr and (b) 12 hrs.

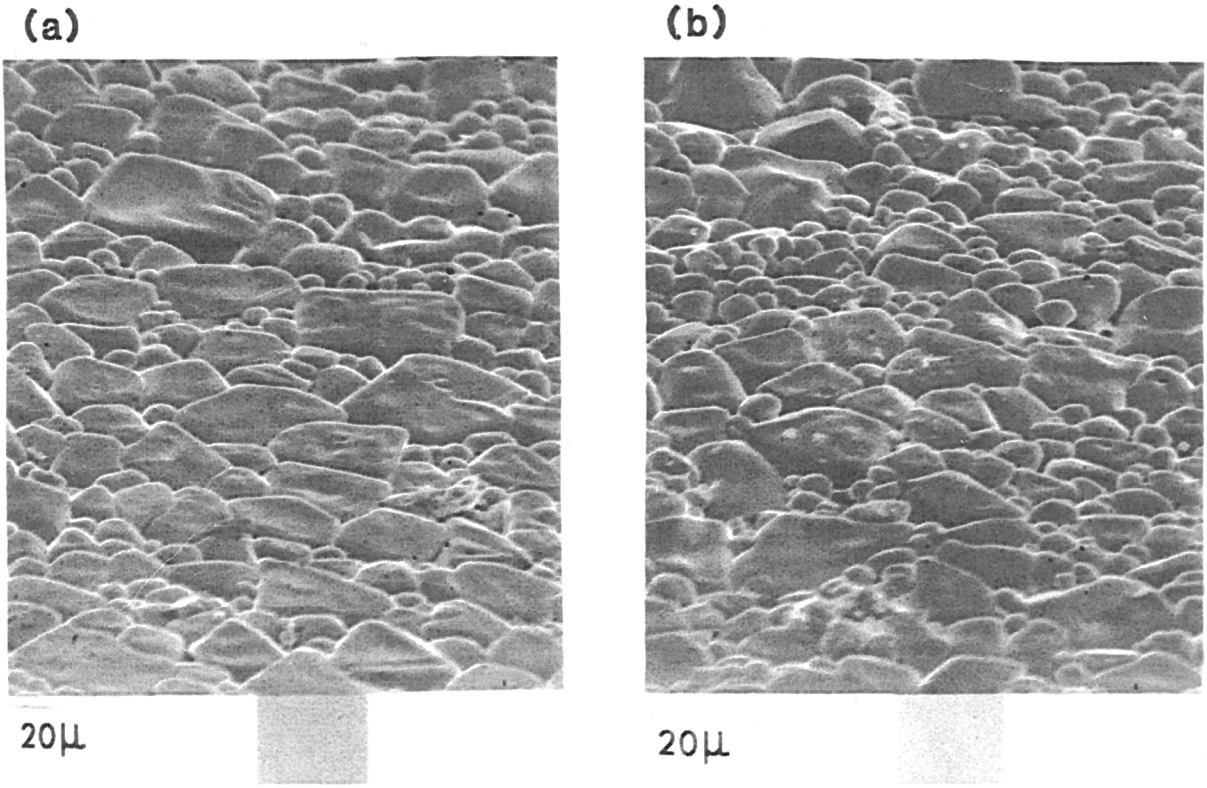

Figure 4.5 SEM micrograph of as-fired surfaces of specimens containing 0.4 at.% Ho annealed for (a) 1hr and (b) 12 hrs.

Table 4.1

Mean Grain Size Values

Specimen Composition	Grain Diameter d (μm)	Std. Dev.
0.1 at. % Ho	21	± 0.9
0.2 at. % Ho	13.4	± 0.7
0.3 at. % Ho	8.3	± 0.3
0.4 at. % Ho	7.9	± 0.2

values of these parameters for the various compositions and annealing times are given in table 4.2. The trends in the variation of these parameters with annealing time are seen to be similar for all the ceramic compositions investigated, although the variations are not monotonic. The dependence of ρ_{max} and ρ_{min}, together with the ratio ρ_{max}/ρ_{min} (which governs the magnitude of the PTCR effect) on the annealing time is illustrated for each donor dopant concentration in figs. 4.20 to 4.23. As the annealing time was increased from ½ hour to 27 hours, both ρ_{max} and ρ_{min} were observed to increase, ρ_{max} doing so more rapidly, so that ρ_{max}/ρ_{min} approximately doubled over this range of annealing times; similar behaviour was observed for all the ceramic compositions.

4.3.3 Reduction and Reoxidation Experiments

Some measured samples which had originally been annealed for 27 hours in air, were reduced by heating in a stream of N_2 (oxygen partial pressure = 10^{-6} bar) at 1220°C for 3 hours in the tube furnace, after first removing the electrodes by abrasion. After cooling down to room temperature, electrodes were again placed on the specimens and their resistivities measured as a function of temperature. The electrodes were again removed and the samples heated in a stream of air at 1220°C for 3 hours in the tube furnace. Again the specimens were allowed to cool, electrodes were attached and resistivity-temperature plots made. Fig. 4.24 shows the ρ-T plots for samples of different donor dopant concentration after reduction in an N_2 atmosphere, and

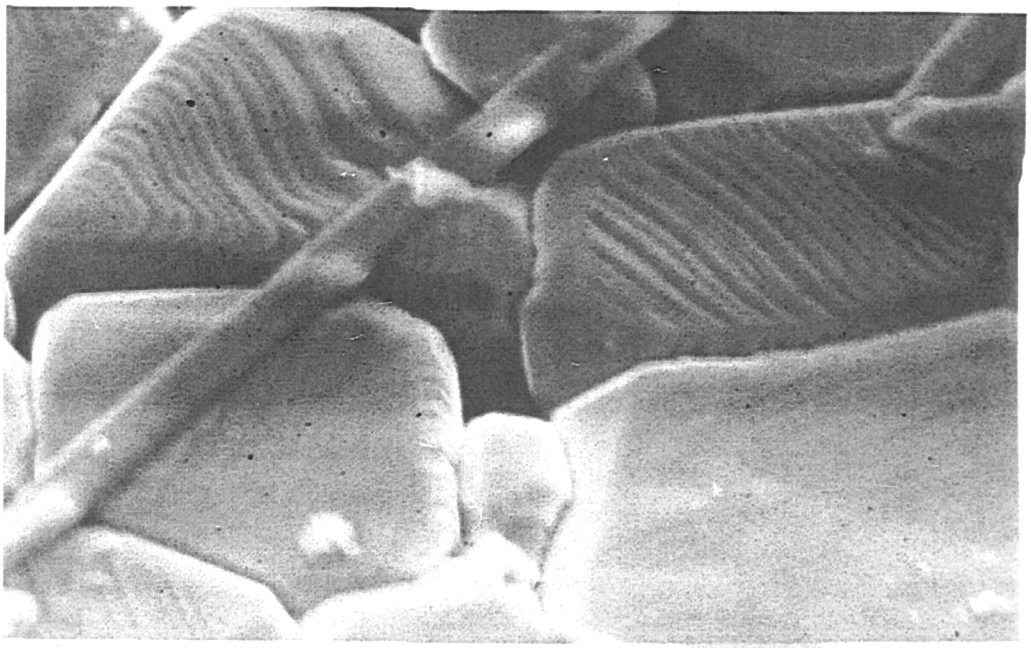

Figure 4.6 SEM micrograph of as-fired surface of specimen containing 0.1 at. % Ho annealed for 12 hrs.

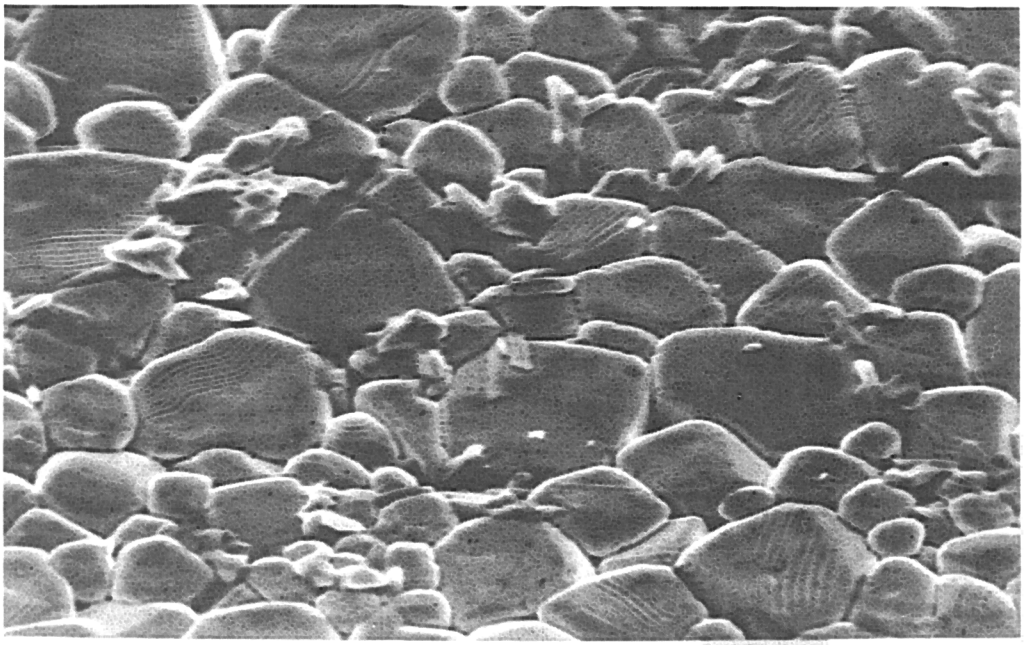

Figure 4.7 SEM micrograph of as-fired surface of specimen containing 0.2 at. % Ho annealed for 12 hrs.

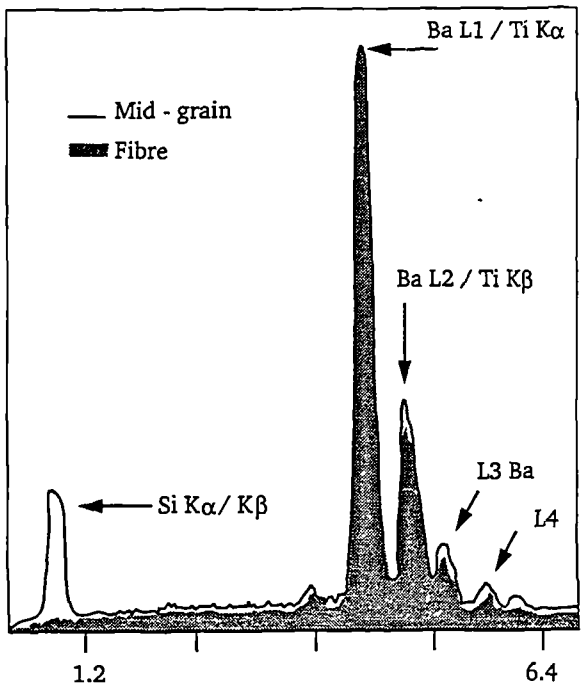

Figure 4.8 EDX spectrum for a specimen containing 0.1 at. % Ho.

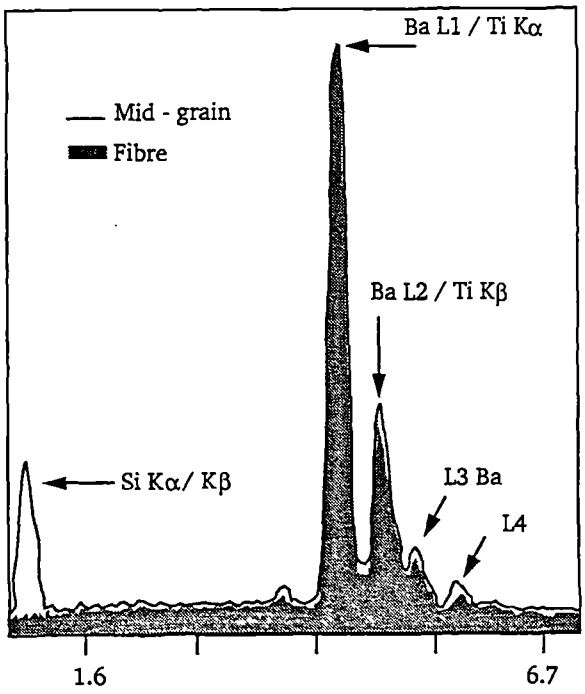

Figure 4.9 EDX spectrum for a specimen containing 0.2 at. % Ho.

fig. 4.25 gives the corresponding ρ-T characteristics for the same devices after reoxidation in air. Fig. 4.24 shows that reduction in N_2 was followed by a considerable diminution in PTCR behaviour for all the ceramic compositions investigated; the reduction was most marked in the case of the 0.4 at. % Ho samples, where ρ_{max} fell by about 1 order of magnitude. A corresponding, though much smaller, fall in ρ_{min} was observed for each composition after reduction. After reoxidation, however, the PTCR effect was restored in each case (fig. 4.25) with the ρ-T curves strongly resembling the original ρ-T plots measured before the reduction treatment (figs. 4.17, 4.15).

4.3.4 Activation Energy Analysis

Arrhenius plots of $\ell n\ \rho$ against T^{-1} at temperatures below the transition temperature for ceramic specimens containing 0.1, 0.2, 0.3 and 0.4 at. % Ho annealed in at 1220°C for 4 hours and 27 hours are shown in figs. 4.26 to 4.33. The analysis of the Arrhenius plot in terms of the Heywang theory to account for grain boundary potential barriers is identical to that developed in Chapter 3.

The straight lines given by the Arrhenius plots in figs. 4.26 to 4.33 demonstrate the presence of potential barriers at temperatures below T_C in the ceramics; the heights of the potential barriers are given in table 4. The rather large errors in the values of the potential barrier heights arise from errors in the measurement of relatively low values of specimen resistance using the ρ-T plotting apparatus. It is apparent that the potential barrier height for each specimen composition shows a definite increase with increasing time from 4 hours to 27 hours.

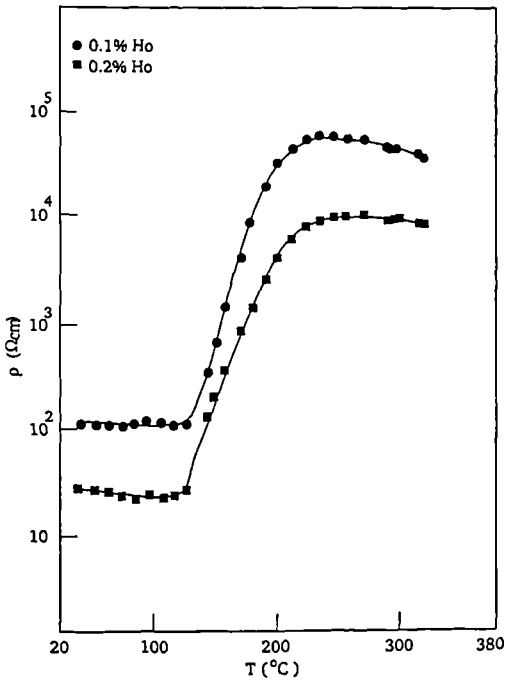

Figure 4.10 Dependence of resistivity ρ on temperature T for specimens containing 0.1 and 0.2 at. % Ho, annealed for 1 hr.

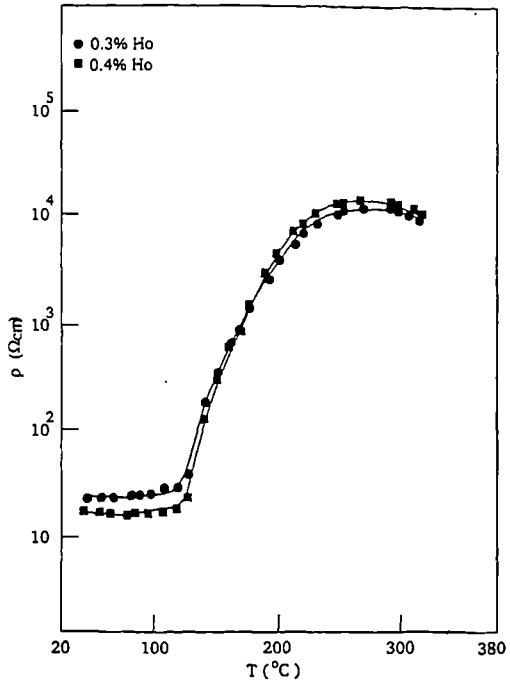

Figure 4.11 Dependence of resistivity ρ on temperature T for specimens containing 0.3 and 0.4 at. % Ho, annealed for 1 hr.

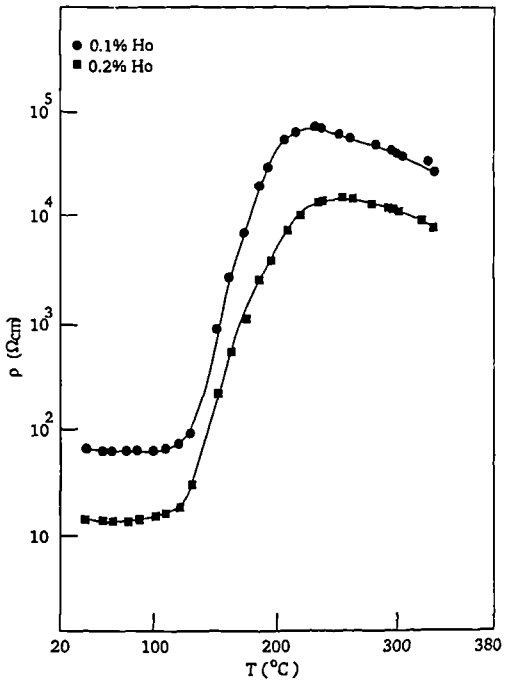

Figure 4.12 Dependence of resistivity ρ on temperature T for specimens containing 0.1 and 0.2 at. % Ho, annealed for 3 hrs.

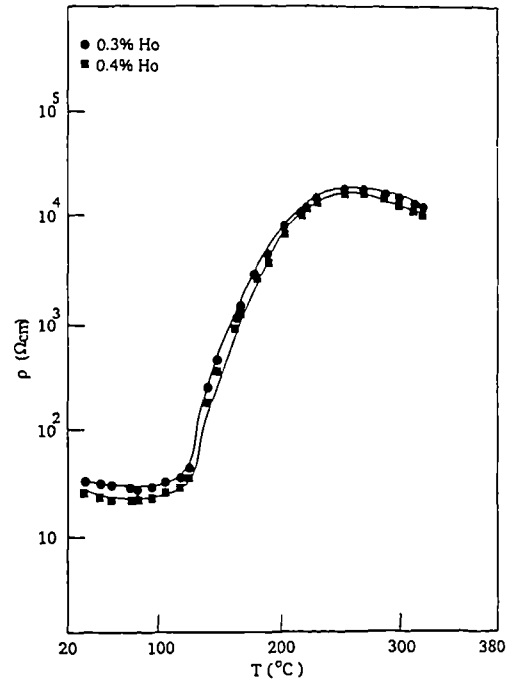

Figure 4.13 Dependence of resistivity ρ on temperature T for specimens containing 0.3 and 0.4 at. % Ho, annealed for 3 hrs.

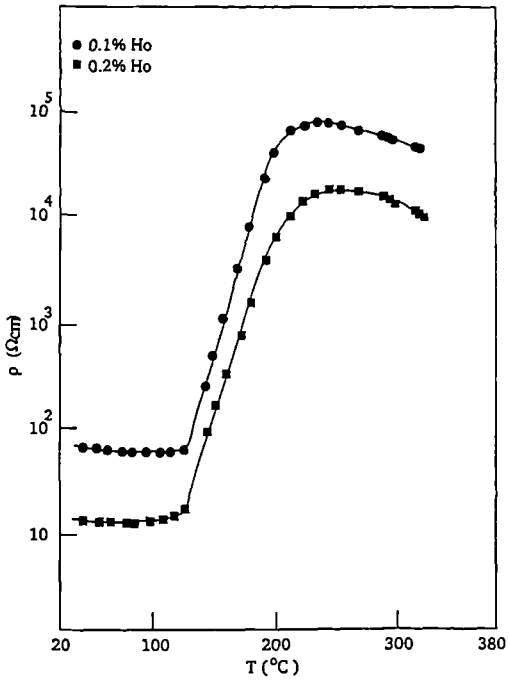

Figure 4.14 Dependence of resistivity ρ on temperature T for specimens containing 0.1 and 0.2 at. % Ho, annealed for 4 hrs.

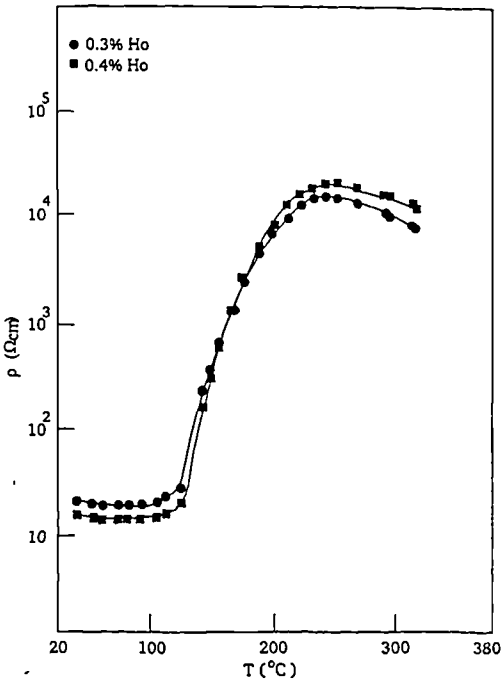

Figure 4.15 Dependence of resistivity ρ on temperature T for specimens containing 0.3 and 0.4 at. % Ho, annealed for 4 hrs.

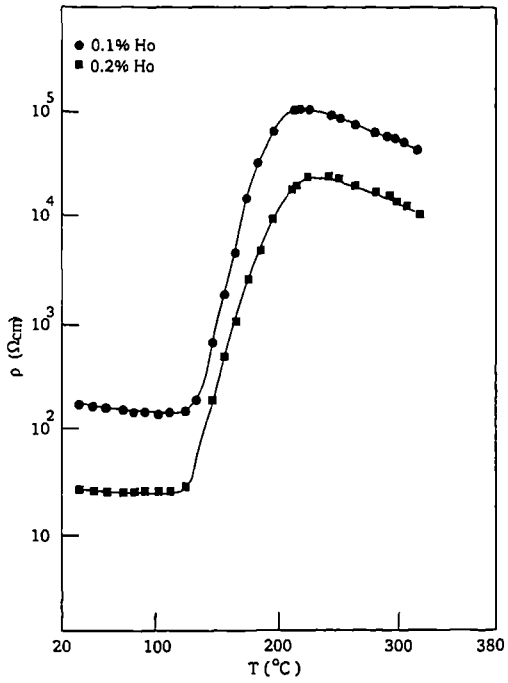

Figure 4.16 Dependence of resistivity ρ on temperature T for specimens containing 0.1 and 0.2 at. % Ho, annealed for 12 hrs.

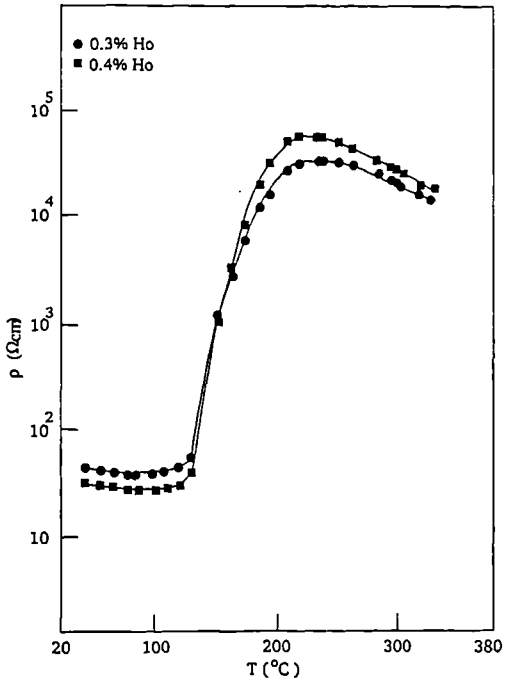

Figure 4.17 Dependence of resistivity ρ on temperature T for specimens containing 0.3 and 0.4 at. % Ho, annealed for 12 hrs.

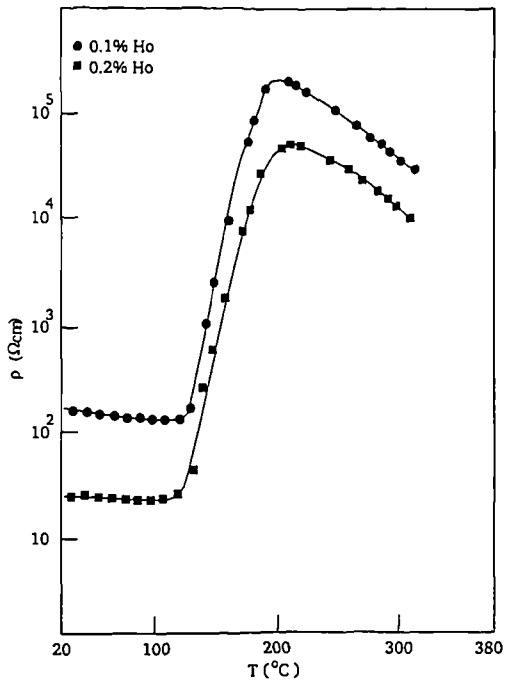

Figure 4.18 Dependence of resistivity ρ on temperature T for specimens containing 0.1 and 0.2 at. % Ho, annealed for 27 hrs.

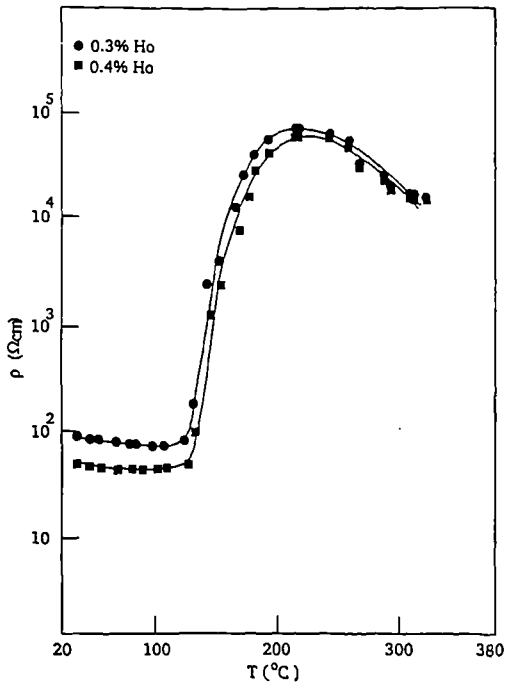

Figure 4.19 Dependence of resistivity ρ on temperature T for specimens containing 0.3 and 0.4 at. % Ho, annealed for 27 hrs.

4.3.5 Peak Resistivity Analysis

The influence of annealing or the PTCR characteristics of ceramics of different composition was further analysed by means of ρ_{max} vs. T_{max} diagrams as first employed by Jonker [3]. Values of ρ_{max} and T_{max} were calculated from the Heywang equations, using the method of Ihrig and Puschert [7] described in Appendix A2, for a number of different values of acceptor energy E_A and effective acceptor density N_{A0}. A map of the calculated values of (ρ_{max}, T_{max}) over all E_A and N_{A0} of interest was then constructed for comparison with the experimental data.

Values chosen for the Curie temperature, T_C = 388 K [8], the Curie constant C = 1.2 x 10^3K [8] and the effective density of states in the conduction band N_C = 1.5 x 10^{22} cm^{-3} (equal to the Ti^{4+} ion density) were identical to the values selected in the previous study (described in Chapter 3) using this model. The absence of data from dielectric measurement precluded the derivation of values of charge carrier concentration n from the grain bulk resistivity ρ_{bulk} of the various specimens. An *a priori* assumption that n = 2.67 x 10^{18} cm^{-3} was therefore made : this value was identical to the measured and estimated values adopted in the previous work. This assumption was justified by reference to the results in Chapter 3 and of several other investigations [6], in which it was shown by means of dielectric measurements that variations in PTCR behaviour arose as a result of changes in the resistance at grain boundaries, and that the resistivity of

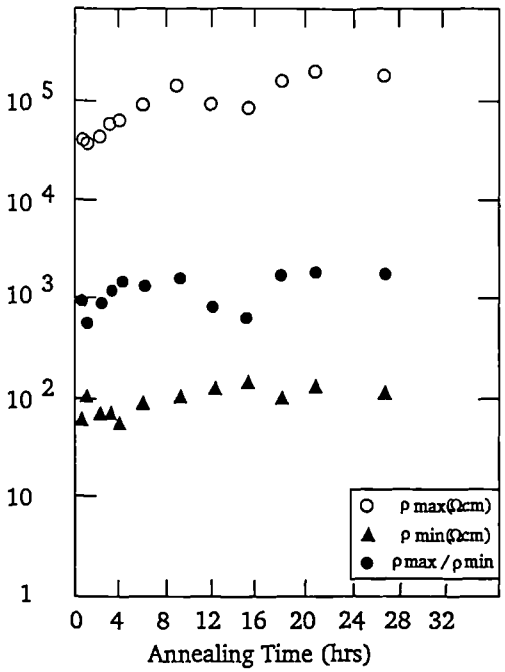

Figure 4.20 Resistivity ratio as a function of annealing time for specimens containing 0.1 at. % Ho.

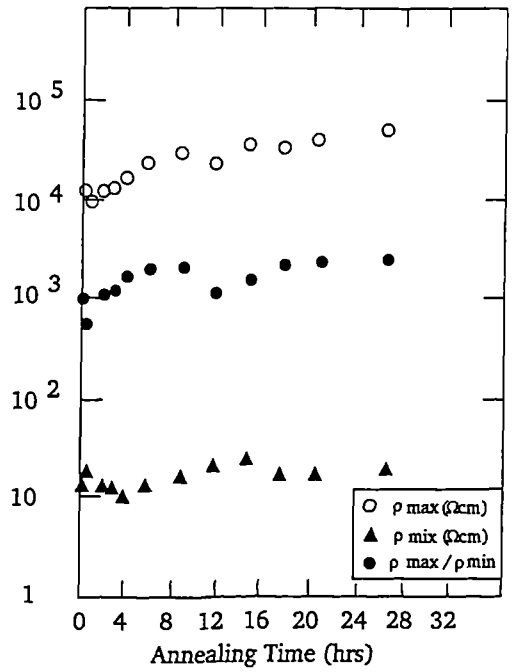

Figure 4.21 Resistivity ratio as a function of annealing time for specimens containing 0.2 at. % Ho.

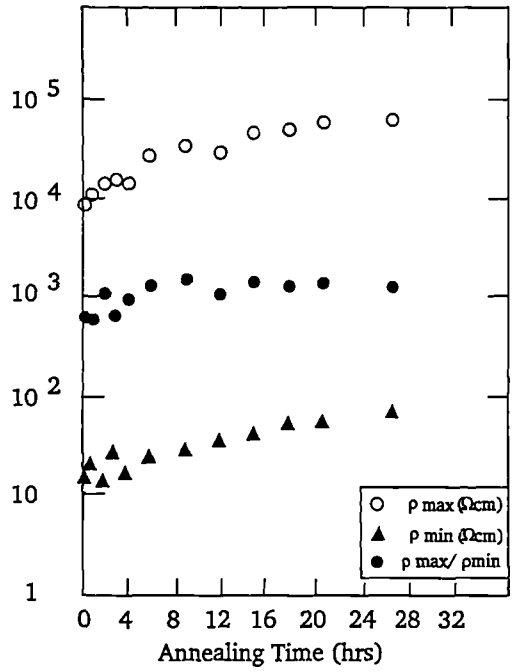

Figure 4.22 Resistivity ratio as a function of annealing time for specimens containing 0.3 at. % Ho.

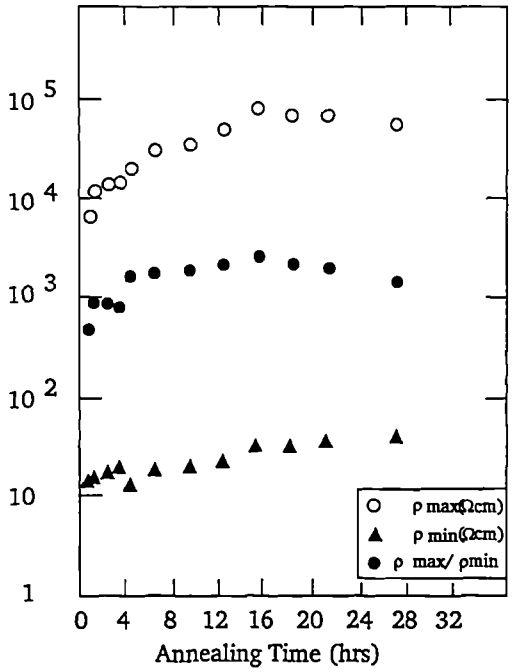

Figure 4.23 Resistivity ratio as a function of annealing time for specimens containing 0.4 at. % Ho.

the grain bulk appeared to be unchanged over a wide range of donor dopant concentrations and sintering conditions. The adoption of the value of n derived from the previous study was additionally supported by the fact that specimens of the same donor dopant composition were produced from the same batches of precursor mixture for the two investigations; the chemical composition of specimens of the same nominal Ho content should therefore be identical, and possible effects caused by variations in the amount of acceptor impurities present (invariably present in trace amounts) should therefore be eliminated.

Curves of ρ_{max} vs. T_{max} for specimens containing 0.1, 0.2, 0.3 and 0.4 at. % Ho are given in figs. 4.34 to 4.37; the values of mean grain diameter d used in calculation of the curves were those derived from SEM micrographs of the specimens and listed in table 4.3. Measured values of ρ_{max} and T_{max} from the specimens of different Ho content and annealing history were also plotted on the (ρ_{max}, T_{max}) maps of figs. 4.34 to 4.37. It is seen that the (ρ_{max} , T_{max}) values of each ceramic composition lie close to lines corresponding to E_A = 1.1 eV in the maps. At each donor dopant concentration, a definite trend was observed towards higher values of effective donor dopant concentration N_{A0} as the length of the annealing time was increased; this observation is related to the trend towards higher ρ_{max} and lower T_{max} at longer annealing times reported in section 4.3.2. The observed trend is not, however, strictly monotonic; this is attributed to the errors in the measurement of ρ_{max} and T_{max}, as mentioned earlier.

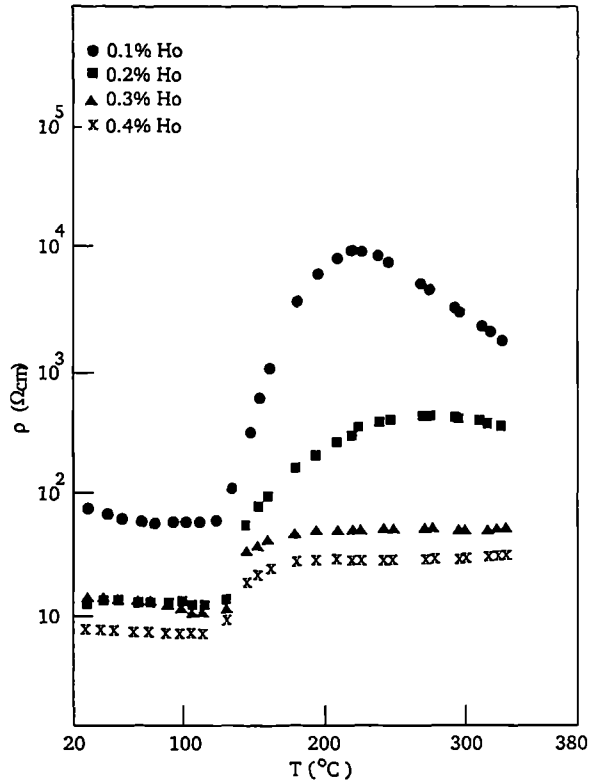

Figure 4.24 Resistivity-temperature plots for reduced specimens.

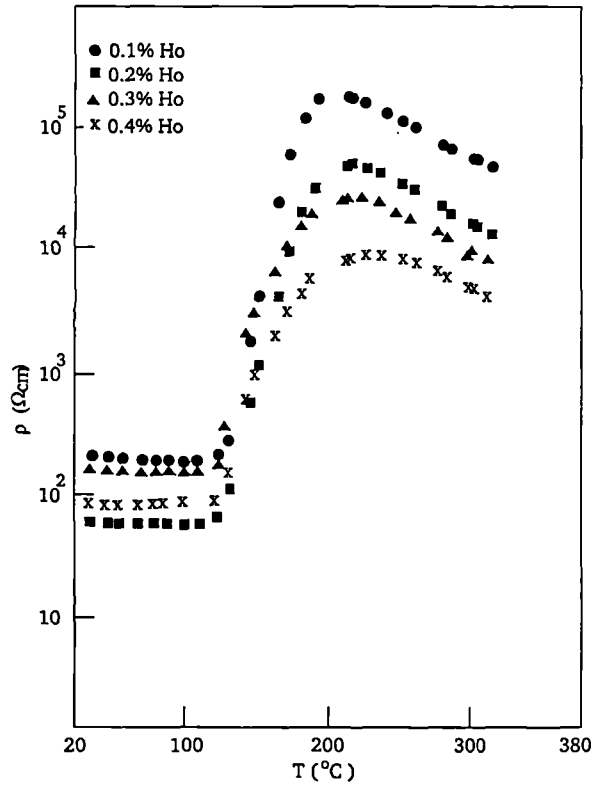

Figure 4.25 Resistivity-temperature plots for reoxidised specimens.

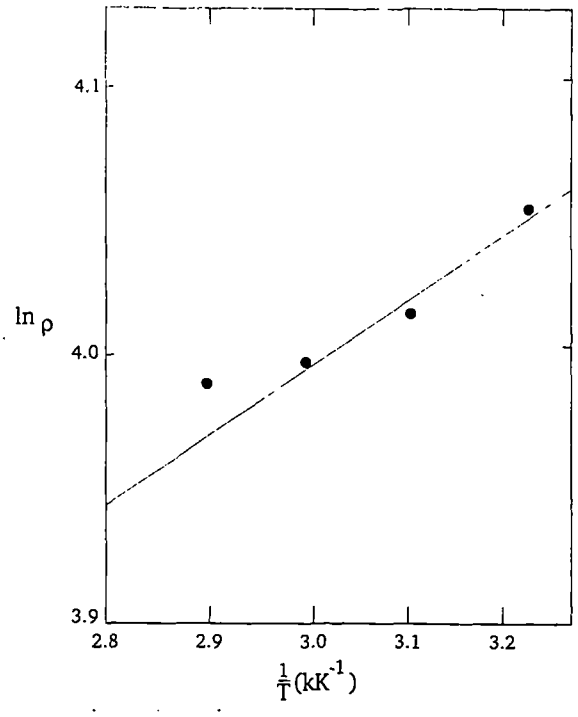

Figure 4.26 Arrhenius plot for specimens containing 0.1 at. % Ho annealed for 4 hrs.

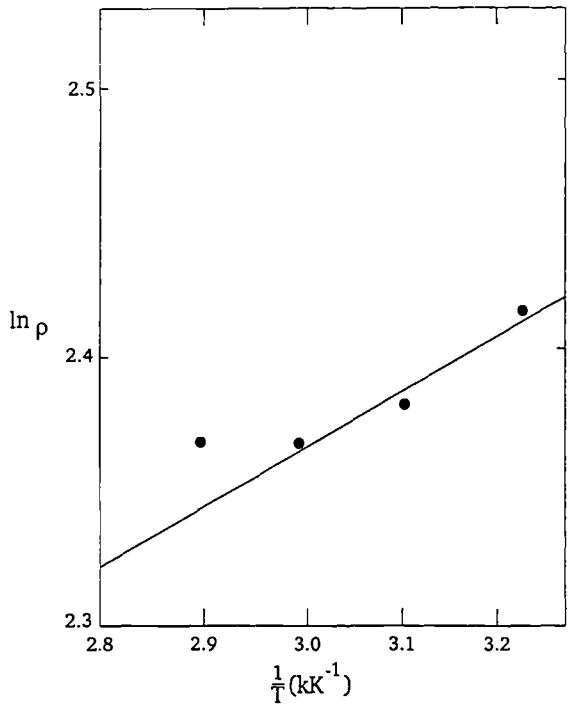

Figure 4.27 Arrhenius plot for specimens containing 0.2 at. % Ho annealed for 4 hrs.

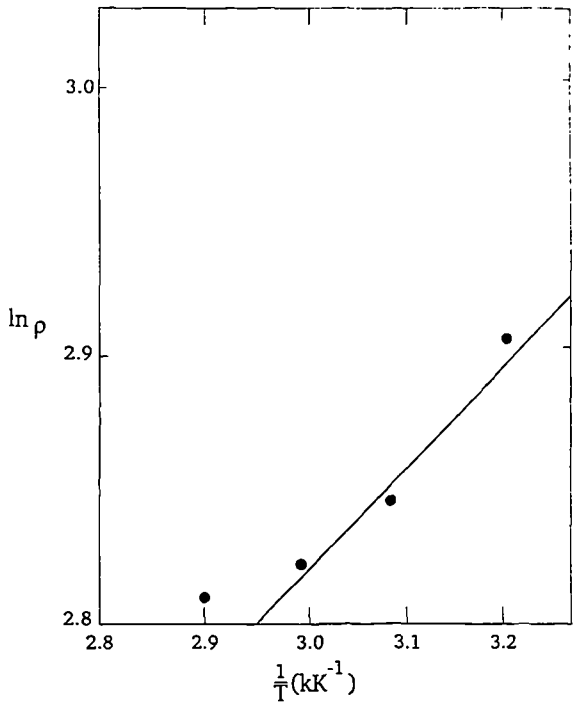

Figure 4.28 Arrhenius plot for specimens containing 0.3 at. % Ho annealed for 4 hrs.

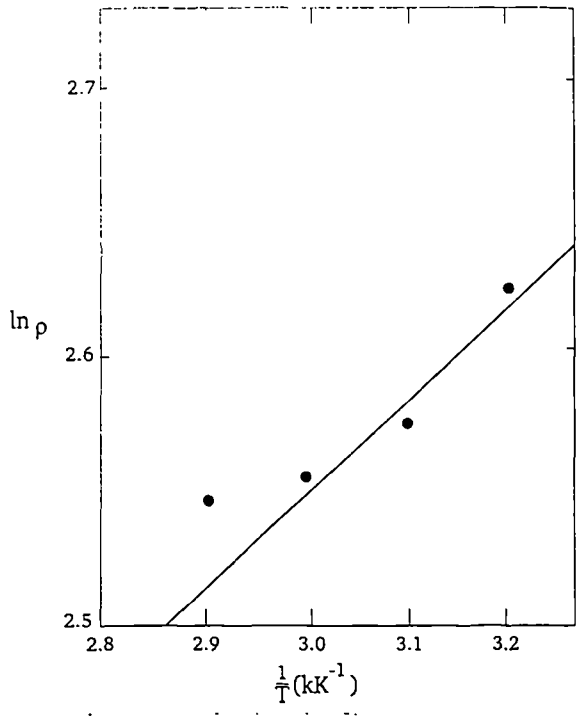

Figure 4.29 Arrhenius plot for specimens containing 0.4 at. % Ho annealed for 4 hrs.

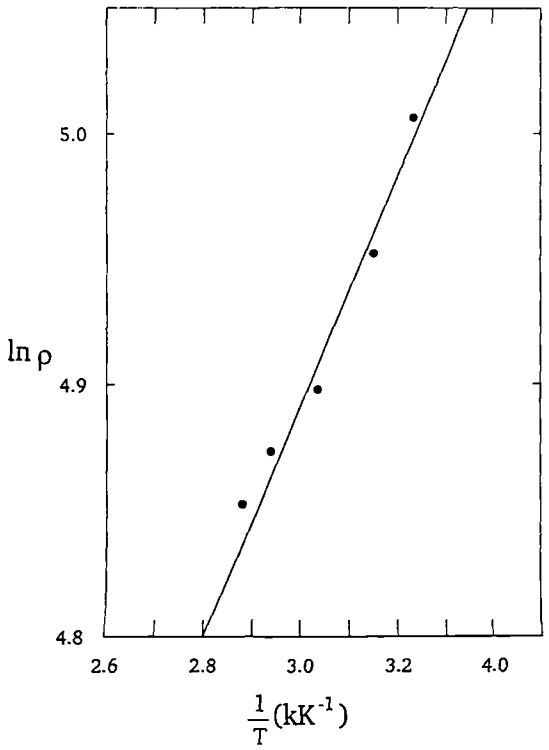

Figure 4.30 Arrhenius plot for specimens containing 0.1 at. % Ho annealed for 27 hrs.

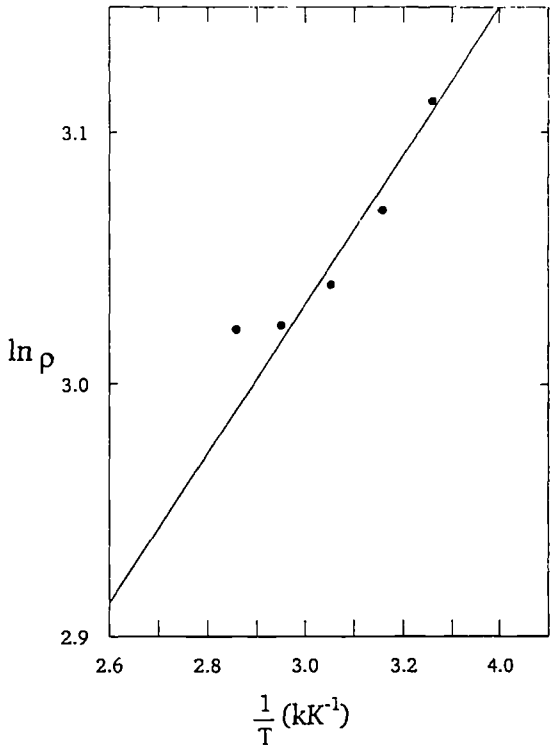

Figure 4.31 Arrhenius plot for specimens containing 0.2 at. % Ho annealed for 27 hrs.

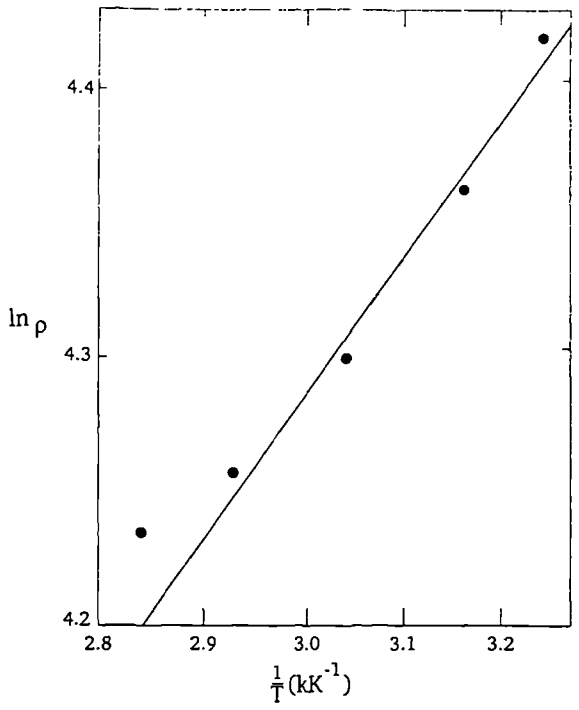

Figure 4.32 Arrhenius plot for specimens containing 0.3 at. % Ho annealed for 27 hrs.

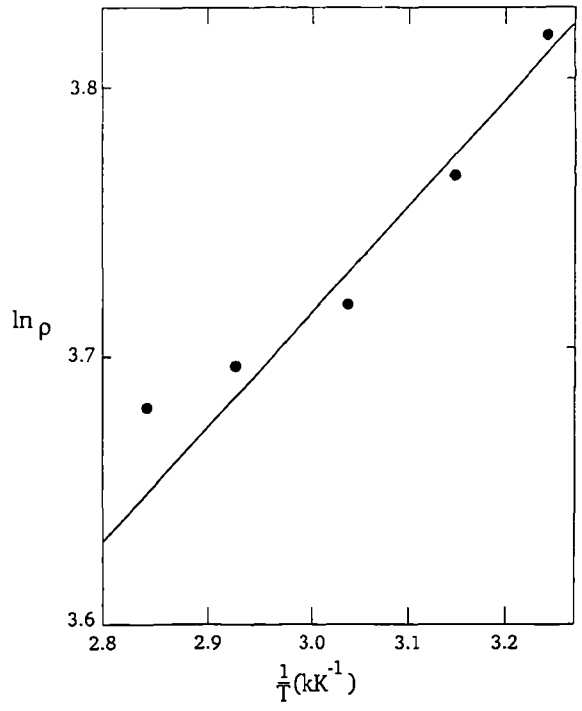

Figure 4.33 Arrhenius plot for specimens containing 0.4 at. % Ho annealed for 27 hrs.

In order to examine the effect on the model of variation of the charge carrier concentration from its assumed value of $n = 2.67 \times 10^{18}$ cm^{-3}, a number of points from the (ρ_{max}, T_{max}) map for the 0.1 at. % Ho specimens were recalculated using values of $n = 2 \times 10^{18}$ cm^{-3} and $n = 3.6 \times 10^{18}$ cm^{-3}, while keeping all the other parameters constant. These points have been superimposed on fig. 4.34, and demonstrate that variations in n exert little influence on the positions of curves of constant E_A in this model, but result in fairly substantial changes in the positions of curves of constant N_{A0}. Thus variations in n from the assumed value would be expected to introduce little additional error into estimates of E_A derived using this model; a significant systematic error could, however, be introduced into estimates of N_{A0}.

4.4 Discussion

It was earlier stated that Daniels et al. suggested that total metal vacancy compensation of the conduction band electrons takes place at 1220°C. An insulating layer, rich in Ba vacancies, would, therefore, be expected to diffuse inwards from the grain surface towards the centre of the grain during the process of annealing in air at 1220°C. Later work by Al-Allak et al. [6] proposed the existence of a resistive layer in series with the space charge layer, introduced during the annealing process.

The establishment of the mechanism responsible for the increase in ρ_{min} during annealing, i.e. whether it is caused by the development of the potential barrier alone, according to Heywang's original model

[1], or whether there exists in addition a series resistive layer as proposed by Daniels [4], requires the consideration of the effects of oxidation and reduction of the ceramic specimens (Section 4.3.3). Throughout this discussion, the assumption is made that the changes in resistivity were a grain boundary effect and that the grain bulk was virtually unaffected by the processing. Although dielectric investigations to confirm this could not be carried out on the specimens used in this instance, dielectric measurements used in other studies (Chapter 3) [6] have shown conclusively that the PTCR effect is exclusively a grain boundary effect; the assumption is therefore considered to be well-founded.

According to the Heywang model the observed diminution or disappearance of the PTCR effect and the decrease in the value of ρ_{min} following reduction in N_2 (fig. 4.24), is caused by the removal of the acceptors, thought to consist of adsorbed oxygen, from the grain boundaries. It would accordingly be expected that following reoxidation for 3 hours in air at 1220°C, the ρ-T plots measured from the specimens would be similar to those of as-made specimens annealed in air for 3 hours at 1220°C immediately following sintering (figs. 4.12, 4.13). The results in fig. 4.25 are not in agreement with this; it is seen instead that the ρ-T curves derived after the reoxidation treatment more closely resemble the original plots obtained from the specimens prior to the reduction treatment (figs. 4.17, 4.18) with respect to the values of ρ_{min}. This proved to be the case for all the Ho concentrations employed.

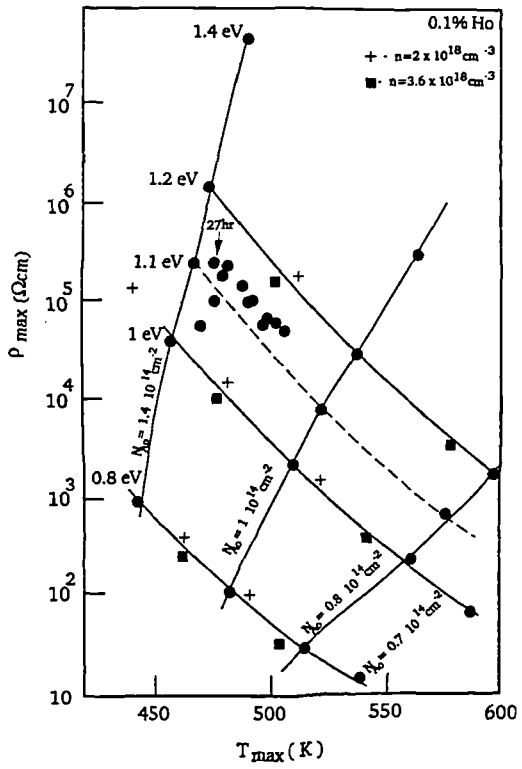

Figure 4.34 Ihrig-Puschert plot of ρ_{max} against T_{max} for specimens containing 0.1 at. % Ho.

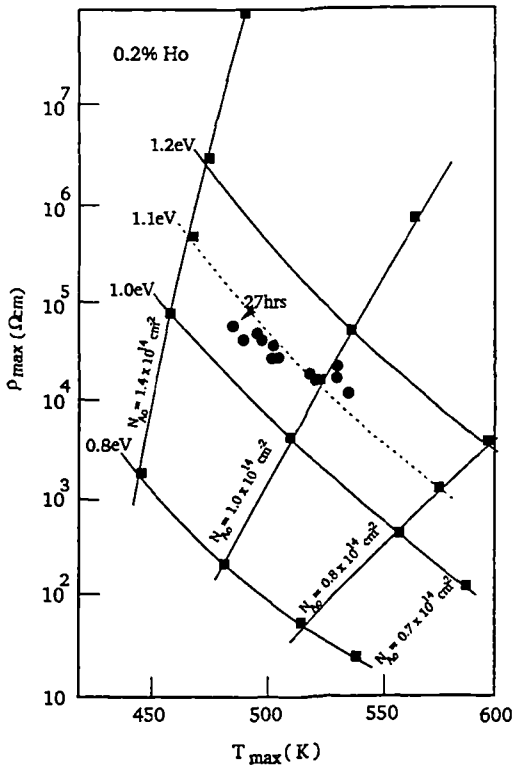

Figure 4.35 Ihrig-Puschert plot of ρ_{max} against T_{max} for specimens containing 0.2 at. % Ho.

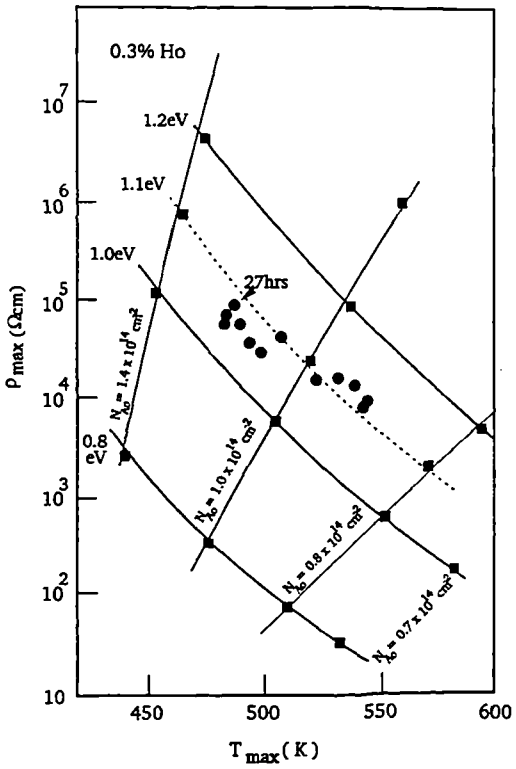

Figure 4.36 Ihrig-Puschert plot of ρ_{max} against T_{max} for specimens containing 0.3 at. % Ho.

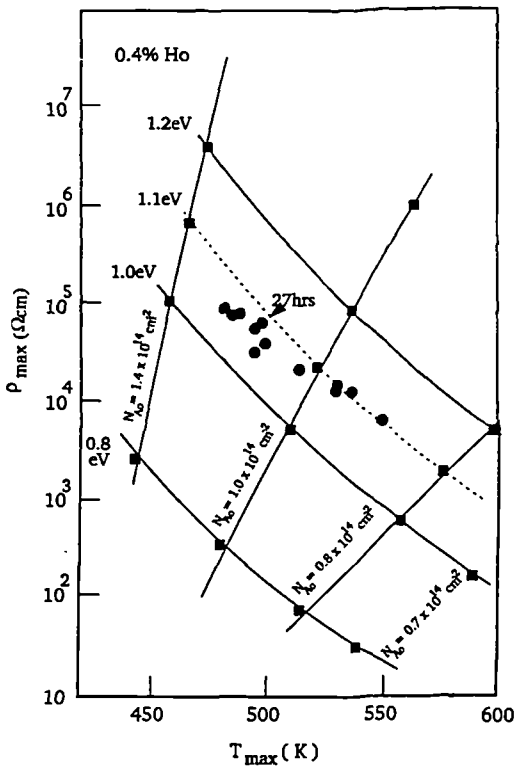

Figure 4.37 Ihrig-Puschert plot of ρ_{max} against T_{max} for specimens containing 0.4 at. % Ho.

An alternative explanation according to the theory of Daniels [4] would attribute the results to a reduction in the Ba vacancy concentration at lower oxygen partial pressure, Po_2. Again the implication is that the ρ-T plots obtained after reoxidation for 3 hours in air should resemble those of newly-manufactured samples annealed for 3 hours, contrary to the experimental observations. It is furthermore extremely unlikely that the boundary region which is rich in Ba vacancies could diffuse completely out of the grains in the timescale of the anneal as would be required to account for the virtually complete suppression of the PTCR effect observed with the 0.3 and 0.4 at. % Ho specimens. This is because of the low diffusion coefficient of the Ba vacancies [9], which have been shown by Al-Allak [6] not to diffuse throughout the grain interiors even after prolonged annealing, and also because the reduction process occupied a much shorter time (3 hours) than the air annealing (27 hours). Thus the effects of reduction and reoxidation are clearly not solely attributable to changes in the concentration of acceptor states.

It is therefore necessary, in order to explain the reduction in ρ_{min} and the diminution of the PTCR effect after reduction in N_2, to extend Daniels' model to include the formation of oxygen vacancies (which are ionised at room temperature) in the Ba vacancy rich region at the grain boundary during reduction. This modification appears to be reasonable since the presence of excess Ba vacancies is thought to promote the formation of oxygen vacancies [10] by the operation of the mass action

law [6] (see Section 4.4.1). The excess of Ba vacancies is assumed to exist throughout the annealing period in N_2 and is believed to arise from the fact that this equilibrium concentration (achieved during annealing in air at 1220°C) did not decrease during the 3 hour reduction treatment in N_2 to re-establish the equilibrium at the lower value corresponding to lower oxygen partial pressure, as predicted by Daniels and Hardtl [11]. Any increased vacancy concentration within the conductive bulk of the grains is likely to be negligible because the bulk is deficient in Ba vacancies, which are confined to the grain boundaries.

4.4.1 Summary of the Revised Grain Boundary Defect Model

In order to explain satisfactorily the results of the annealing investigation, an extension to the original model of Daniels, Hardtl and Wernicke [4] is proposed.

The original model by Daniels et al. proposed that the acceptors at the grain boundary layer consist of Ba vacancies forming a three-dimensional zone which extends inside the grains. These Ba vacancies were assumed to diffuse in from the grain boundaries as their equilibrium concentration increased as the temperature fell during cooling. Total vacancy compensation was believed to occur at about 1220°C in air. At practical cooling rates these vacancies are thought to diffuse to a distance of 1 to 3 μm from the grain surface until they are frozen-in at about 1000°C : this leaves the inside of the grain conductive. A schematic profile of the concentrations of the defects relevant to the PTCR effect in a single grain of Ho doped $BaTiO_3$ is

shown in fig. 4.38. According to this model [4], therefore, an insulating (i.e. high resistance) layer of barium vacancies exists in the vicinity of the grain boundaries, and the space charge layer exists between the inner boundary of the barium vacancy layer and the conductive interior of the grain.

This model is then extended by including the formation of oxygen vacancies, mainly in the grain boundary region, during the reduction treatment. These oxygen vacancies coexist with the Ba vacancies and become ionised at room temperature, compensating for the reduction in conduction electrons caused by the Ba vacancies and counteracting the effects of the space charge and insulating layer. This is illustrated schematically in fig. 4.39.

The presence of the barium vacancies is also believed to enhance the formation of oxygen vacancies at the grain boundaries during reduction. Wernicke [9] suggested a reaction scheme relating the vacancies to the Ti-rich intergranular phase (resulting from the addition of excess TiO_2 prior to sintering) which can be summarised by the equation

$$BaTi_3O_7 + 2Ba_{(lattice)} + 2O_{(lattice)} \rightleftharpoons 3BaTiO_3 + 2V_{Ba} + 2V_o \quad (4.1)$$

This reaction implies a mass-action law of the form

$$[V_{Ba}]\,[V_o] = K_S \quad (4.2)$$

Although the concentration of barium vacancies at the grain boundaries increases with falling temperature during cooling, the concentration does not reach its equilibrium value before the defects are frozen-in because of the low diffusion coefficient of the barium vacancies. According to the mass-action law, therefore, a corresponding increase in oxygen vacancy concentration is favoured in order to restore the overall equilibrium.

A reoxidation treatment rapidly destroys the oxygen vacancies because of the high mobility of oxygen ions in the lattice, thus restoring the original situation (fig. 4.38).

4.4.2 Consequences of the Revised Model

An important consequence of this revised model is that oxygen vacancy formation would be expected to proceed preferentially, since the diffusion coefficient of oxygen vacancies in $BaTiO_3$ exceeds that of the barium vacancies by several orders of magnitude [9]. Both oxygen and barium vacancies are therefore believed to be present in the reduced ceramics. The additional conduction band electrons available from the oxygen vacancies give rise to a decrease in ρ_{min} and a reduction in the height of the grain boundary potential barrier, diminishing or suppressing the PTCR effect. Upon reoxidation in air, the concentration of the oxygen vacancies at the grain boundaries fall very rapidly because of their high diffusion coefficient, and the dominant effect of the barium vacancies, acting as acceptors, is restored. The PTCR effect is consequently restored and the resulting characteristics are therefore

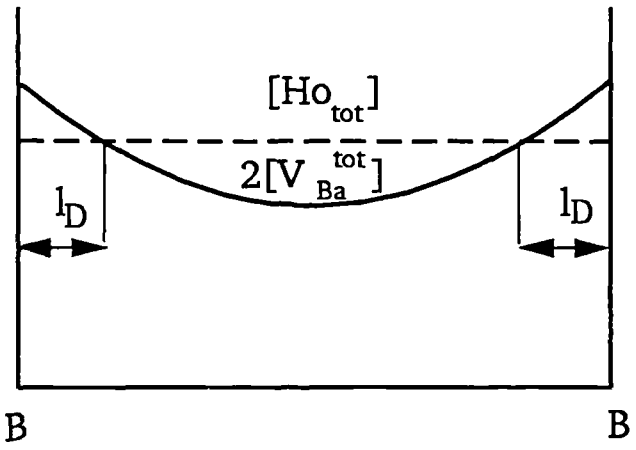

Figure 4.38 Schematic distribution of vacancy concentrations across a single grain.

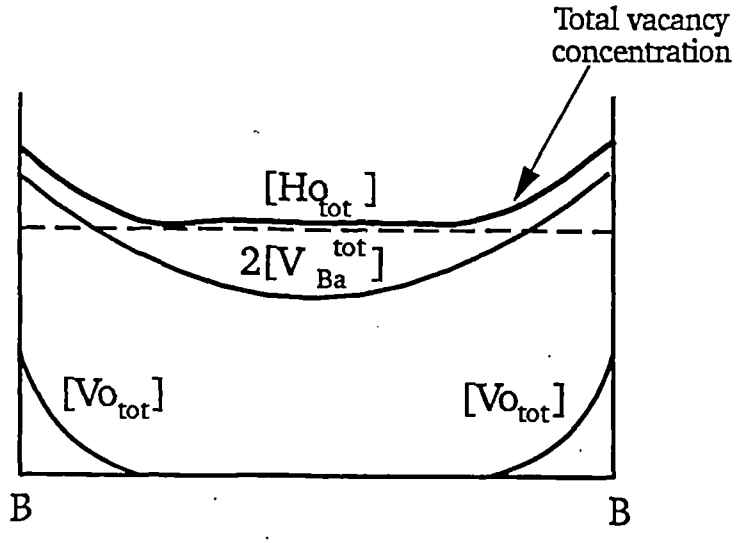

Figure 4.39 Schematic distribution of vacancy concentrations across a single grain after reduction.

expected to resemble the original properties of the specimen before reduction; this prediction is indeed consistent with the experimental observations.

The fact that the length of the annealing time had no noticeable influence upon either the mean size or the distribution of the grains (even after a 27 hour annealing treatment) for any of the donor dopant compositions investigated appears to show that the number of grain boundaries per unit length is not significantly altered by the annealing process. Modifications to the grain structure may therefore be excluded as a possible cause of the observed variations of ρ_{min}. The second phase, rich in Si and Ti, observed in the 0.1 and 0.2 at. % Ho ceramics by means of the SEM, is attributed to the elimination of the SiO_2 and excess TiO_2, added as sintering aids to the precursor mixture, from the specimen during the sintering process. The absence of detectable amounts of the second phase in the finer-grained 0.3 and 0.4 at. % Ho ceramics was considered to be caused by the presence of larger numbers of intergranular interstices into which the material could readily be dispersed evenly without being eliminated onto the surface of the specimen.

The observed increase in activation energy below the transition temperature, derived from the Arrhenius plots, as the annealing time was increased from 4 hours to 27 hours is consistent with enhancement of the potential barrier by the annealing process. The most likely explanation of this enhancement is on the basis of an increase in the

acceptor state density at grain boundaries during annealing, according to Jonker's modification of the Heywang model [3]; the spontaneous polarisation does not completely compensate the potential barriers below the transition temperature, so that the residual potential barriers will be influenced by changes in acceptor state density at grain boundaries which also influence ρ_{max} etc. It is considered likely that such an enhancement of the residual potential barriers could occur simultaneously with the postulated formation of an insulating layer during the annealing process, and that the observed changes in ρ_{min} are due to a combination of the two effects.

The analysis of ρ_{max} and T_{max} at different annealing times by the Ihrig and Puschert technique, reveals a definite trend towards an increase in acceptor density at longer annealing times. This trend was observed for specimens of all the donor dopant concentrations examined and is considered to be significant, although there may, however, be some systematic error in the positions of the loci of constant N_{A0}, as mentioned in Section 4.3.5. It is, therefore, considered that the trends towards the increase in the steepness of the rising parts of the ρ-T plots, the increase in ρ_{max} and the lowering of T_{max} as the length of the annealing time is increased may be satisfactorily explained in terms of the Heywang model as being caused by an increase in the acceptor state density. The applicability of the Heywang model to these observations indicates that at high temperatures (i.e. above the transition temperature) the resistance of the postulated resistive layer

created by the annealing process is likely to be negligible in comparison with the resistance of the space charge layer.

The observation that the (ρ_{max}, T_{max}) values for each ceramic composition lay close to the locus of acceptor energy corresponding to E_A = 1.1 eV indicates that the same acceptor species is present at each donor dopant concentration examined, so that variation of the donor dopant concentration within these limits is unlikely to have changed the compensation mechanism, although the acceptor concentration necessary to achieve compensation will be altered accordingly. Likewise the value of E_A derived from Al-Allak's [6,12] study of the effects of annealing, E_A = 1.12 eV, indicates that the same acceptor species were probably present as in the work discussed here. It may be noted that in Al-Allak's work, an increase in peak resistivity of about 3 orders of magnitude was produced by annealing, compared with about 1 order of magnitude in the present work. The difference is believed to be mainly attributable to the presence of ~ 11 % $CaTiO_3$ in Al-Allak's specimens; the Ca^{2+} ions are believed to substitute for Ba^{2+} ions [13] in the lattice, and although the substitution does not appear to have greatly changed the nature of the acceptor species, as evidenced by the similarity in acceptor energy values E_A, it is considered that such a substantial substitution might have changed the lattice parameters and enhanced the diffusion coefficients of vacancies. At 120°C, $CaTiO_3$ has an orthorhombic crystal structure with lattice parameters a = 5.3670Å, b = 7.6438 Å and c = 5.4439 Å [14], whereas $BaTiO_3$ has a cubic

structure with lattice parameters a = 3.996 Å [15]. Such changes would be expected to exert a significant influence on the peak resistivity, according to the Heywang and Daniels models.

A further aspect of the influence of the reduction process on the PTCR behaviour of the specimens remains to be addressed, namely the fact that the reduction process is far more effective in eliminating the PTCR effect in heavily donor doped ceramics than in the lightly doped specimens (fig. 4.24). This phenomenon may be related to the substantial reduction in grain diameter (table 4.3) from 21 μm to 7.9 μm as the dopant concentration is increased from 0.1 to 0.4 at. % Ho. This reduction in grain diameter is accompanied by a change in specimen microstructure; the morphology changes from flat, closely-packed grains to more rounded, less closely-packed ones, and there is also an increase in the number of intergranular interstices as the grain size diminishes and the number of grains increases. The reduction in grain diameter increases the surface to volume ratio of each grain so that gaseous exchange during the reduction process occurs at a larger effective surface area within each specimen; the large number of interstices and more loosely-packed grains also permit gaseous diffusion to occur more readily. The effectiveness of gaseous exchange at the surface of each grain during reduction would, therefore, be enhanced in the heavily-doped, small-grained specimens and the influence of the process on the PTCR properties correspondingly enhanced. This appears to be a likely

explanation for the effect, but additional work is required to confirm it, such as comparisons using smaller specimens with a larger surface area.

4.5 Conclusions

It has been demonstrated by means of a reduction and reoxidation treatment carried out on samples of varying composition which had been subjected to annealing in air at 1220°C for a lengthy period (27 hours) that an insulating layer caused by the annealing process was present. This layer was predicted by Daniels who postulated that it is rich in Ba vacancies acting as acceptors. The reduction in minimum resistivity and diminution of the PTCR effect observed in the reduced specimens was interpreted in terms of Al-Allak's extension to the Daniels model, which incorporates the formation of oxygen vacancies mainly in the grain boundary region during reduction. The oxygen vacancies coexist with the barium vacancies and become ionised at room temperature, compensating the reduction in the number of conduction electrons caused by the barium vacancies.

It has also been shown that annealing in air at elevated temperatures produces an enhancement of the grain boundary potential barrier by increasing the acceptor state density. This phenomenon is responsible for the observed increase in maximum resistivity and reduction in temperature corresponding to the maximum resistivity observed with increasing annealing time. The observed increase in

minimum resistivity with annealing time is attributed both to the formation of the resistive grain boundary layer and to the enhancement of the potential barrier, with consequent increase in the resistance of the space charge layer. The nature and dimensions of the resistive layer, however, are not yet known and further work is required to elucidate its properties.

References

1. Heywang, W., Solid St. Electron., 3, 51 (1961).
2. Jonker, G. H., Solid St. Electron., 7, 895 (1964).
3. Jonker, G. H., Mat. Res. Bull., 2, 401 (1967).
4. Daniels, J., Hardtl, K. H. and Wernicke, R., Philips Tech. Rev., 38, 73 (1978/9).
5. Daniels, J. and Wernicke, R., Philips Res. Rpts., 31, 344 (1976).
6. Al-Allak, H. M., Russell, G. J. and Woods, J., J. Phys. D., 20, 1645 (1987).
7. Ihrig, H. and Puschert, W., J. Appl. Phys., 48, 3081 (1977).
8. Johnson, C. J., Appl. Phys. Lett., 7, 221 (1965).
9. Wernicke, R., Philips Res. Rpts., 31, 526 (1976).
10. Eror, N. G. and Smyth, D. M., in "The Chemistry of Extended Defects in Non-Metallic Solids", (L. Eyring and M. O'Keefe, eds.), pp62-74, North-Holland (1970).
11. Daniels, J. and Hardtl, K. H., Philips Res. Rpts., 31, 489 (1976).
12. Al-Allak, H. M., Brinkman, A. W., Russell, G. J. and Woods, J., J. Appl. Phys., 63, 4530 (1988).

13. Han, Y. H., Appleby, J. B. and Smyth, D. M., J. Am. Ceram. Soc., 70 [2], 96-100 (1987).

14. Landolt-Börnstein, Numerical Data and Functional Relationships in Science and Technology, New Series, Group III, Vol. 3, p51 (1969).

15. Ibid, p44.

Table 4.2

0.1 at. % Ho

Annealing Time (min)	T_{min} (°C)	ρ_{min} (Ω cm)	ρ_{max} (Ω cm)	T_{max}		ρ_{max}/ρ_{min}
				(°C)	(K)	
30	105	63	58000	235	452	920.6
60	112	101	55000	232	505	544.6
120	70	71	64500	224	497	908.5
180	58	70	71000	225	498	1014.3
240	92	54	76000	229	502	1407.3
360	102	85	108000	217	490	1270.6
540	114	104	163000	215	488	1567.3
720	114	130	108000	218	491	830.8
900	112	162	101000	204	477	623.5
1080	114	106	188000	208	481	1773.6
1260	112	130	238000	204	477	1830.8
1620	112	120	218000	211	484	1817.7

Table 4.2 (Cont/.....)

0.2 at. % Ho

Annealing Time (min)	T_{min} (°C)	ρ_{min} (Ω cm)	ρ_{max} (Ω cm)	T_{max}		ρ_{max}/ρ_{min}
				(°C)	(K)	
30	32/16	14/100	13500	246	519	964.3
60	102	19	10200	260	533	536.8
120	40	13.4	14000	256	529	1044.8
180	62	12.9	15000	244	517	1162.8
240	70	10.8	17200	246	519	1592.6
360	66	13.2	24000	228	501	1818.2
540	52	16	30500	228	501	1906.3
720	91	22	23500	230	503	1068.2
900	94	25.6	36000	224	497	1406.3
1080	64	17	35000	217	490	2058.8
1260	72	17.4	40000	222	495	2298.8
1620	90	21	51000	213	486	2428.6

Table 4.2 (Cont/.....)

0.3 at. % Ho

Annealing Time (min)	T_{min} (°C)	ρ_{min} (Ω cm)	ρ_{max} (Ω cm)	T_{max}		ρ_{max}/ρ_{min}
				(°C)	(K)	
30	60	15	9700	271	544	646.7
60	62	18.9	10900	273	546	576.7
120	78	14	14400	268	541	1028.6
180	85	26	16400	261	534	630.8
240	84	16.6	15700	241	514	945.8
360	71	23.3	29000	229	502	1244.6
540	82	28	40000	236	509	1428.6
720	87	34	33000	224	497	970.6
900	85	38	52000	214	487	1368.4
1080	74	46	52000	220	493	1130.4
1260	91	50	63000	215	488	1260.0
1620	98	66	75000	219	492	1136.4

Table 4.2 (Cont/.....)

0.4 at. % Ho

Annealing Time (min)	T_{min} (°C)	ρ_{min} (Ω cm)	ρ_{max} (Ω cm)	T_{max}		ρ_{max}/ρ_{min}
				(°C)	(K)	
30	56	13.3	6650	278	551	500.0
60	72	14.2	12900	264	537	908.5
120	77	16	14200	258	531	887.5
180	84	19	14900	258	531	784.2
240	78	12.4	21200	243	516	1709.7
360	61	18	32300	224	497	1794.4
540	76	19.8	37000	228	501	1868.7
720	90	24	54500	222	495	2270.8
900	84	30	85000	210	483	2833.3
1080	102	31	75000	213	486	2419.4
1260	100	35	75000	215	488	2142.9
1620	95	40	62000	225	498	1550.0

Table 4.3

Potential barrier heights below the transition temperature, derived from Arrhenius analysis

Composition	ϕ (4 hours annealing) (eV)	ϕ (27 hours annealing) (eV)
0.1 at. % Ho	0.023 $\pm$ 0.005	0.038 $\pm$ 0.008
0.2 at. % Ho	0.019 $\pm$ 0.004	0.025 $\pm$ 0.005
0.3 at. % Ho	0.035 $\pm$ 0.007	0.047 $\pm$ 0.009
0.4 at. % Ho	0.031 $\pm$ 0.006	0.037 $\pm$ 0.007

CHAPTER 5

GRAIN BOUNDARY OBSERVATIONS

5.1 Introduction

In the commonly accepted explanation of the PTCR effect, the rapid change in resistivity as the temperature is increased beyond the Curie point, it is assumed that acceptor states are responsible for the existence of grain boundary potential barriers [1,2,3,4,5]. At temperatures below the ferroelectric-paraelectric transition (the ferroelectric Curie point) the potential barriers are compensated by the polarisation of the ferroelectric domains in the grains and the overall resistivity of the ceramic remains low. As the temperature is increased above the Curie point and the material enters the paraelectric phase, the domains disappear removing the means by which the potential barriers are compensated and resulting in the characteristic sharp rise in resistivity.

Since the PTCR behaviour of the material is governed by the characteristics of the potential barriers and compensating ferroelectric domains, it would appear that further information concerning the PTCR mechanism might be elicited by direct examination of the grain boundaries and domains at the microscopic level using appropriate techniques.

The non-centrosymmetric crystal structure of the tetragonal, ferroelectric phase of $BaTiO_3$ results in optically anisotropic behaviour and birefringence. The birefringent behaviour permits ferroelectric domains to be observed under the microscope in polarized light and such techniques have been applied to the study of the ferroelectric

domains in single crystals of $BaTiO_3$ by a number of workers [6, 7, 8, 9, 10, 11]. These methods may be applied to the study of polycrystalline specimens, such as ceramics, provided that specimens thin enough to permit light transmission can be prepared.

Scanning electron microscopy techniques such as electron beam induced current (EBIC) and the related electron barrier voltaic effect (EBVE) are used widely in semiconductor physics for the characterisation of semiconductor materials and devices. The techniques, which measure the current induced in the specimen by the electron-hole pairs produced by the electron beam may be used to image features such as traps, defects, potential barriers, etc. These influence the induced carrier-pair lifetime and produce variations in current that introduce contrast into the image. Scanning electron microscopy techniques of this type are therefore potentially useful for the study of the grain boundary phenomena in PTCR ceramics.

This chapter describes the results of an investigation of ferroelectric domain behaviour and grain boundary phenomena in $BaTiO_3$ PTCR ceramics by means of polarized light microscopy and scanning electron microscopy techniques.

5.2 Experimental Techniques

5.2.1 Polarized Light Microscopy

(a) Specimen Preparation

Ceramic specimens thin enough to permit light transmission were prepared by the departmental workshop from PTCR ceramic pellets by standard metallographic polishing and lapping techniques. The pellets were mounted on Logitech lapping machines and their flat surfaces polished using alumina powder. The faces were polished alternately, using successively finer grades of abrasive down to a particle size of 0.25 μm, until both surfaces had acquired a fine polish and the specimen thickness had been reduced to 30 μm. The thickness of 30 μm was the standard value of specimen thickness for which geological polarized light microscopies are designed, and corresponded to specimens being approximately 1 grain thick. Great caution had to be exercised in the later stages of the lapping process in order to avoid the fracture of the thin polycrystalline specimens; many were destroyed during polishing.

(b) Observation Technique

The lapped specimens were cleaned by repeated washing in 1.1.1-trichloroethane in order to remove traces of the wax used to mount the specimens during polishing; the wax had to be removed to prevent contamination of the microscope objective lens. After cleaning, the specimens were gently positioned at the centre of the circular glass slide of the heated stage; no adhesive or refractive index matching

compound was used, in order to prevent clamping effects influencing the ferroelectric properties of the sample. The thermocouple junction was then positioned in contact with the glass adjacent to the specimen, ensuring that it did not come into contact with the microscope objective lens.

Each specimen was examined at x300 magnification at room temperature in unpolarized light with the polarizing elements absent from the optical path, then in polarized light with the polarizing elements positioned such that the plane of polarization of the upper element was at 90° to that of the lower element (i.e. the "crossed polarizers" condition). The specimen was rotated using the microscope turntable so as to vary the plane of polarization of the incident light relative to the specimen. Photomicrographs of the specimen under the different illumination conditions were taken using a Reichert camera which was positioned over the microscope eyepiece; exposure times were determined by the exposure bracketing technique.

The specimen under investigation was then slowly heated above the ferroelectric transition temperature by passing a d.c. current through the heater element of the hot stage. Specimen temperature was measured by means of the adjacent thermocouple in conjunction with a Digitron digital thermometer; the temperature was not permitted to exceed ~ 175°C (which was sufficiently high for the investigation) in order to prevent thermal damage to the objective lens, < 1 mm from the specimen. The behaviour of the specimen was observed during the

heating process, and adjustments made to its position and to the focus setting made as required in order to maintain the specimen position in the optical field.

After the temperature had stablilized, the specimen under investigation was examined at different angular orientations in polarized and unpolarized light, as at room temperature, and likewise recorded in photomicrographs.

(c) **Investigation of Influence of Electric Fields**

In order to permit the study of the effects of applied external electric fields on the optical properties of the materials, suitable optical specimens were selected and metallic silver electrodes thermally evaporated onto their upper surfaces. The electrodes were circular of diameter 1 mm with centres 2 mm apart, giving an electrode separation of 1 mm at the closest point; the electrode thickness was approximately 2000Å. The specimens were mounted on ordinary glass microscope slides using silver dag conductive paint at the specimen edges for adhesion; thin enamel insulated wires with the insulation removed at the ends, were then attached to the silver contacts using conductive paint to allow electrical contact to be made more easily. The mounted specimens were then placed on the microscope turntable, with the hot stage removed, and connected via the wires to a high voltage d.c. power supply. The specimens were then observed in polarized light between crossed polarizers, as the applied voltage was gradually increased from zero to a maximum value of ~ 300 V, and variations in

the optical behaviour of the specimens recorded. Photographic recording of the high-voltage behaviour proved impossible, since the thin specimens fractured after a few seconds at high voltage.

5.2.2 Electron Microscopy

(a) **EBIC**

Specimens in which the donor dopant was 0.23 at. % La (batch UIB130) and 0.2 at. % Ho (batch HDH15) were selected for EBIC investigation; the specimens of both compositions had been sintered at 1420°C for 30 min followed by annealing at 1220°C for 30 min according to the standard firing profile shown in fig. 2.1. The EBIC studies were carried out according to the procedure described in Section 2.3.2.1. Specimens of thickness ~ 30 μm and 2 mm were prepared using the standard metallographic technique described in section 5.2.1 (a), and the thicker specimens were etched in 5% HF:10% HCl solution in order to reveal surface features. A Schottky electrode consisting of a 200 Å layer of Au, and an ohmic electrode consisting of a 2000 Å Ti layer covered by a protective Au layer, were deposited on opposite faces of each specimen by thermal evaporation. The specimens were then mounted on the heated stage in the SEM and connected to the EBIC electrical circuit, as shown in fig. 2.3. With the Schottky junction reverse biased, attempts were made to obtain images of the specimens in EBIC mode at temperatures below and above the PTC transition temperature.

(b) **EBVE**

Initial preparation of ceramic specimens for investigation by the EBVE technique was carried out using the same metallographical polishing and etching technique adopted for the EBIC specimens. Only one surface of each pellet was thus treated since electrodes were only to be applied to this face; the final thickness of the polished pellets was ~ 2 mm. After cleaning with acetone, ohmic electrodes were then deposited on the polished and etched surface of each specimen by thermal evaporation; the electrodes consisted of a layer of titanium 2000 Å thick, protected from atmospheric oxidation by a superimposed layer of gold, also 2000 Å thick. The electrodes were circular and of diameter 1 mm with the centres 2 mm apart.

The specimen under investigation was mounted on the heater block as shown in fig. 2.4. Thin gold wires attached to binding posts on the stage were used to establish electrical contact with the electrodes, contact being maintained by mechanical pressure. The tip of the thermocouple was positioned in contact with the mica sheet as close as possible to the specimen, to obtain as accurate an indication of the specimen temperature as possible.

The heater block was mounted on the microscope stage and positioned in the microscope column. The electrical circuit used to generate the EBVE image is illustrated in fig. 2.4 and described in Chapter 2.

The area of the specimen to be investigated, i.e. between the electrodes was located using the microscope in secondary electron

emission mode. The SEM was then switched to EBVE mode, and bias applied to the electrodes to form an EBVE image. Initial adjustments were made with the SEM in line scan mode, before the instrument was switched to raster scan operation for the final detailed adjustment. Any features of interest in the EBVE image were photographically recorded.

The specimen was then slowly heated, at a rate not exceeding 1.5-2°C/min until its temperature exceeded the transition temperature. After allowing the temperature to stabilise, EBVE images of the specimen were formed and recorded as described earlier.

5.3 Results

5.3.1 Polarized Light Microscopy

(a) **Orientation Effects**

(i) *Doped Specimens*

The effect of specimen orientation relative to the plane of polarization of incident light is illustrated for a doped specimen from batch UIB130 in the optical photomicrographs in figs. 5.1 to 5.11. The photomicrographs were taken at a magnification of x300, and the width of each print represents 300 μm (± 15 μm) on the specimen, as determined using a stage micrometer. The angular position of the specimen in each photograph was recorded from the angular scale of the microscope turntable, i.e. with respect to an arbitrary origin : the plane of incident light polarization was upwards in these photographs. Although figs. 5.1-5.11 illustrate a single specimen, the observed

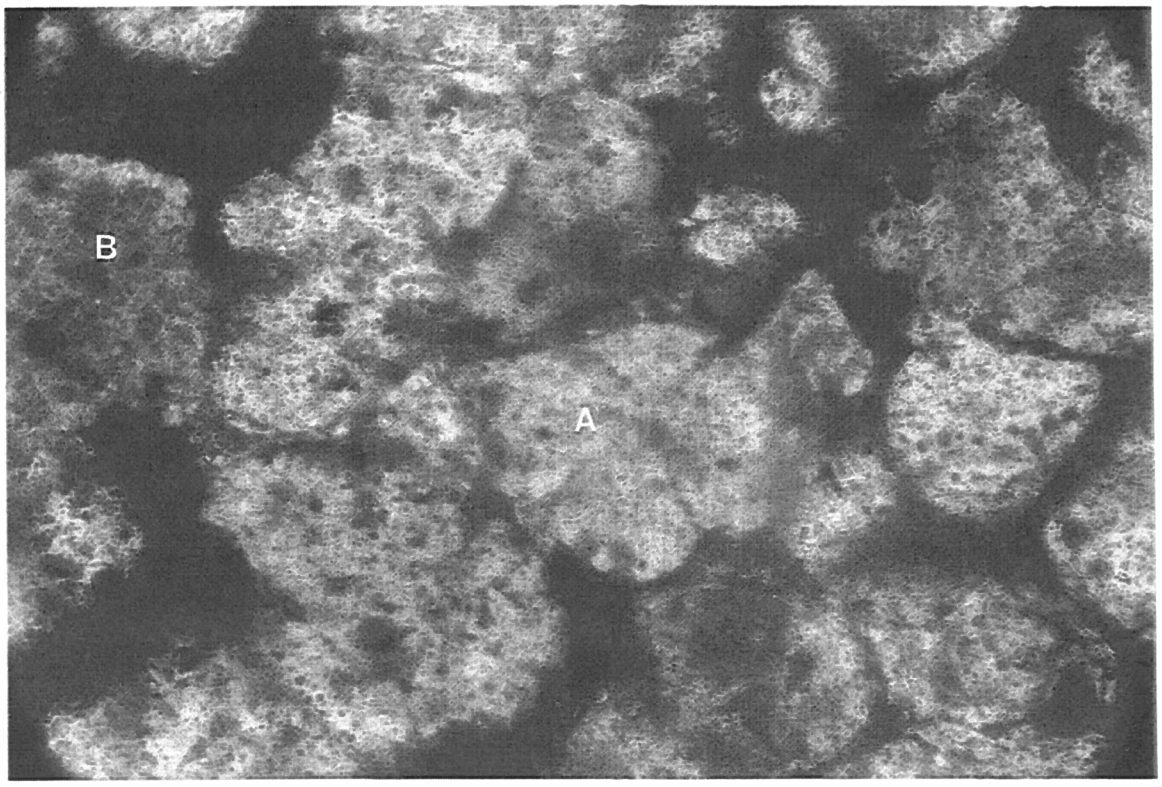

30 µm

Figure 5.1 Polarized light micrograph of a UIB 130 specimen. Angular position $\theta = 0°$.

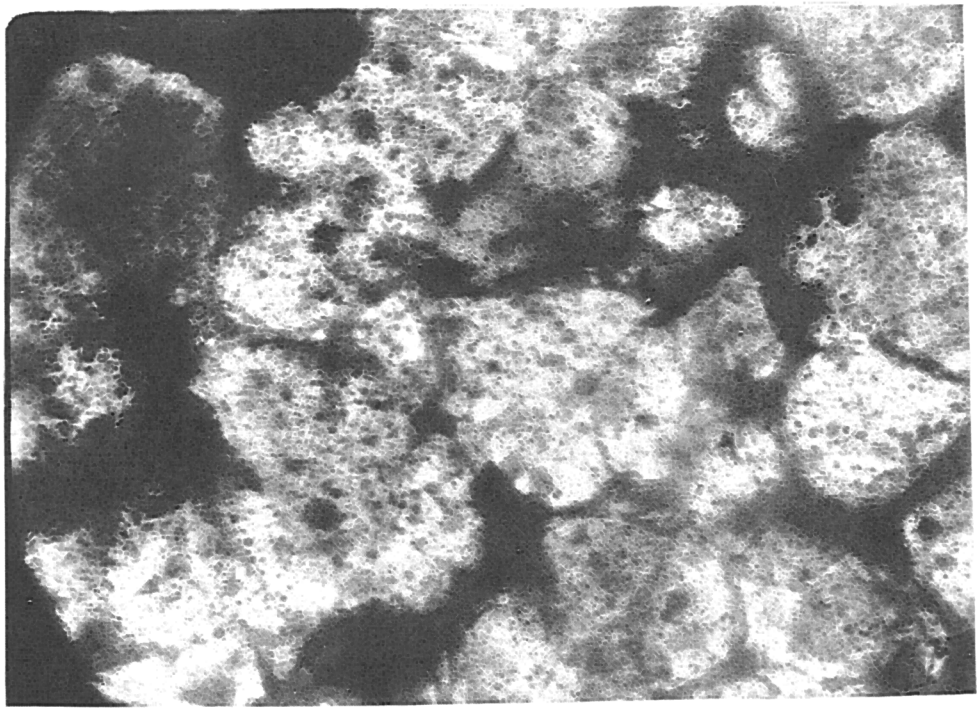

30 µm

Figure 5.2 Polarized light micrograph of a UIB 130 specimen. Angular position $\theta = 10°$.

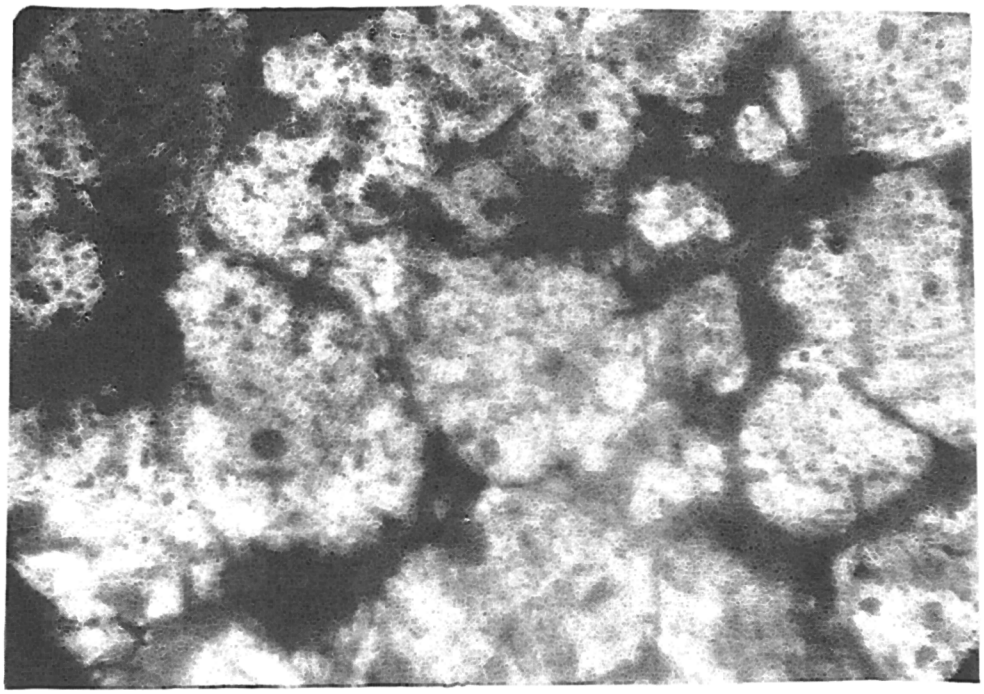

30 μm

Figure 5.3 Polarized light micrograph of a UIB 130 specimen. Angular position θ = 20°.

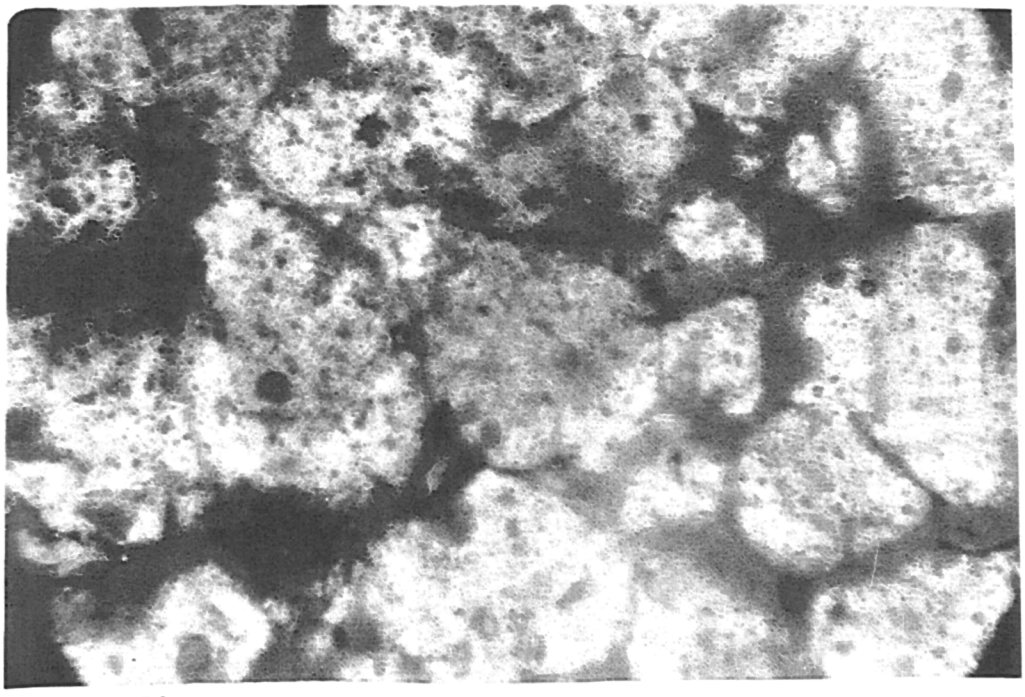

30 μm

Figure 5.4 Polarized light micrograph of a UIB 130 specimen. Angular position θ = 30°.

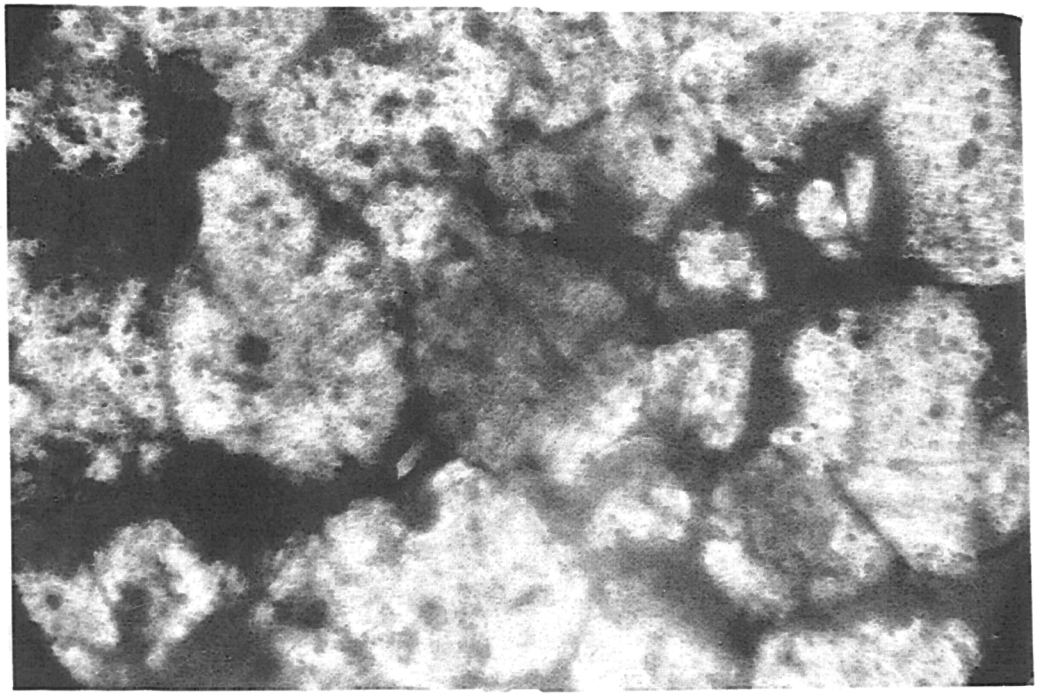

30 μm

Figure 5.5 Polarized light micrograph of a UIB 130 specimen. Angular position $\theta \approx 40°$.

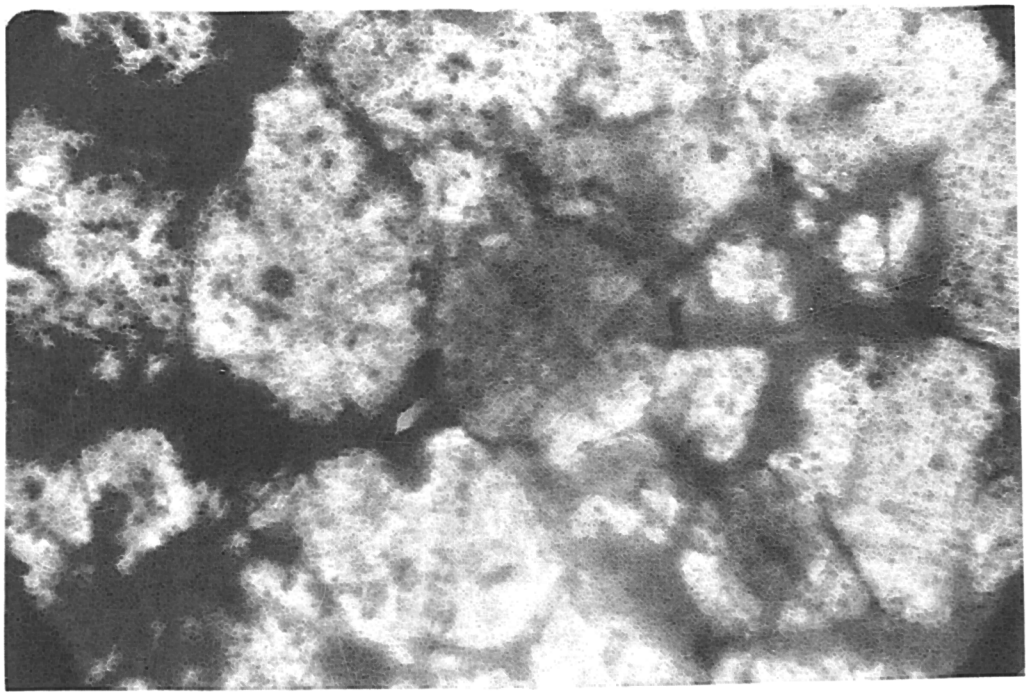

30 μm

Figure 5.6 Polarized light micrograph of a UIB 130 specimen. Angular position $\theta = 50°$.

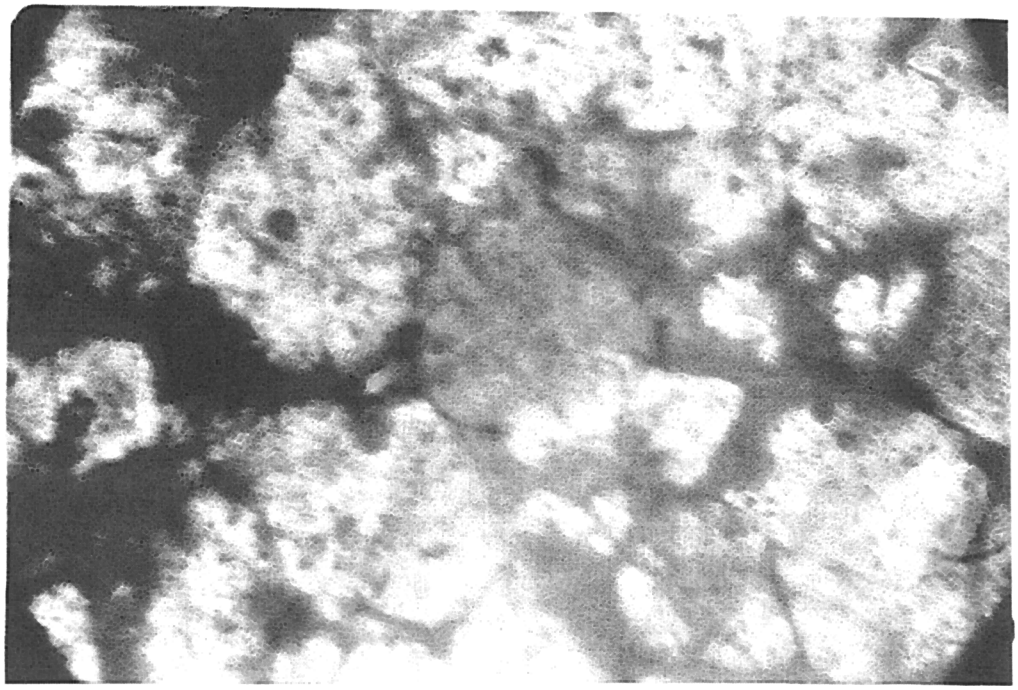

30 µm

Figure 5.7 Polarized light micrograph of a UIB 130 specimen. Angular position $\theta = 60°$.

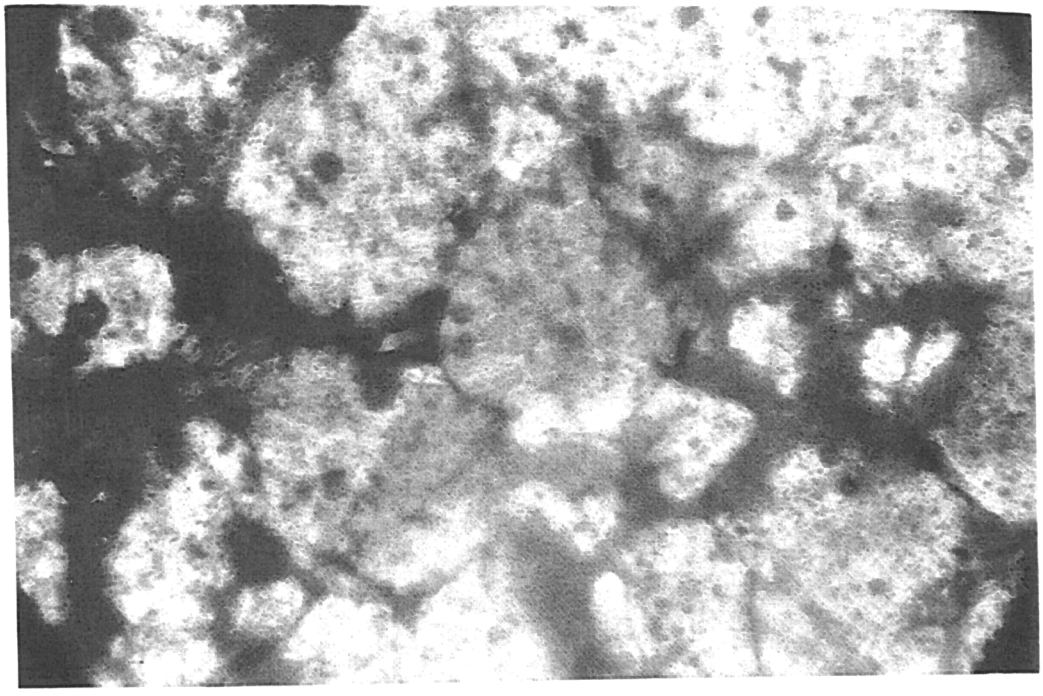

30 µm

Figure 5.8 Polarized light micrograph of a UIB 130 specimen. Angular position $\theta = 70°$.

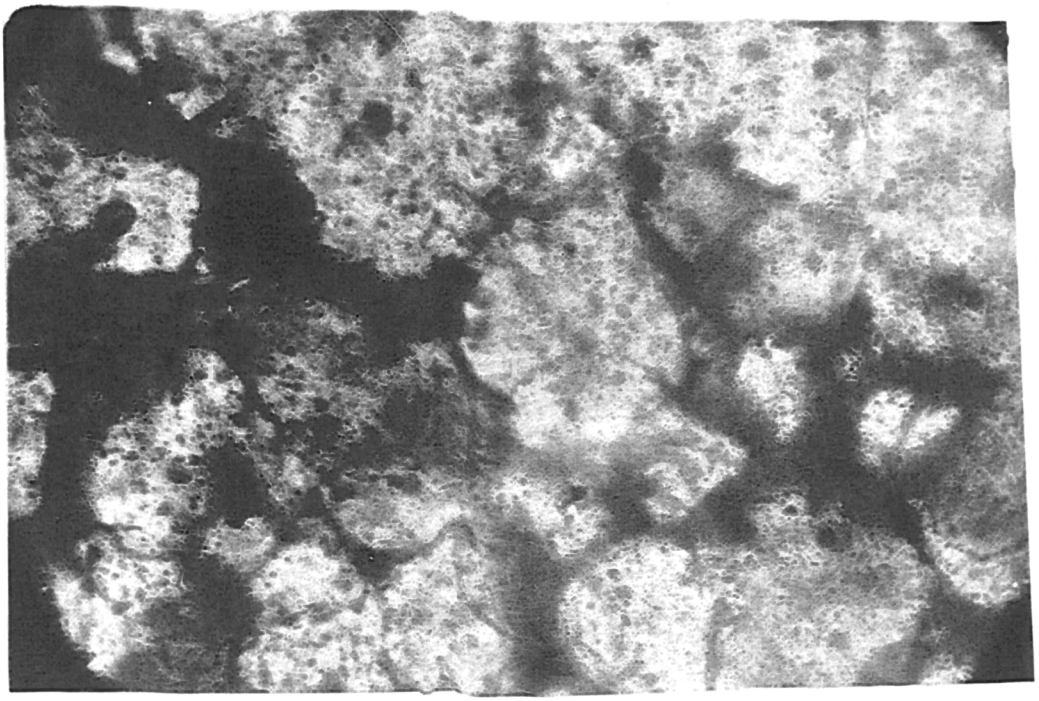

30 µm

Figure 5.9 Polarized light micrograph of a UIB 130 specimen. Angular position $\theta = 80°$.

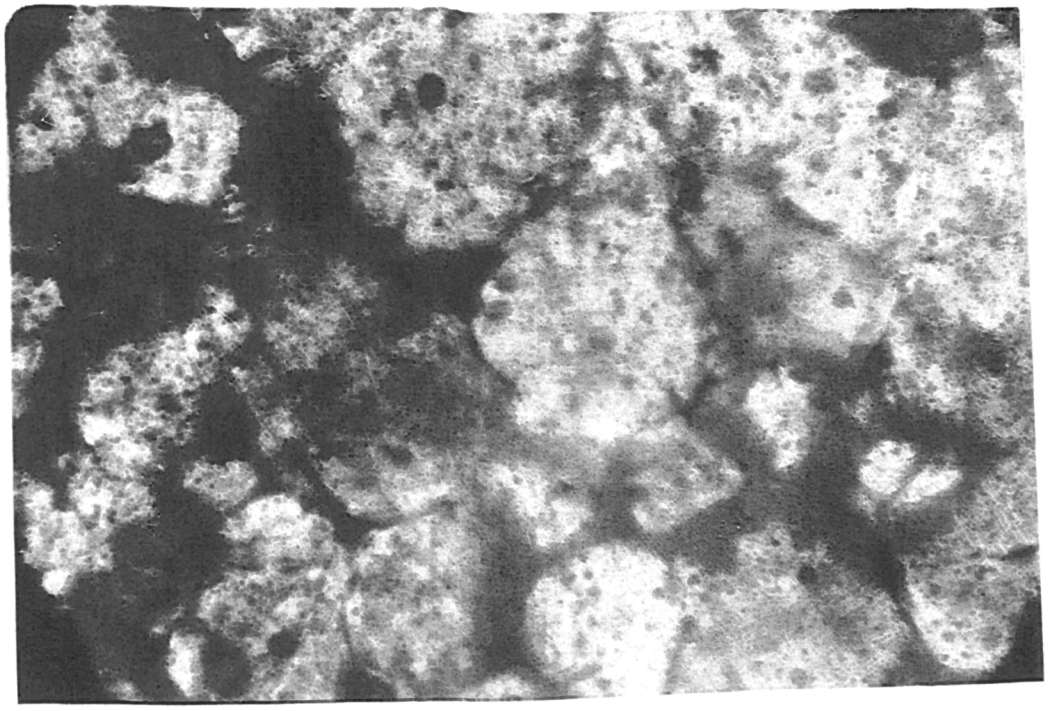

30 µm

Figure 5.10 Polarized light micrograph of a UIB 130 specimen. Angular position $\theta = 90°$.

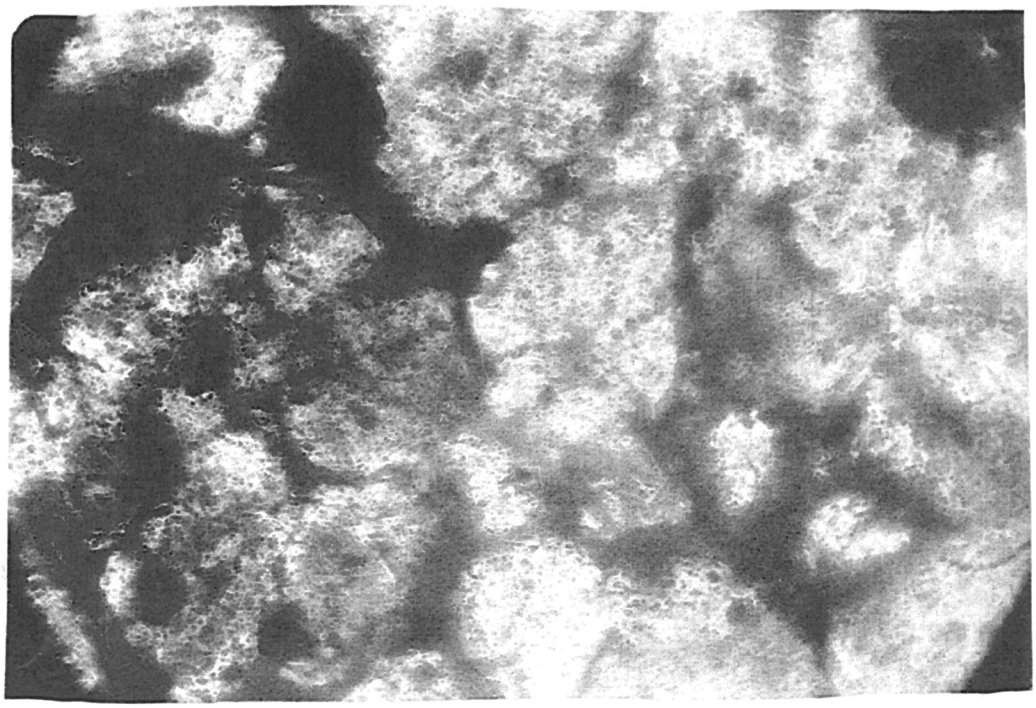

30 μm

Figure 5.11 Polarized light micrograph of a UIB 130 specimen. Angular position θ = 100°.

behaviour was typical of the other specimens from the same batch which were also investigated. The mean grain diameter was 30 μm ± 3 μm derived from a scanning electron micrograph of an unpolished specimen, verified by comparison with polished and etched specimens.

Intergranular boundaries in the specimen were observed to take two forms. In the first case, where grains at triple boundaries had been sheared away by the polishing process, the boundaries between remaining grains occurred in the form of dark fissures up to about 10 μm in width. Where, however, the polishing process bisected a boundary between two touching adjacent grains, the boundary appeared as a difference in contrast between parts of what seemed to be a single large grain; the boundary was much less pronounced in this case.

In several grains, numerous parallel linear features were observed, of width ~ 2 μm and extending in length across the entire extent of the grain. These features are particularly pronounced in grain B in fig. 5.1-5.11.

Examination of grain A, the central grain in figs. 5.1-5.11, revealed the effect of rotation of specimen orientation in polarized light on the properties of a typical grain. The photographs were taken at angular intervals of 10°; it was observed that as the orientation was changed from 0° (fig. 5.1) the light transmission of the grain gradually reduced, being extinguished at 50° (fig. 5.5) and gradually increasing again as the angular orientation moved beyond 50° (figs. 5.5-5.11). It was observed that the positions at which maximum and minimum light transmission occurred were separated by 90° and also that the sequence of events was repeated upon passage through a further 180°. Similar behaviour was observed in the case of numerous other grains in the specimen. Although the intensity of the transmitted light varied with angular rotation the colour of these grains was unaffected by the angular position: each grain displaying the optical extinction phenomenon was of a different colour, unrelated to the colours of adjacent grains.

Other grains however did not show complete optical extinction during angular rotation: the transmitted light intensity varied between maximum and minimum values, but the minimum value did not reach zero. In these grains the variation in transmitted light intensity was

accompanied by changes in colour, traversing the visible spectrum several times in the course of a 360° rotation but reverting to the original colour on returning to the initial angular position. Again the colours of adjacent grains were unrelated.

Slight lateral displacement of the specimen was observed to change the colours of all grains within the field of view.

(ii) *Undoped Specimens*

A scanning electron micrograph of an unpolished pellet of undoped $BaTiO_3$ ceramic is reproduced as fig. 5.12. The mean grain size for this undoped batch was determined as 30 μm $\pm$ 3 μm. An optical micrograph of a polished undoped specimen, observed between crossed polarizers, is shown in fig. 5.13. The overall appearance closely resembled that of the doped specimens.

Linear features similar to those described earlier in the doped specimens were also observed in some of the grains of several doped samples. The undoped ceramic specimens likewise exhibited optical transmission and extinction behaviour during specimen rotation analogous to the behaviour of the doped material. These phenomena were observable by eye, but the optical quality of the undoped specimens was poor, resulting in excessive light scattering and it proved difficult to take useable photographs because of low image contrast (fig. 5.13).

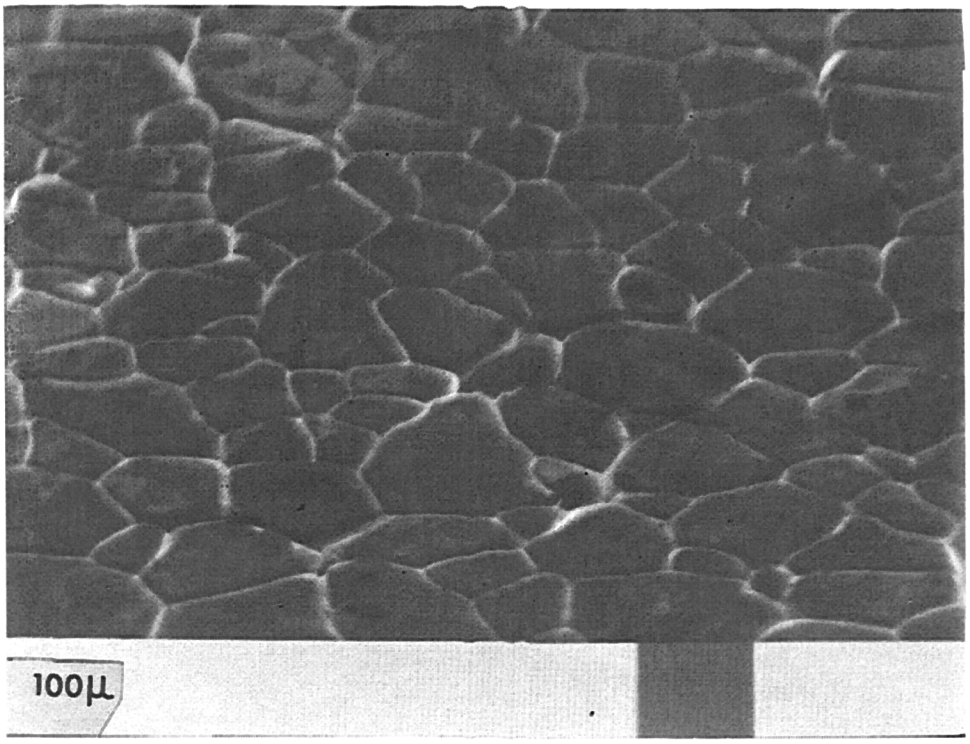

Figure 5.12 SEM micrograph of the as-fired surface of an undoped $BaTiO_3$ specimen.

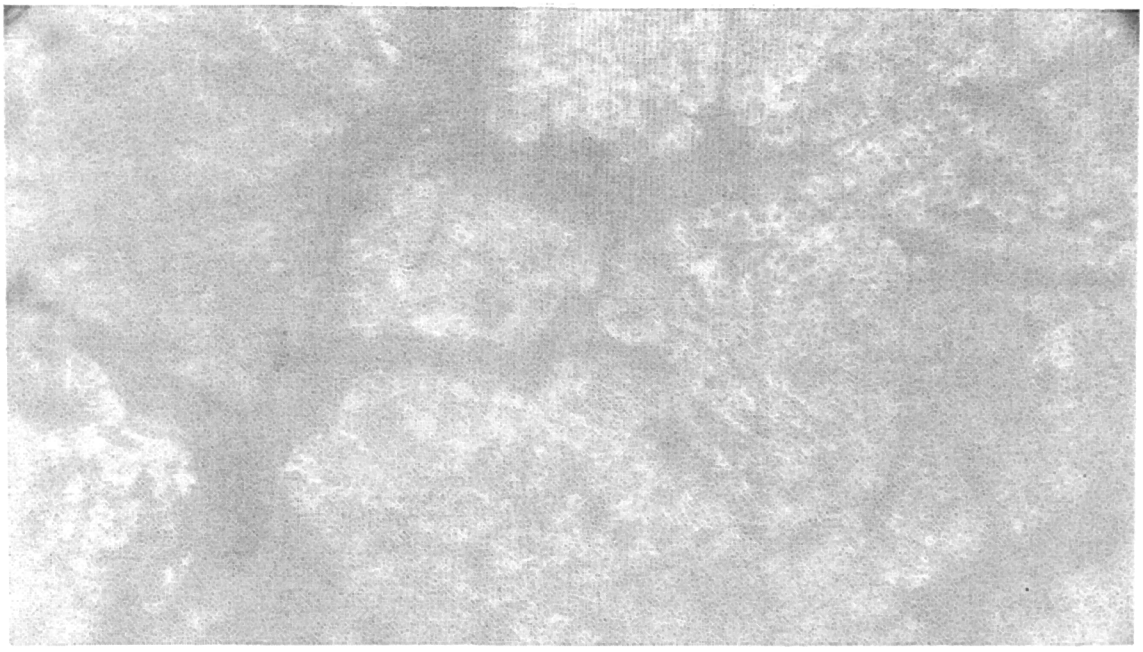

30 μm

Figure 5.13 Polarized light micrograph of an undoped specimen T = 27.4°C.

(b) **Temperature Effects**

Photomicrographs of a UIB130 doped specimen are shown in figs. 5.14-5.16; these were taken in unpolarized light, and between crossed polarizers respectively. These photographs were taken at a temperature of 27.4°C, well below the switching temperature T_C = 130°C for this ceramic composition. Linear features, similar to those previously observed in other specimens, were visible in various grains between crossed polarizers, e.g. the central grain in fig. 5.14. Upon heating the specimen, little visible change was observed until the temperature reached 80°-90°C. The grains then appeared to change colour slowly as the temperature was increased, gradually traversing the optical spectrum until the switching temperature of 130°C was approached. Each grain started from a different initial colour, and some grains were seen to traverse more than one order of the optical spectrum. As T_C was approached, optical extinction occurred at the grain centres, which therefore appeared dark. Different grains exhibited extinction at slightly differing temperatures, so that the phenomena occurred over a temperature range extending 2°-3°C either side of T_C. At temperatures significantly above T_C, the centres of all grains in the specimen were darkened as a result of the extinction process.

Light, however, continued to be transmitted through a thin layer at the boundary of each grain; this layer was about 2-3 μm thick. The phenomenon is illustrated in fig. 5.15, a photomicrograph taken using crossed polarizers at a specimen temperature of 163°C, illustrating the same area of the specimen photographed at room temperature in fig.

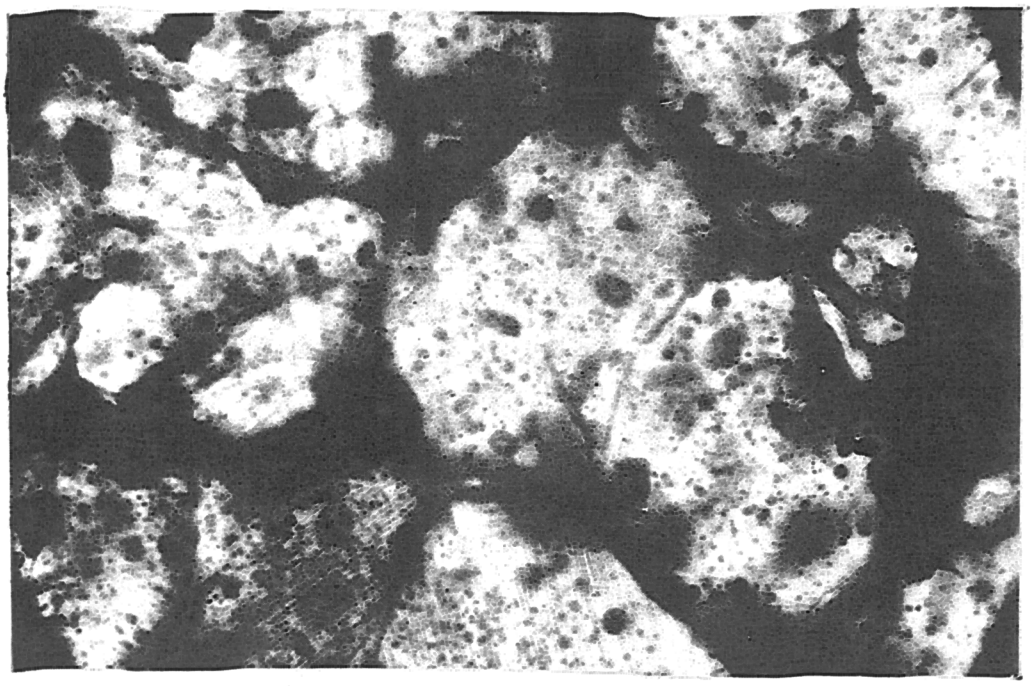

30 µm

Figure 5.14 Polarized light micrograph of a UIB130 sample, T = 27.4°C.

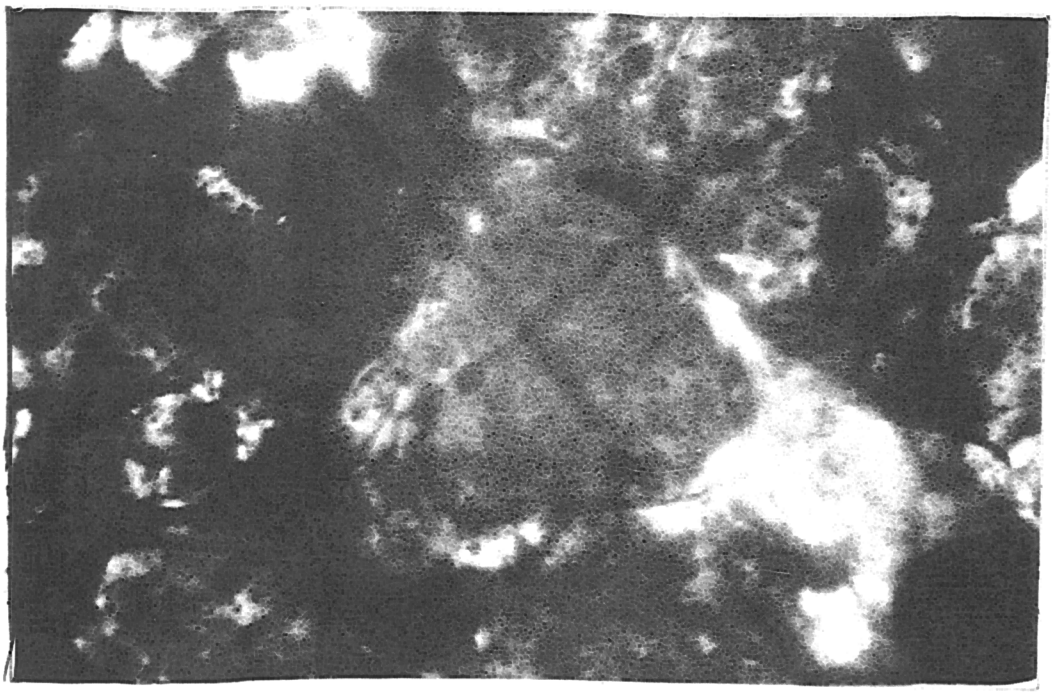

30 µm

Figure 5.15 Polarized light micrograph of the same UIB130 sample, T = 163°C.

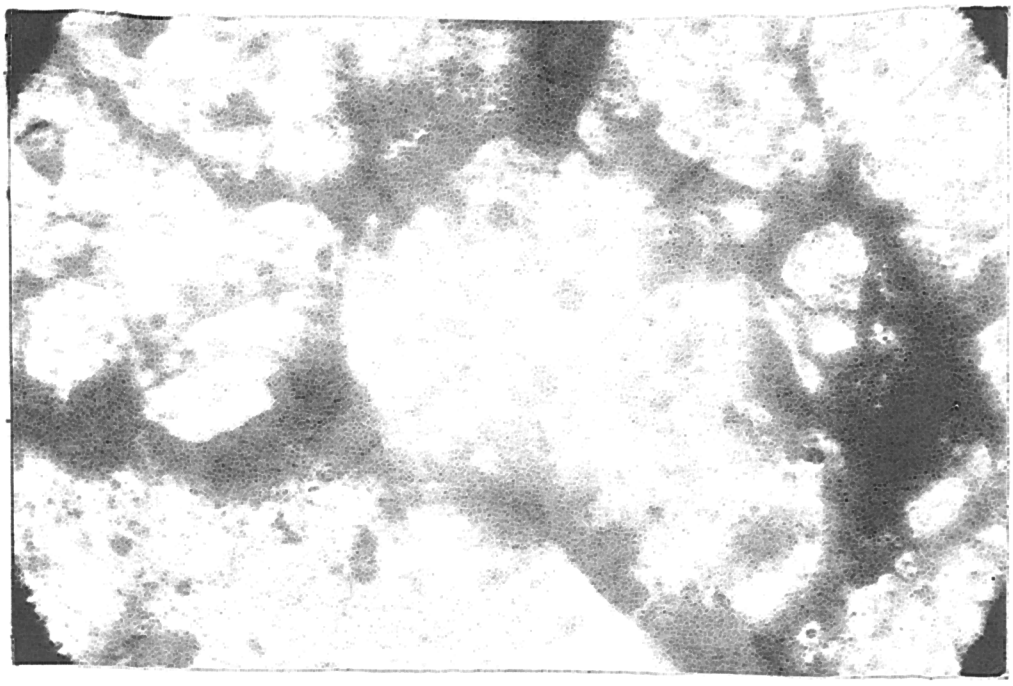

Figure 5.16 Unpolarized light micrograph of the UIB130 sample, T = 163°C.

5.14. The optical transmission at the grain boundaries is best shown by the central grain. Rotation of the microscope stage produced optical transmission along the sections of the grain boundary not transmitting in fig. 5.15; rotation through 90° was seen to extinguish the areas transmitting light in the figure.

Similar behaviour was observed in the case of other specimens from the doped UIB130 batch; the phenomena are believed to be typical.

When undoped specimens were viewed between crossed polarizers (e.g. fig. 5.13) and then heated beyond the switching temperature (in this case the Curie temperature of $BaTiO_3$, 130°C)

the grains behaved in a fashion similar to those in the doped UIB130 material. They were observed to change colour on heating, and optical extinction took place as the switching temperature was reached. In contrast with the doped specimens no light transmission was observed at the grain boundaries above the switching temperature. The optical field thus appeared completely dark and could not be photographed.

(c) **Effects of External Electric Fields**

The application of a voltage to electrodes evaporated onto a UIB130 specimen produced little effect on the optical properties until a value of ~ 300 V was reached. At about this value, a 'wave' of colour changes, followed immediately by optical extinction, travelled from grain to grain across the field of view from the negative to the positive electrode. The process took about 1-2 seconds to complete. When the electric field was switched off, the phenomenon was reversed in a time which appeared instantaneous to the unaided eye, and must therefore have been much shorter than 1 second. These observations were repeated when the experiment was attempted using a number of different specimens.

Maintenance of the applied voltage for longer than about 3-4 seconds resulted in the destruction of the specimen under investigation; the thin specimen shattered into numerous pieces, accompanied by arcing between the residual electrodes. This precluded photography of the specimens, since an exposure time of ~ 16 seconds was required for

photography under these conditions. After several specimens were destroyed in attempts at photography the investigation was discontinued because of the excessive consumption of polished specimens, and the danger to the operator caused by the arcing.

5.3.2 Electron Microscopy

(a) EBIC

Repeated attempts were made to obtain an EBIC signal from various specimens by means of the technique described earlier (Section 5.2.2(a)), but no success was achieved. It was found that short circuits between the rectifying and ohmic contacts were present in most of the thin specimens, rendering them unusable: examination of the specimens under the optical microscope revealed the presence of numerous pinholes in the electrode area. In the remaining specimens the gold electrodes produced insufficient rectification for an EBIC signal to be detectable; specimen junction resistances were found to be in the approximate ratio of 2:1 under reverse and forward bias respectively. It therefore appeared that true Schottky barriers had not been found at the gold electrodes.

(b) EBVE

The initial investigations using this technique were carried out on specimens derived from batch UIB130. At ambient temperature, no electrical activity was detectable by the EBVE techniques in any of the specimens examined; the amplifier output signal was examined for

several lines of the raster image of each specimen by switching the SEM to line scan mode, but the signal was found to consist solely of electrical noise in all cases.

When the specimens were heated to 160°C, well above the transition temperature of ~ 131°C, and a d.c. voltage of 9 V applied between the electrodes, EBVE images showing electrical activity were obtained for a number of specimens. These areas of electrical activity were found to coincide with grain boundaries observed using the SEM in secondary electron emission mode, and to be most prominent at those grain boundaries which were nearly perpendicular to a line joining the electrodes. When the heater current was switched off and the specimen permitted to fall slowly between the transition temperature, the electrical activity was observed to diminish and then disappear as the transition temperature was crossed; this process occurred over the temperature range 140-120°C.

The EBVE images were photographically recorded, together with the corresponding secondary electron emission images of the area under investigation. It was found necessary to disconnect the thermocouple during EBVE photography since the thermocouple lead was found to transmit mains-borne 50 Hz electrical noise into the microscope column. Care was taken to ensure that the sample had reached thermal equilibrium before photography commenced in order to reduce the effects of changes in specimen resistivity, caused by temperature variation, which resulted in drifting of the EBVE bias current during the

exposure with consequent degradation of the image. The EBVE image of some specimens, although visible, could nevertheless not be photographed because of electrical noise and current drift, despite these precautions.

The EBVE image of an UIB130 specimen is shown in fig. 5.17, and the secondary electron emission micrograph of the corresponding area of the same specimen in fig. 5.18. It is evident that the diagonal line of EBVE activity in the centre of fig. 5.17 corresponds to the prominent grain boundary visible in the same position in fig. 5.18. The increased brightness of the image at this position corresponds to an increase in the current passing through the specimen as the grain boundary was irradiated by the electron beam. The horizontal striations visible in fig. 5.17 were caused by the drift of the bias current which caused fluctuations in the image intensity during exposure.

The variation of the EBVE signal generated by this specimen with temperature was also investigated by a different method. The SEM was switched to line scan mode and a raster line near the centre of the display was selected, so that the area of activity would be interrupted by the scan (fig. 5.19). The controls were then adjusted to display the EBVE signal sketched in fig. 5.19, with the specimen temperature at approximately 160°C. This line at the base of the display represented the bias current with electrical noise present, whereas the signal peak near the centre corresponded to the point at which the line scan

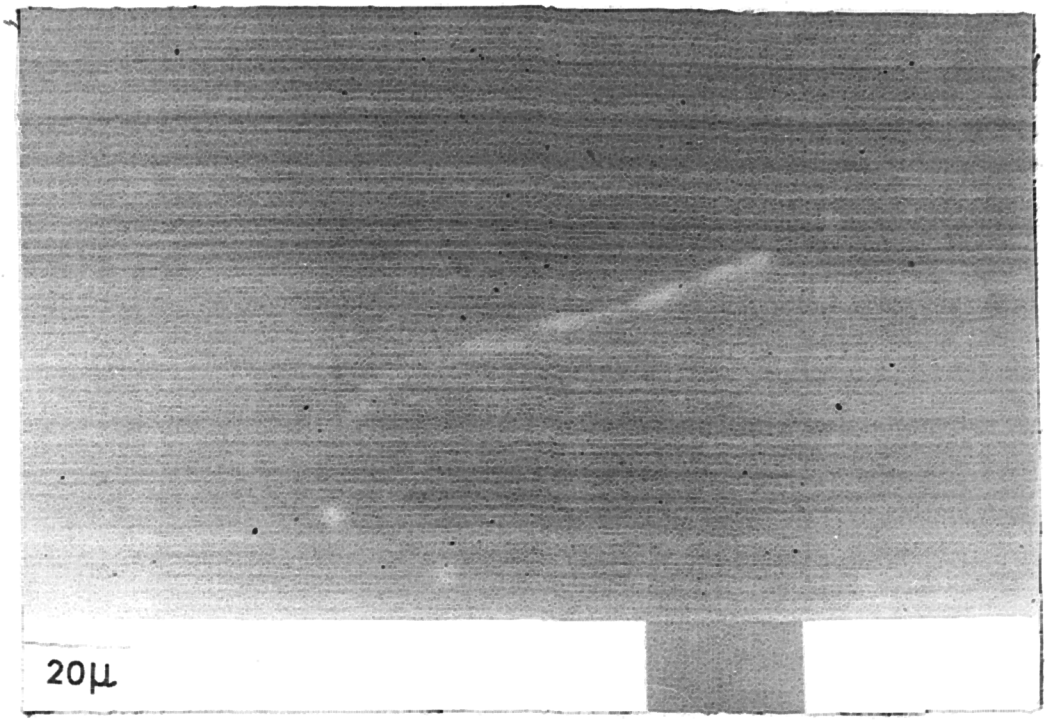

Figure 5.17 EBVE image of UIB130 specimen.

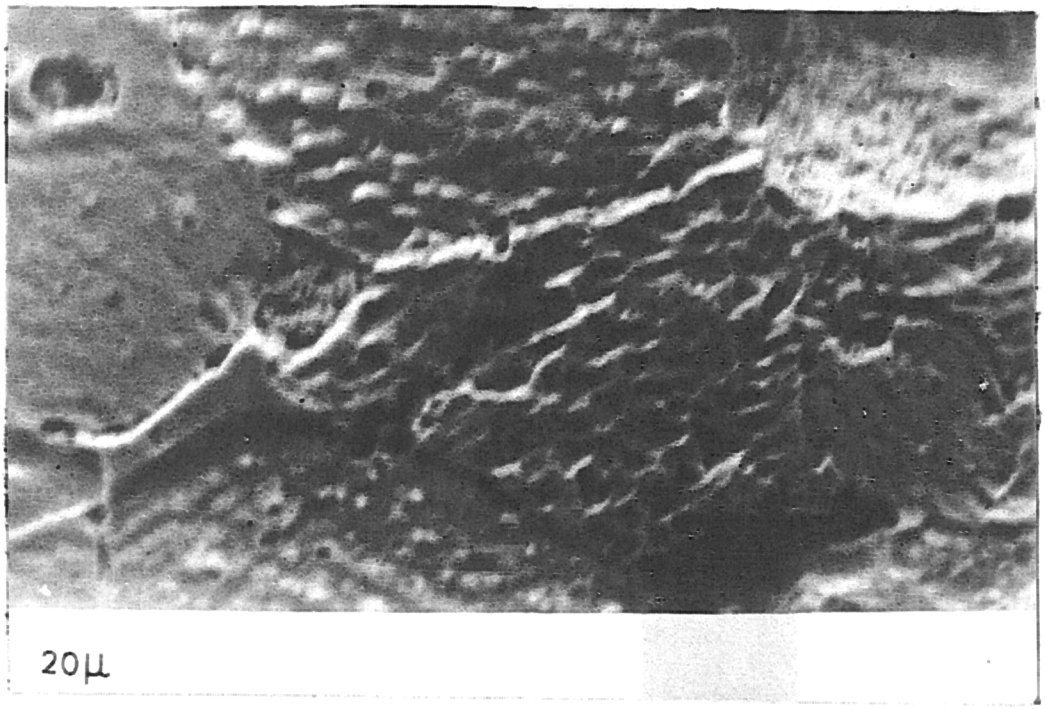

Figure 5.18 Secondary electron mode SEM micrograph of the specimen (UIB130) as in fig. 5.17.

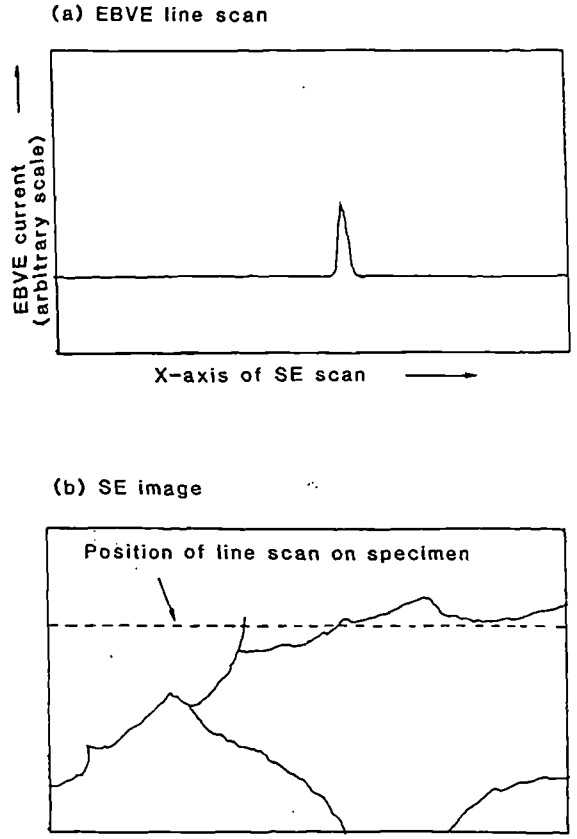

Figure 5.19 Schematic diagram of single line scan EBVE image.

intercepted the potential barrier. With the thermocouple disconnected to reduce electrical noise, the heater current was switched off and the specimen allowed to cool. After an initial small reduction, the bias current was observed to increase steadily as cooling progressed; it was found necessary to adjust the amplifier offset setting repeatedly in order to keep the signal visible on the display. As cooling continued, the central EBVE peak was observed to diminish steadily in height, finally disappearing altogether after about 20 minutes cooling. When this peak had vanished, the thermocouple was reconnected and the temperature measured as 112°C.

Attempts were made to reproduce the EBVE phenomena using two specimens from batch HDH15 which had been polished by hand prior to etching. Some electrical activity was observed at specimen temperatures of about 170°C; however, noise and bias current drift rendered photography impossible. It was also found that the hand polishing process followed by etching had resulted in a coarsely pitted surface on which it was impossible to identify individual grains and grain boundaries for correlation with the electrical activity.

5.4 Discussion

5.4.1 Polarized Light Microscopy

(a) Effects of Specimen Orientation

The alternate optical extinction and transmission behaviour exhibited by grains such as grain A in fig. 5.1 were attributable to the birefringence of the specimen. A detailed explanation and derivation of the conditions for optical transmission and extinction in the polarizing microscope is given in Appendix A3.

The different colours of the individual grains are ascribed to the random orientation of thte optic axes of the grains (the tetragonal c-axes of the crystals) with respect to the optical axis of the microscope, denoted z in fig. A3.1. Equation A3.10 in Appendix A3 shows that optical extinction occurs when

$$2\pi |n_1 - n_2| \frac{l}{\lambda} = p\pi \qquad (5.1)$$

where p is an odd integer , l is the specimen thickness, λ is the wavelength of the incident light in a vacuum, and n_1 and n_2 are the refractive indices for light polarized rerspectively along directions 1 and 2. For given values of n_1, n_2, and l, this condition will be satisfied for a given wavelength λ : light of this wavelength will therefore not be transmitted and the grain will appear to be of the complementary colour when viewed in transmitted light. Variation of the inclination of the optic axis of the grain with respect to the z axis of the microscope results in changes in the values of n_1 and n_2 (equations A3.11-A3.14) and in the corresponding wavelength λ which is not transmitted; the colour of the grains therefore varies from grain to grain.

It is believed that the colour changes observed as a result of lateral motion of the specimens on the stage can also be ascribed to this effect, since movement of the specimen was likely to be accompanied by small angular displacements with respect to the microscope z axis.

The discussion of birefringence effects in the polarizing microscope given in Appendix A3 assumes that the specimen thickness corresponded to the dimensions of a single grain, so that each grain was illuminated by plane polarized light. This condition was not however met for all the grains: the random distribution of grains within the polished specimens ensured that not all the grains observed from

the upper surface of the specimen extended through the entire specimen thickness to be illuminated directly by plane polarized light from the microscope polarizer, but that some would be illuminated through a second layer of grains beneath them. It was therefore possible that some grains would be illuminated by several overlapping, randomly oriented grains in the layer beneath. This would result in the illumination of the upper grain by an elliptically polarized light source, the effect of which would be to prevent complete extinction of transmitted light at any angular position of the specimen, although the light intensity would vary as the specimen rotated on the stage. It would also result in variation in the wavelength of extinguished light, according to equation A3.10, as the specimen was rotated, resulting in changes in the colour of the grain. This behaviour contrasted with the total extinction at 90° intervals and constant grain colour observed under linearly polarized illumination. It is believed that elliptically polarized illumination arising as a result of the passage of light from the microscope polarizer through additional layers of grains was responsible for the incomplete extinction and variable colour observed in some grains. Such effects could be minimised by further reductions in specimen thickness, although at the expense of specimen durability.

The linear features observed in grain B in fig. 5.1 were ferroelectric domains [13,15]. In this instance, the domains appeared to be arranged so that the ferroelectric dipoles in adjacent domains were at right angles to each other (in contrast with the alternative case, also

found in $BaTiO_3$, where the dipoles in adjacent domains are antiparallel). The dark regions were domains (called c-domains) in which the dipole polarisation was perpendicular to the grain surface and thus parallel to the light beam. This corresponded to orientating the crystallographic c-axis and therefore the optic axis of the c-domains parallel to the beam. Accordingly the c-domain refractive index was isotropic relative to the plane of polarisation of incident light, and these domains appeared dark at all specimen angular positions when viewed between crossed polars. The bright regions corresponded to domains (called a-domains) in which the dipole polarisation, and consequently the optic axis, was parallel to the grain surface and hence perpendicular to the light beam. As the angular position of the specimen was altered, the orientation of the optic axes of the a-domains with respect to the plane of polarisation of the incident light changed, and the a-domains moved between optical transmission and extinction in a manner analogous to that already described for the case of a complete grain behaving uniformly.

No antiparallel domains were observed; this was not surprising since the optical properties, including birefringence, of antiparallel domains of $BaTiO_3$ are the same. It would, therefore, be difficult to obtain sufficient contrast to observe the boundary between adjacent domains; it is possible that several antiparallel domains might exist unobserved within some apparently uniform grains. This phenomenon might account for the observation that such uniform grains exhibited

alternate optical extinction and transmission as the specimen was rotated, despite their apparent absence of any domain structure.

Examination of the entire area of several specimens did not reveal the existence of any specific orientation of ferroelectric domains with respect to the grain boundaries which might be caused by the grain boundary space charge and correlated with the existence of the PTCR effect. This was consistent with the results of transmission electron microscopy investigations of ferroelectric domains in PTCR ceramics carried out by Haanstra and Ihrig [12].

The domain structures seen in this study were found to resemble those observed by Merz and other workers [6,7,8,9,10,13,15] in several investigations of single crystal $BaTiO_3$ using polarized light. They were also similar to features found by Arlt and Sasko [14] in experiments involving the chemical etching of polished undoped (i.e. non PTC) $BaTiO_3$ ceramics.

As described earlier, the properties of the undoped $BaTiO_3$ ceramics studied in this experiment closely resembled those of the doped PTC ceramics, and may be explained in identical terms. In fact, it was not possible to distinguish between doped and undoped specimens by microscopic examination. It was noted that the ferroelectric domain patterns of the undoped specimens were very similar to those of the doped specimens, and that again no specific pattern of domain orientation relative to the grain boundaries was discessible.

The similarity of the domain patterns in the doped and undoped

ceramics, together with the absence of any specific orientation of domains relative to grain boundaries in either case, seem to show that the formation of ferroelectric domains is due to the crystallographic properties of the grains. Since the presence or absence of the PTCR effect appeared to exert little or no influence on domain orientation, it is assumed that the grain boundary space charge responsible for the PTCR effect plays a subordinate role in the formation of domains, if it affects the process at all. This is consistent with the results of Haanstra and Ihrig, and with the standard model for the PTCR mechanism which postulates compensation of the grain boundary charge by ferroelectric domains but does not claim that the boundary charge governs domain formation.

Haanstra and Ihrig [12] also stated that 90° domains predominated, and suggested that the PTCR theory, which assumes 180° domains, may require modification to take account of this. Although the present investigation revealed numerous 90° domains, the difficulty of imaging 180° domains prevents the drawing of a definitive conclusion in this respect and it is considered that the predominance of 90° domains remains unproven. It is, therefore, considered that insufficient evidence exists about the precise orientation of the domains at the grain boundaries to require modification of the model.

(b) **Temperature Effects**

The changes in colour observed in the grains as the ceramic specimen was heated were caused by variations in refractive index. As

the temperature rose the permittivity changed, according to the Curie-Weiss law, with consequent variation of the refractive index. Since the permittivity and the refractive index of the tetragonal phase of $BaTiO_3$ are anisotropic, giving rise to the optical birefringence property, the temperature rise caused a change in the refractive indices of both the ordinary and extraordinary waves. This altered the differential optical path length travelled within the grain by the two waves, changing the condition for destructive interferences between the waves, and therefore the observed colour of the grain.

As the Curie point was reached, the $BaTiO_3$ underwent a change from the tetragonal to the cubic phase. Since the cubic phase was optically isotropic, optical extinction occurred as the specimen was viewed between crossed polars.

This explanation accounts for the observations on the undoped specimens. In the case of the doped specimens from batch UIB130, rotation of the specimen caused light to be transmitted through different areas of the grain boundaries while the grain bulk remained dark. This implied the existence of areas of residual optical anisotropy at the grain boundaries of the doped specimens, whereas such localised anisotropy was absent in the case of the undoped specimens.

A tentative explanation of the residual anisotropy may be advanced by considering the effect of the space charge at the grain boundaries; it is possible that the electric field generated at the grain boundary by the space charge was sufficiently intense to induce a local

distortion of the crystal lattice thus causing the optical anisotropy as if the tetragonal to cubic phase transition at the Curie point had not occurred. This was analogous to the increase in Curie temperature caused by the application of a strong external electric field to single crystals of $BaTiO_3$, first reported by Merz [16,17]. The effect would not occur in the undoped specimens, in which the grain boundary space charge and field were absent.

If this explanation is valid, this microscopical method may represent a means of examining the extent of grain boundary fields in specimens of various compositions and processing histories. Further work is, however, necessary to validate this tentative explanation. It is suggested that a comparison be made between specimens of a standard PTCR composition and processing history, some of which have been subjected to a subsequent reduction treatment (by heating in an argon atmosphere) to destroy the PTC effect and the grain boundary space charge and electric field. This should permit the determination of whether the optical activity was caused by the grain boundary field.

(c) **Externally Applied Field**

There is uncertainty about the nature of the mechanism responsible for the optical extinction phenomena observed when an external field was applied to this specimens. It is unlikely that resistive heating of the specimen by the current passed between the electrodes so as to raise the specimen temperature above the Curie point, was responsible. This is because the extinction, although appearing over a

period of 2-3 seconds after application of the field, vanished almost instantaneously (< ~ 0.1 sec) upon removal of the field. The speed of the phase change would be governed by the thermal time constants of the specimen in this model; these would be expected to be of the same order of magnitude whether the specimen was being heated or cooled. The observed transitions were inconsistent with this expectation.

Another possible mechanism is the electro-optic effect. In this case, the specimen was considered to operate as a transverse electro-optic modulator, of optical path length ℓ = 30 μm and electrode gap $x \simeq 1$ mm. The drive voltage required to produce a phase shift of π and optical extinction with this modulator geometry was estimated as ~ 29kV - about 2 orders of magnitude greater than the 300 V applied in practice. The electro-optic effect appeared to be an unlikely explanation. (In any case, the applicability of an analysis developed for single crystal modulators [18] to polycrystalline specimens was doubtful).

The final mechanism considered was the realignment of the domains within the grains, with the dipoles tending to align parallel to the applied field, with consequent alignment of the optic axes of the grains. Optical extinction then ensued if the plane of polarisation of the emergent light were perpendicular to that of the microscope analyzer. The fact that extinction proceeded in a wave across the field of view might be consistent with the sequential alignment of dipoles with an applied field: the events, however, occurred too rapidly for the

observer to discern whether ferroelectric domains were in fact moving.

It therefore appears that no definite conclusion can be drawn as to the mechanism responsible for these effects.

5.4.2 Electron Microscopy

(a) **EBIC**

The short circuits between electrodes were attributed to the pinholes found in many specimens, which permitted contact between the metal layers. In the case of the specimens where short circuiting had not occurred, the low rectification ratio (2:1) indicated that a true Schottky barrier was not formed: the reason for this failure is uncertain. It is possible that electron traps may have been formed at the electrode interface as a result of localised heating during electrode deposition [19], and that the properties of these traps then dominated, degrading the Schottky barrier [20].

The difficulties in fabricating usable Schottky barriers, which prevented the obtaining of an EBIC image, were similar to those encountered in the original work by Ralph, Gowers and Burgess [18,19]. Although they succeeded in obtaining EBIC images of ferroelectric domains and grain boundaries, Gowers stated [19] that the yield of usable specimens was very low, and that this had led directly to the abandonment of the technique. Accordingly the EBVE technique was used in preference to EBIC for the remainder of these studies.

(b) **EBVE**

The properties of the EBVE images detected in this investigation may be explained in the following terms. The specimen current from which the EBVE image was derived consisted of two separate components: a bias component and an electron-beam generated component. This bias component consisted of electrons (i.e. majority carriers) injected by the external battery circuit, whereas the beam-generated component arose from the production of electron-hole pairs by the interaction of the electron beam with the specimen, with the carriers being separated by the applied bias field before recombination could occur and therefore augmenting the specimen current under the influence of the bias field.

Variations in carrier lifetime at various points in the specimens were thus responsible for changes in the beam-generated current component whence the EBVE images were derived.

Drift of the bias current values, however, was ascribed to fluctuations in specimen temperature, since the external battery was connected across a specimen whose resistance was a very sensitive function of temperature in the vicinity of the PTCR transition temperature. Small temperature fluctuations could, therefore, cause significant variations in bias current.

The fact that the EBVE image in fig. 5.18, and the sketched line scans in fig. 5.20, reveal a marked increase in beam-generated current at grain boundaries above the PTCR transition temperature initially

appeared surprising because such an increase corresponded to a localised increase in carrier lifetimes at the grain boundary. Since there existed high concentrations of electron traps at the grain boundaries, in accordance with the Heywang theory, an increase in carrier lifetime at these points would seem improbable because the beam-generated electrons would rapidly be captured by the traps, whereas the hole lifetimes would, in any case, be expected to be short in a heavily n-doped semiconductor.

The increase in the lifetime of beam-generated charge carriers at the grain boundaries may, however, be explained in terms of the high electric fields produced by the space charge layers arising from the charge traps found at the grain boundaries. In the bulk of a grain, the electron and hole constituting a beam generated pair would tend to move in opposite directions under the influence of the externally-applied field, so that the increased separation would reduce the probability of recombination and increase the lifetime of the carrier pair. This effect would be expected to be slight under the influence of the fairly weak field generated by the external battery. In the vicinity of a grain boundary, however, where the local field was much stronger as a result of the space charge, this carrier separation effect would be expected to increase, increasing the carrier pair lifetime and therefore the beam-generated current. An increase in specimen current would therefore occur when the grain boundary was illuminated by the electron beam.

The disappearance of the current peak at the grain boundaries as the specimen temperature fell below the PTCR transition temperature (fig. 5.19) is attributable to the compensation of the grain boundary space charge below this temperature by the variation in permittivity and the formation of ferroelectric domains upon the charge to the tetragonal phase. Compensation of the space charge resulted in the diminution or disappearance of the grain boundary electric field, thus removing the cause of the increased carrier lifetime. The same mechanism was responsible for the disappearance of the PTCR effect, by reducing the grain boundary potential barrier heights, so that the PTCR and EBVE effects coincided.

The increase in the bias current observed as the specimen temperature fell was caused by the reduction in overall specimen resistance as a result of the PTCR effect.

It is considered that the EBVE technique is in principle generally applicable to the study of PTCR ceramics since EBVE images were obtained for several specimens from ceramic batches of different composition. Improvements to the technique are, however, necessary for its reliable implementation. These consist of improved specimen temperature control in order to reduce temperature induced bias current drift, and an increase in signal current integration time to counteract the electrical noise introduced by the numerous resistive barriers (i.e. the grain boundaries) in the signal current paths. The longer integration time, by increasing the time taken to record the image, reinforces the need to control bias current drift.

The results obtained using the EBVE techniques were consistent with the results obtained by other workers using different techniques for the direct observation of the grain boundaries. Haanstra and Ihrig [22] used a voltage contrast technique to show the existence of potential barriers between adjacent grains. A study carried out by Ihrig and Klerk [23] using a cathodoluminescence technique demonstrated the existence of a charge depletion layer at the grain boundaries. Koschek and Kubalek [24,25,26] carried out work by means of a spectrally-resolved cathodoluminescence technique which revealed the existence of high concentrations of Ba vacancies at the grain boundaries, acting as electron traps, in accordance with the PTCR effect theory. Mader, Meixner and Kleinschmidt's [27] work using infra-red microscopy revealed the existence of resistive effects at the grain boundaries which caused thermal dissipation to occur preferentially at the grain boundaries when an electrical current was passed through a specimen. The EBIC technique of Ralph et al. [19,20], although difficult to implement, succeeded in demonstrating a means of imaging the difference in charge carrier lifetime between the grain boundaries and the grain bulk above the PTCR transition temperature, as well as revealing the pattern of ferroelectric domains in the grains.

All these results were consistent with the Heywang theory of the PTCR effect. The present EBVE study, in forming images of the grain boundary potential barriers, which existed above the PTCR transition temperature and which were absent below this temperature, was also consistent with the PTCR theory and with the results of other workers.

5.5 Conclusions

The ferroelectric domain structure of ceramic specimens was revealed by means of polarized light microscopy, but no particular relationship between the ferroelectric domains and the grain boundaries was detected. Residual optical activity was observed at the grain boundaries of donor doped ceramics above the Curie point. The residual optical activity was not observed in undoped specimens. This phenomenon is believed to be attributable to an electro optic effect induced by the electric field of the grain boundary space charge layer in the doped specimen; the space charge and therefore the electro-optic effect was not seen in the undoped ceramic.

The use of polarized light microscopy to study the optical effects of externally applied electric fields produced no conclusive results because the effects observed occurred too rapidly for recording or analysis by still photography.

Electrical activity at the grain boundaries of doped ceramics was observed above the Curie point using the EBVE technique, and disappeared as the temperature was reduced below the Curie point. This phenomenon was attributed to an increase in the lifetime of beam-generated electron-hole pairs under the influence of uncompensated grain boundary electric fields above the transition temperature; below the transition temperature passivation of the space charges compensated the electric fields and quenched the activity. The EBVE technique was used to produce images of the electrical activity at grain boundaries, revealing the effects of the depletion layers

Both polarized light microscopy and the EBVE technique have been shown to be capable of forming images of ceramic grain boundaries and to be of potential value in the investigation of the grain boundary phenomena responsible for the PTC effect. Some additional development work is, however, required to improve the reliability of both methods before they can be used as routine experimental techniques.

References

1. Heywang, W., Solid St. Electron., 3 (1961) 51.
2. Jonker, G. H., Solid St. Electron., 7 (1964) 895.
3. Jonker, G. H. Mat. Res. Bull., 2 (1967) 401.
4. Daniels, J. and Wernicke, R., Philips Res. Rpts., 31 (1976) 344.
5. Daniels, J., Hardtl, K. H. and Wernicke, R., Philips Tech. Res., 38 (1978/79) 73.
6. Merz, W. J., Phys. Rev., 88 (1952) 421-2.
7. Merz, W. J., Phys. Rev., 95 [3] (1954) 690-8.
8. Merz, W. J., J. App. Phys., 25 [10] (1954) 1346 (+ cover).
9. Forsbergh, P. W., Phys. Res., 76 [8] (1949) 1187-1201.
10. Miller, R. C. and Savage, A., Phys. Rev. Lett., 2 [7] (1959) 294-6.
11. Hooton, J. A. and Merz, W. J., Phys. Rev., 98 [2] (1955) 409-13.
12. Haanstra, H. B. and Ihrig, H., J. Am. Ceram. Soc., 63 [5-6] (1980) 288-91.
13. Fatuzzo, E. and Merz, W. J., Ferroelectricity, Ch. 6, p190ff, North-Holland (1967).
14. Arlt, G. and Sasko, P., J. App. Phys., 51 [9] (1980) 4965-60.

15. Jaffe, B., Cook, W. R. and Jaffe, H., Piezo-electric Ceramics, Ch. 5, p64-70, Academic Press (1971).

16. Merz, W. J., Phys. Rev., 91 (1953) 513.

17. Fatuzzo, E. and Merz, W. J., Ferroelectricity, pp33-34, North Holland (1967).

18. Yariv, A., Quantum Electronics, 3rd Ed., (1989) p298-317, Wiley.

19. Ralph, J. E., Gowers, J. P. and Burgess, M. R., App. Phys. Lett., 41 [4] (1982) 343-5.

20. Gowers, J. P., Private Communication.

21. Sze, S. M., Physics of Semiconductor Devices, 2nd Ed., (1981) p245-8, Wiley.

22. Haanstra, H. B. and Ihrig, H., Phys. Stat. Sol. (a), 39 (1977) K7-K10.

23. Ihrig, H. and Klerk, M., App. Phys. Lett., 35 [4] (1979) 307-9.

24. Koschek, G. and Kubalek, E., Phys. Stat. Sol. (a), 79 (1983) 131-9.

25. Koschek, G. and Kubalek, E., Ferroelectrics, 68 (1986) 293-303.

26. Koschek, G. and Kubalek, E., Phys. Stat. Sol. (a), 102 (1987) 417-24.

27. Mader, M., Meixner, H. and Kleinschmidt, P., J. Appl. Phys., 56 [10] (1984) 2832-6.

CHAPTER 6

CONCLUSIONS

6.1 General Remarks

The work described in this thesis consisted of investigations into various aspects of the PTCR effect in n-doped $BaTiO_3$ semiconducting ceramics. A number of techniques were used to study the transition of ceramics fired in air from conductive to insulating behaviour at room temperature as the donor dopant concentration was increased, in an attempt to discover the mechanism causing this transition. The effects of high temperature annealing for varying time intervals in oxidising and reducing ambient atmospheres on the PTCR characteristics of the ceramic were investigated in order to study the properties of the grain boundary vacancies responsible for the PTCR effect. Polarized light microscopy was used to examine the ferroelectric domain structure of thin specimens of PTCR ceramic and to study the relationship between the domains and the grain boundaries. Using a scanning electron microscope, an electron barrier voltaic effect technique was applied and used to observe variations in contrast across the images of ceramic specimens and to examine the effects of grain boundaries on carrier lifetimes.

6.2 Donor Dopant Effects

The investigation of the transition from conductive to resistive room temperature behaviour at high donor dopant concentrations revealed that the increase in room temperature resistivity is exclusively a grain boundary phenomenon. Dielectric measurements at A.F. and

R.F. revealed that the transition was associated with an increase in grain boundary resistance, whereas the resistivity of the grain bulk remained unchanged. This was in conflict with the theory of Daniels et al. which postulated that the transition to insulating behaviour was caused by the reduction in grain size at high donor dopant concentrations, resulting in the grain boundary depletion layer extending throughout the grain bulk. Measurements of the dependence of the room temperature resistivity on the applied electric field eliminated the formation of an insulating intergranular second phase as a possible cause of the insulating behaviour of heavily doped samples.

Analysis of the resistivity-temperature characteristics of the specimens in terms of the Ihrig-Puschert model showed behaviour consistent with an increase in acceptor density at the grain boundaries, together with an increase in activation energy of the acceptors, at high donor dopant concentrations. The mechanism responsible for these changes is not yet understood. It is concluded that the increase in acceptor density and activation energy at high dopant concentrations enhances the height of the grain boundary potential barriers and modifies the resistivity-temperature characteristic to produce the change from conductive to insulating behaviour.

Additional work is recommended in order to characterize the behaviour of the grain boundary potential barriers more fully. This includes measurement of the resistivity over an extended range above the transition temperature in order to permit the determination of

barrier activation energies from Arrhenius plots, and the measurement of resistivity as a function of applied electric field above the transition temperature to investigate the conduction mechanisms in greater detail. Measurement of the relative permittivity as a function of temperature for the various dopant concentrations would be useful and might permit greater accuracy of analysis using the Ihrig-Puschert model. It would also be interesting to extend the investigation to include ceramics incorporating alternative donor dopants.

6.3 Annealing Effects

Investigations of the effects of reduction and reoxidation treatments on specimens previously annealed in air revealed the presence of an insulating layer arising from the annealing process. Such a layer had originally been postulated by Daniels, who stated that it consisted of a layer rich in Ba vacancies acting as acceptors. The effect of the reduction process in lowering the minimum resistivity and diminishing the PTCR effect of the specimens was found to be interpreted more effectively in terms of Al-Allak's extension to the Daniels model. This extended model incorporates the formation of oxygen vacancies which are ionised at room temperature and hence compensate the reduction in conduction electron density caused by the barium vacancies. Reoxidation results in the rapid elimination of the oxygen vacancies as a result of their high mobility, reversing the compensation mechanism and restoring the PTCR effect.

Annealing of specimens in air at high temperature has been shown to produce an enhancement of the grain boundary potential barrier by increasing the acceptor state density. This causes the increase in maximum resistivity and reduction in temperature at which maximum resistivity occurs with increased annealing time. The increase in minimum resistivity with annealing time is attributed both to the enhancement of the potential barrier and to the formation of the resistive grain boundary layer.

The nature of the grain boundary resistive layer and its dimensions are not yet known, and it is recommended that further work be directed towards investigating the properties of the resistive layer and its relationship with the potential barrier. To this end measurement of potential barrier activation energies, and the dependence of resistivity upon the applied electric field, above the transition temperature might be useful, together with the measurement of the relative permittivity as a function of temperature.

6.4 Polarized Light Investigations

Investigations using polarized light microscopy revealed the ferroelectric domain structure of ceramic specimens but failed to show any definite relationship between ferroelectric domain structure and the grain boundaries. However, the technique revealed the existence of residual optical activity above the ferroelectric transition temperature at the grain boundaries of donor doped specimens: this residual

activity was entirely absent in undoped ceramics. This phenomenon is attributed to an electro-optic effect induced by the electric field arising from the grain boundary space charge layer which is responsible for the PTCR effect in doped ceramics: the space charge layer and thus the electro-optic effect was not present in undoped specimens. It is suggested that this study be extended to specimens which have been subjected to reduction and reoxidation treatments in order to discover whether the optical activity disappears and returns with the PTCR effect.

Studies of the optical effects induced by the application of external electric fields proved inconclusive because the speed with which the phenomena occurred after the field was applied prevented recording or analysis of an image using still photography. Effective application of this experimental technique would therefore require an alternative method of recording the images such as video recording or possibly the use of an alternating applied field accompanied by stroboscopic illumination of the specimen.

6.5 EBVE Studies

The electron barrier voltaic effect experiments showed the existence of electrical activity in the form of an increase in the beam generated current at the grain boundaries above the PTCR transition temperature. The activity was absent below the transition temperature and was observed to appear and disappear as the transition was

traversed. The electrical activity was attributed to an increase in the lifetime of beam-generated electron-hole pairs, which drifted apart under the influence of the electric fields of the grain boundary potential barriers above the transition temperature. Compensation of the grain boundary space charge below the transition temperature removed the electric field and eliminated the electrical activity.

The EBVE technique is clearly capable of forming images of the distribution of carrier lifetimes within the grains of the ceramic and is thus of potential use in the study of the grain boundary depletion layers. Additional work would be required to refine the technique, in particular to improve the signal to noise ratio of the image and to control the specimen temperature more accurately, before it could be used routinely. It would be valuable if this technique could be used systematically to study the grain boundaries in conjunction with measurements of the electrical properties of the materials.

6.6 Final Conclusions

It is concluded that the PTCR effect is exclusively a grain boundary phenomenon. The evidence for this was provided by the dielectric measurements, which showed that variations in the PTC characteristic with specimen composition and processing history were associated solely with changes in the grain boundary resistance and that the grain bulk resistivity component was unaltered.

It is further concluded that the PTC properties are primarily determined by the grain boundary potential barriers, and that the effect of the thickness of any insulating layers at the grain boundaries is relatively unimportant compared with that of the potential barrier height. This conclusion is supported by the evidence of the analysis of resistivity-temperature characteristics according to Ihrig and Puschert's model, and by the polarized light microscopy and EBVE investigations. It therefore appears that an appropriate model for the PTCR effect would more closely resemble the Heywang model than that proposed by Daniels.

Finally we conclude that the grain boundary potential barriers influence the resistivity of the ceramics at low temperatures, below the PTC transition. Evidence for this conclusion is provided by the activation energies derived from the low temperature Arrhenius plots.

APPENDICES

APPENDIX A1

Derivation of Normalized Resistance

In order to investigate the influence of donor dopant concentration on the temperature dependence of resistance of a PTC material where the resistance is dominated by grain boundaries, it is necessary to allow for the effect of donor dopant concentration on grain size. It is only if the reduction in grain size (and hence increase in the number of grain boundaries) with increasing dopant concentration is accounted for that comparison can be made between specimens containing different donor dopant concentrations. This dependence on the number of grain boundaries may be allowed for by using the values of resistance normalized per grain boundary of area 1 cm^2 for comparison: this normalized resistance, ρ', is defined by :

$$\rho' = \frac{RA}{2g} \qquad \text{(A1.1)}$$

where R is the measured resistance of the specimen (in Ω), A is the cross-sectional area of the specimen (cm^2) and g is the number of grains between the electrodes or half the number of grain boundaries. g is calculated from the relation

$$g = \frac{\ell}{d} \qquad \text{(A1.2)}$$

where ℓ is the distance between the electrodes and d is the mean grain size, making the assumption that the grains are approximately cuboid in form, an assumption that appears to be justified by the microstructure of the materials

observed using the scanning electron microscope.

The use of the normalized resistance, defined in (A1.1) above, thus removes the effect of variations in the number of grain boundaries, in specimens incorporating different donor dopant concentrations. Comparison of normalized resistance values therefore enables the influence of donor dopant concentration on the temperature dependence of resistance of the grain boundaries to be established for an identical area of a single grain boundary in specimens of different composition.

Since the resistivity of the material is defined by

$$\rho = \frac{RA}{\ell} \qquad \text{(A1.3)}$$

substitution of equations (A1.2) and (A1.3) into (A1.1), together with the previous assumption of cuboid grains, gives the following relationship between normalized resistance and resistivity.

$$\rho' = \frac{\rho d}{2} \qquad \text{(A1.4)}$$

APPENDIX A2

Derivation of the Ihrig-Puschert Model

The influence of specimen composition and processing history on the PTCR characteristic may be investigated by the construction of ρ_{max} vs. T_{max} diagrams, first described by Jonker. In this method, values of ρ_{max} vs. T_{max} are calculated using the Heywang equations for a number of different values of acceptor energy E_A and acceptor density N_{A0}. The values of ρ_{max} and T_{max} are calculated over a range of, say E_A at constant N_{A0} and the locus plotted on a graph of ρ_{max} vs. T_{max}. The process is then repeated for other values of N_{A0}, until a map of (ρ_{max} vs. T_{max}) has been constructed over the range of all values of E_A and N_{A0} of interest, meanwhile keeping all other relevant parameters such as the charge carrier density n and the average grain size d constant. The plotting of experimentally measured values of ρ_{max} vs. T_{max} [1] on the diagrams then permits estimation of the values of E_A and N_{A0} of the ceramic specimens.

The ρ_{max} vs. T_{max} plots were calculated by the method of Ihrig and Puschert [1], as follows. The diffusion equation relating the current density J to the voltage V across a single Heywang barrier at a grain boundary, including field and diffusion currents, is

$$J = ne\mu \frac{\partial V}{\partial z} + kT\mu \frac{\partial n}{\partial z} \qquad \text{(A2.1)}$$

where n is the charge carrier density in the grain bulk, μ is the carrier mobility and z is the distance from the centre of the barrier at $z = 0$. Integration across the depletion layer according to a method described by Mallick and Emtage

[2], and Kulwicki and Purdes [3], which assumes a Schottky-type parabolic potential barrier, leads to the following expression :

$$J(V) \propto ne\mu \frac{\phi_0}{2}\left(1-\exp\left(-\frac{eV}{kT}\right)\right)\left(1-\frac{V^2}{16\phi_0^2}\right)\left(\exp\left(-\frac{e\phi_0\left(1-\frac{V}{4\phi_0}\right)^2}{kT}\right)\right) \quad \text{(A2.2)}$$

Here, ϕ_0 denotes the maximum potential barrier height, where

$$\phi_0 = \frac{e N_A^2(T)}{8\,\varepsilon_r(T)\,\varepsilon_0 n} \quad \text{(A2.3)}$$

where

	$\varepsilon_r(T)$	is the relative permittivity in the depletion layers
	ε_0	is the permittivity of free space
	e	is the electronic charge
	n	is the charge carrier density in the grain bulk
	μ	is the charge carrier mobility
	$N_A(T)$	is the density of ionized uncompensated acceptors at T K.

N_A is given by the Fermi distribution

$$N_A(T) = N_{A0}\left[1+\exp\left(\frac{e\phi_0 - E_A + E_F}{kT}\right)\right]^{-1} \quad \text{(A2.4)}$$

where N_{A0} is the acceptor state density per unit area of the grain boundary;
E_A is the energy interval between the acceptor levels and the conduction band edge, and
E_F is the Fermi level.

The Fermi level is defined by

$$E_F = kT\,\ell n\left(\frac{N_C}{n}\right) \quad \text{(A2.5)}$$

where N_C is the effective density of states in the conduction band. The width

of the grain boundary depletion layer, z_0 is given by

$$z_0 = \frac{N_A(T)}{2n} \qquad \text{(A2.6)}$$

The relative permittivity ε_r is generally assumed to be determined by the Curie-Weiss law,

$$\varepsilon_r = \frac{C}{T - T_0} \qquad \text{(A2.7)}$$

Where C is the Curie constant and T_0 is the Curie temperature. As a result of the linearization of the spatial dependence of the potential in order to simplify integrations during the derivation of equation A2.2 (the Schottky approximation [3]), the equation is an approximation valid for $e\phi_0 >> kT$. The formula is subject to the additional requirement that $V < 4\phi_0$. It is found experimentally that both these conditions are met for practical PTC ceramics.

At small V, the following approximations may be made in equation A2.2

$$\left(1 - \exp\left(-\frac{eV}{kT}\right)\right) \approx \frac{eV}{kT}$$

$$\left(1 - \frac{V^2}{16\phi_0^2}\right) \approx 1$$

$$\exp\left(\frac{-e\phi_0\left(1 - \frac{V}{4\phi_0}\right)^2}{kT}\right) \approx \exp\left(\frac{-e\phi_0}{kT}\right)$$

Thus, for small V, equation A2.2 becomes

$$J \simeq ne\mu \left(\frac{\phi_0}{z_0}\right) \frac{eV}{kT} \exp\left(\frac{-e\phi_0}{kT}\right) \qquad \text{(A2.8)}$$

The resistance R_F^B of unit area of the grain boundary, measured with a small applied voltage so that the approximations derived above for small V apply, is given by

$$R_F^B = V/J$$

$$= \rho_n \frac{kT}{e\phi_0} z_0 \exp\left(+\frac{e\phi_0}{kT}\right) \qquad \text{(A2.9)}$$

where $\rho_n = (ne\mu)^{-1}$ and the charge carrier mobility $\mu = 0.5$ cm^2/Vs [4,5] is the value for small polaron charge carriers.

For a system consisting of the bulk of a grain of average size d and resistance R_F^G, in series with a grain boundary, both of unit cross-sectional area, the resistance is given by

$$R_F = R_F^B + R_F^G = R_F + \rho_n d \qquad \text{(A2.10)}$$

$$R_F = \rho_n (kT/e\phi_0)\, z_0 \exp(e\phi_0/kT) + \rho_n d \qquad \text{(A2.11)}$$

which leads to an expression for the resistivity of the system

$$\rho = \rho_n [d + (kT/e\phi_o)\, z_0 \exp(e\phi_0/kT)]\, (d + z_0)^{-1} \qquad \text{(A2.12)}$$

This expression also gives the resistivity of the polycrystalline ceramic, provided that appropriate mean values of parameters are substituted in the derivation. Since in general $d >> z_0$, it follows that $d + z_0 \simeq d$ and A2.12

simplifies to

$$\rho = (ne\mu)^{-1}\left[1 + \frac{z_0}{d}\left(\frac{kT}{e\phi_0}\right)\exp\left(\frac{e\phi_0}{kT}\right)\right] \qquad \text{(A2.13)}$$

Setting C = 1.2 x 10^5K and T_0 = 388 K [6], and N_C = 1.5 x 10^{22} cm^{-3} (equal to the Ti^{4+} ion density) [4] and deriving the charge carrier concentration n from the grain bulk resistivity ρ_{bulk} found from dielectric measurements (Section 3.3.3) by the relation $n = (e\mu\rho_{bulk})^{-1}$, equations A2.3 and A2.4 were solved numerically to calculate ϕ_0 (T) and N_A (T) over a range of temperatures. Substitution for ϕ_0 (T) in A2.13 then enabled the resistivity-temperature characteristic to be calculated : the values of ρ_{max} and T_{max} were then determined by an intercept method. Repetition of the process over the range of E_A and N_{A0} of interest was carried out to construct the (ρ_{max}, T_{max}) map. The numerical calculations were executed using a program run on a BBC microcomputer.

The use of ρ_{max} vs. T_{max} diagrams constructed according to the Ihrig-Puschert model to study the effect of variation of ceramic composition on the properties of acceptor traps at the grain boundaries is complicated by the fact that variation in the concentration of donor dopant atoms influences the mean grain diameter and therefore the number of grain boundaries per unit length in the specimen, as well as the properties of the grain boundary acceptor traps. Since the grain size is a parameter in the calculation of ρ_{max} vs. T_{max} diagrams, which are usually calculated for constant grain size, a method is required to compensate for the effect of varying grain size on resistivity so that materials

of different grain sizes may be plotted on a single diagram for direct comparison.

Considering equation A2.13 above, at the peak resistivity ρ_{max} and the corresponding temperature T_{max},

$$\frac{1}{ne\mu} \ll \frac{z_0}{d}\left(\frac{kT}{e\phi_0}\right)\exp\left(\frac{e\phi_0}{kT}\right) \qquad \text{(A2.14)}$$

so that the first term may be neglected. This corresponds to ignoring the grain bulk component of resistivity, since the resistivity of the material is dominated by the grain boundary properties. Thus

$$\rho_{max}\,(T_{max}) \;\alpha\; d^{-1} \qquad \text{(A2.15)}$$

where d is the mean grain size.

If a series of ρ_{max} vs. T_{max} curves is plotted for a ceramic having mean grain size d_0 and values of ρ_{max} are measured, denoted $\rho_{max,1}$, $\rho_{max,2}$ etc. for different materials with respective mean grain sizes d_1, d_2 ..... etc., then from A2.15 above we may define a normalised resistivity ρ^*_{max}, where

$$\rho^*_{max,1} = \rho_{max,1} \cdot \frac{d_1}{d_0} \;.....\; etc. \qquad \text{(A2.16)}$$

This has the effect of eliminating the influence of grain size on measured peak resistivity values, so that values of ρ^*_{max} may be plotted on the curves calculated for $d = d_0$ and a direct comparison made between the properties of specimens of different mean grain diameter.

References

1. Ihrig, H. and Puschert, W., J. Appl. Phys., **48** (1977) 3081.

2. Mallick, G. T. and Emtage, P. R., J. Appl. Phys., **39** (1968) 3088.

3. Kulwicki, B. M. and Purdes, A. J., Ferroelectrics, **1** (1970) 253.

4. Ihrig, H., J. Phys. C, **9** (1976) 3469.

5. Gerthsen, P., Groth, R. and Härdtl, K. H., Phys. Stat. Sol., **11** (1965) 303.

6. Johnson, C. J., Appl. Phys. Lett., **7** (1965) 221.

APPENDIX A3

Conditions for Extinction in the Polarizing Microscope

The arrangement of the polarizing elements and specimen in the polarized light microscope is illustrated schematically in figure A3.1; the lens elements which behave isotropically with respect to the polarization of light, have been omitted for clarity. The direction of polarization of the first polarizing element, the microscope polarizer, is defined as direction 1, set at +45° to the x-axis and that of the second polarizing element, the microscope analyzer, is defined as direction 2, at -45° to the x-axis: the directions of polarization of the polarizer and analyzer are therefore mutually perpendicular, i.e. the condition of 'crossed polars'.

The polarizing properties of an optical element may be defined in terms of a [2 x 2] matrix, known as the Jones matrix [1]. For the present case the relevant matrices are as follows :

For the polarizer, a linear polarizer at +45°, $A_1 = \frac{1}{2}\begin{bmatrix} 1 & 1 \\ 1 & 1 \end{bmatrix}$ (A3.1)

For the analyzer, a linear polarizer at -45°, $A_3 = \frac{1}{2}\begin{bmatrix} 1 & -1 \\ -1 & 1 \end{bmatrix}$ (A3.2)

The effect of a birefringent specimen is to introduce a phase shift between the horizontal and vertical components of the polarization, due to the difference in the optical path lengths for the two polarizations. The specimen may therefore be considered to be a differential phase shifter with a corresponding

Jones matrix,

$$A_2 = \begin{bmatrix} e^{i(\psi_0 + \Delta\psi)} & 0 \\ 0 & e^{i(\psi_0 - \Delta\psi)} \end{bmatrix} \qquad \text{(A3.3)}$$

where $\psi_0 + \Delta\psi = \frac{2\pi n_1 \ell}{\lambda}$ $\qquad$ $\psi_0 - \Delta\psi = \frac{2\pi n_2 \ell}{\lambda}$

and

ℓ is the specimen thickness

n_1 is the refractive index in the specimen of light polarized along direction 1

n_2 is the refractive index in the specimen of light polarized along direction 2

λ is the wavelength of the light in vacuum.

Since the specimens investigated are optically anisotropic, in general $n_1 \neq n_2$ and light waves polarized along directions 1 and 2 undergo differing phase shifts as these pass through the specimen, represented by $\Delta\psi_0 + \Delta\psi$ and $\Delta\psi_0 - \Delta\psi$ respectively. ψ_0 may be regarded as the mean value of these phase shifts, where

$$\psi_0 = \frac{2\pi\ell}{\lambda}\left(\frac{n_1 + n_2}{2}\right) \qquad \text{(A3.4)}$$

The light incident on the microscope polarizer is horizontally plane polarized and in the Jones matrix notation is denoted by a two-component vector, the Jones vector;

$$E_i = \begin{bmatrix} E_{ix} \\ E_{iy} \end{bmatrix} = \begin{bmatrix} 1 \\ 0 \end{bmatrix} \qquad \text{(A3.5)}$$

The polarization state of light transmitted through a polarizing element is given by the product of the Jones matrix for the element and the Jones vector for the incident light. Thus for light transmitted through the polarizer (see Fig. A3.1) :

$$E_1 = A_1 E_i$$

$$E_1 = \begin{bmatrix} E_{1x} \\ E_{1y} \end{bmatrix} = \frac{1}{2} \begin{bmatrix} 1 & 1 \\ 1 & 1 \end{bmatrix} \begin{bmatrix} 1 \\ 0 \end{bmatrix} = \frac{1}{2} \begin{bmatrix} 1 \\ 1 \end{bmatrix} \qquad \text{(A3.6)}$$

i.e. linearly polarized at +45°, as expected.

Transmission through the specimen gives :

$$E_2 = A_2 E_1$$

$$E_2 = \frac{1}{2} \begin{bmatrix} e^{i(\psi_o + \Delta\psi)} & 0 \\ 0 & e^{i(\psi_o - \Delta\psi)} \end{bmatrix} \begin{bmatrix} 1 \\ 1 \end{bmatrix} = \frac{1}{2} e^{i\psi_o} \begin{bmatrix} e^{i\Delta\psi} \\ e^{-i\Delta\psi} \end{bmatrix} \qquad \text{(A3.7)}$$

and after transmission through the analyzer :

$$E_3 = A_3 E_2$$

$$E_3 = \frac{1}{2} \begin{bmatrix} 1 & -1 \\ -1 & 1 \end{bmatrix} e^{i\psi_o} \begin{bmatrix} e^{i\Delta\psi} \\ e^{-i\Delta\psi} \end{bmatrix} = \frac{e^{i\psi_o}}{2} \begin{bmatrix} 2i\sin\Delta\psi \\ -2i\sin\Delta\psi \end{bmatrix}$$

$$E_3 = i e^{i\psi_o} \sin\Delta\psi \begin{bmatrix} 1 \\ -1 \end{bmatrix} \qquad \text{(A3.8)}$$

so that light emerges from the microscope linearly polarized at -45°.

The intensity of the light transmitted through the system is given in the usual way by

$$I = |E_3|^2 = E_3 E_3^* \qquad \text{(A3.9)}$$

$$= \left(i\,(\cos\psi_0 + i\sin\psi_0)\,\sin\Delta\psi\sqrt{(1)^2 + (-1)^2}\,\right)$$

$$\times \left(-i\,(\cos\psi_0 - i\sin\psi_0)\,\sin\Delta\psi\sqrt{(1)^2 + (-1)^2}\,\right)$$

$$= 2\sin^2\Delta\psi$$

and, substituting for $\Delta\psi$

$$I = 2\sin^2\left(\frac{2\pi\,|n_1 - n_2|\,\ell}{\lambda}\right) \qquad \text{(A3.10)}$$

It is now necessary to express n_1 and n_2 in terms of the refractive indices n_o and n_e of the uniaxial birefringent specimen, and of the angle θ between the optic axis of the specimen and the direction of polarization of the microscope polarizer, direction 1, which serves as the reference direction of the system.

Diagram (A3.2) shows the projection of the indicatrix of the specimen onto the plane of the microscope stage (and of the specimen itself). O′A′ is the projection of the optic axis, since the optic axis itself may often be inclined out of the plane, depending on the specimen orientation. n_o' and n_e' represent the projected values of n_o and n_e into the plane, and n_1 and n_2 the values of refractive index in directions 1 and 2 respectively.

The projection of the principal section of the indicatrix is itself an ellipse, with the equation

$$\frac{u^2}{(n_o')^2} + \frac{v^2}{(n_e')^2} = 1 \qquad \text{(A3.11)}$$

where $\tan\theta = \frac{u}{v}$ or $u = v\tan\theta$ $\quad v = u\cot\theta$ (see Fig. A3.2)

Substituting for u and rearranging gives

$$v = \left(\frac{(n_o')^2 (n_e')^2}{(n_o')^2 + (n_e')^2 \tan^2\theta} \right)^{\frac{1}{2}} \qquad \text{(A3.12)}$$

and similarly, $$u = \left(\frac{(n_o')^2 (n_e')^2}{(n_e')^2 + (n_o')^2 \cot^2\theta} \right)^{\frac{1}{2}}$$

Now the components of the refractive index along the microscope system axes 1, 2 are given by

$$n_1 = \sqrt{u_1^2 + v_1^2}, \quad n_2 = \sqrt{u_1^2 + v_1^2} \qquad \text{(A3.13)}$$

i.e. $$n_1 = \left(\frac{(n_o')^2 (n_e')^2}{(n_o')^2 + (n_e')^2 \tan^2\theta} + \frac{(n_o')'^2 (n_e')'^2}{(n_e')^2 + (n_o')^2 \cot^2\theta} \right)^{\frac{1}{2}} \qquad \text{(A3.14)}$$

$$n_2 = \left(\frac{(n_o')^2 (n_e')'^2}{(n_o')^2 + (n_e')^2 \tan^2(\theta - 90°)} + \frac{(n_o')^2 (n_e')^2}{(n_e')^2 + (n_o')^2 \cot^2(\theta - 90°)} \right)^{\frac{1}{2}}$$

Note that when :

$$\theta = 0^\circ \qquad n_1 - n_2 = n_e' - n_o'$$

$$\theta = 90^\circ \qquad n_1 - n_2 = n_o' - n_e'$$

and the transmitted light (Eq. A3.10) intensity I reaches its maximum value. Similarly when the sample is rotated such that :

$$\theta = 45^\circ, 135^\circ, \text{etc. ...} \qquad n_1 - n_2 = 0$$

the transmitted light intensity I = 0, i.e. total extinction occurs.

It can be seen that successive transmission maxima occur at 90° intervals, as do successive extinction positions, and that maxima occur at 45° from the adjacent minima.

It may also be noted that in the special case where the optic axis is perpendicular to the plane of the specimen, $n_1 = n_2$ for all values of θ, the specimen appears isotropic, and total extinction occurs for all θ.

Reference

1. The reader is referred to any standard text on optics, e.g. E. Hecht and A. Zajac, "Optics", Chp. 8, Addison-Wesley, London, 1974.

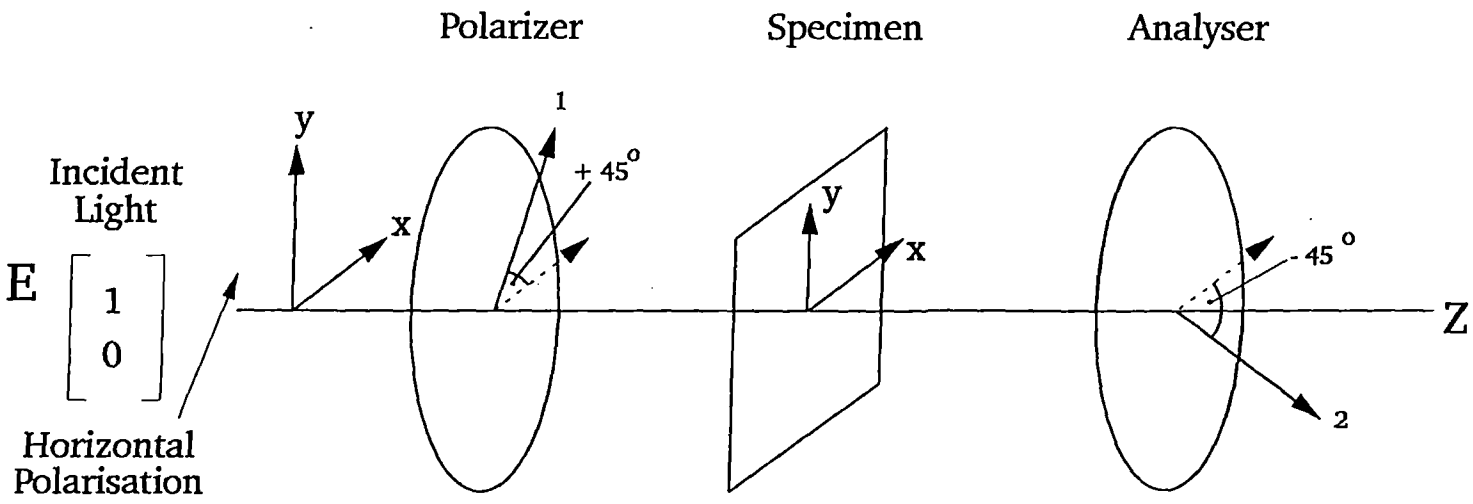

Fig. A3.1 Arrangement of polarizing elements in a polarizing microscope (non-polarizing lens elements have been omitted for clarity).

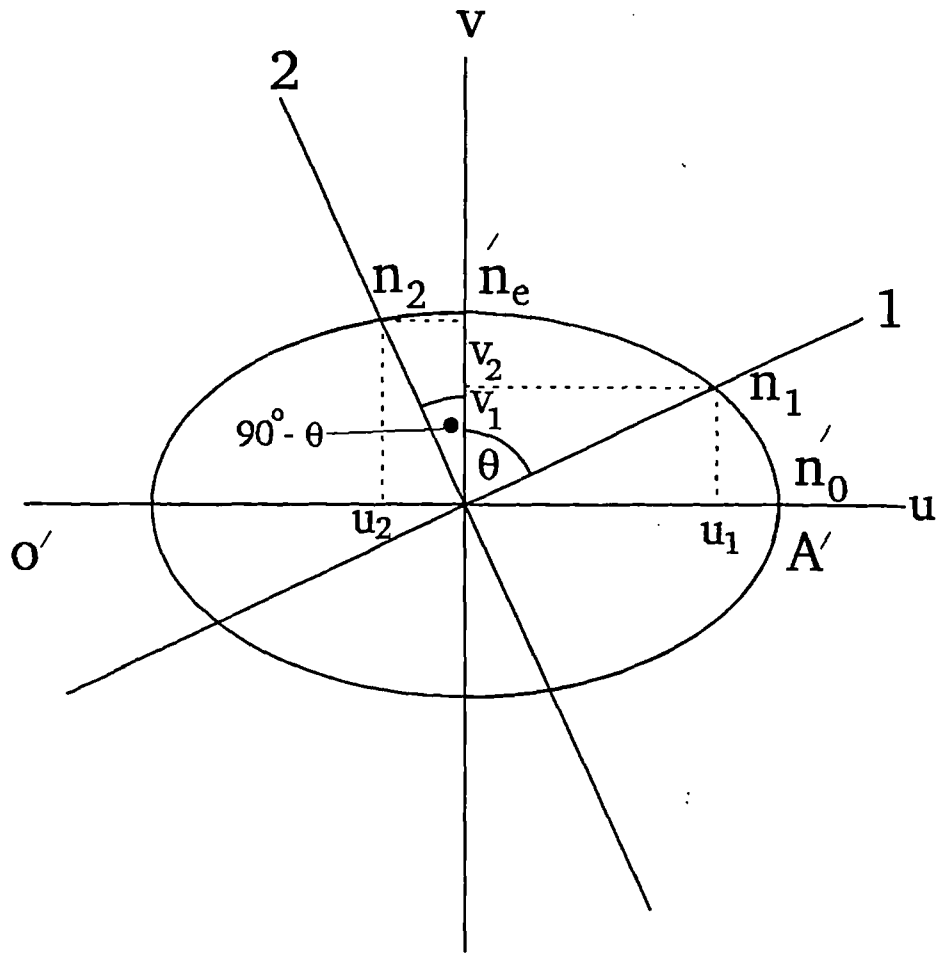

Fig. A3.2 Projection of specimen indicatrix onto the microscope stage plane (u, v) and relation to the microscope polarizer axes (1, 2).